

POLITECNICO DI MILANO

Dipartimento di Elettronica, Informazione e Bioingegneria

Corso di Laurea Magistrale in Ingegneria Biomedica



FE simulation of a novel design for a Sano procedure in Hypoplastic Left Heart: a valved venous conduit reinforced with an outer Palmaz stent

Relatore: Prof. Emiliano Votta

Correlatore: Dott. Alessandro Caimi

Tesi di Laurea di:

Elena Corna, matricola 883965

Anno Accademico 2017/2018

Table of contents

Abstract	iv
Introduction.....	iv
Materials and Methods.....	v
Results and Discussion	viii
Conclusions.....	x
References.....	xi
Sommario	xii
Introduzione	xii
Materiali e Metodi.....	xiii
Risultati e Discussione.....	xvi
Conclusioni	xviii
Bibliografia	xx
1 Clinical background.....	1
1.1 The human heart	1
1.1.1 Anatomy of the heart	1
1.1.2 The cardiac cycle	4
1.2 Congenital heart diseases	5
1.2.1 Hypoplastic Left Heart Syndrome	5
1.2.2 Surgical treatments for HLHS	7
1.2.3 Innovative surgical procedures for first stage treatment of HLHS	10

2	State of the art	14
2.1	Numerical modelling of HLHS treatment.....	14
2.1.1	Palmaz stent FE models.....	16
2.1.2	Saphenous vein.....	18
2.1.3	Venous valve leaflets.....	22
2.2	Aim of the thesis	25
3	Materials and Methods	26
3.1	Introduction.....	26
3.2	Geometries, meshes and sensitivity analysis	28
3.2.1	Palmaz Stent	28
3.2.2	Saphenous vein.....	29
3.2.3	Venous valve leaflets.....	32
3.2.4	Mesh convergence study	35
3.3	Saphenous valved conduit cardiac cycles simulation	36
3.4	Simulation of the surgical procedure	38
3.4.1	Stent pre-expansion	38
3.4.2	Stent-vein assembly and vein pressurization.....	39
3.4.3	Stent crimping procedures and cardiac cycles simulation.....	40
3.5	Post processing.....	41
4	Results and Discussion	44
4.1	Mesh convergence analysis.....	44
4.1.1	Palmaz stent.....	44
4.1.2	Saphenous vein.....	48
4.1.3	Venous valve leaflets.....	53

4.2	Simulation of the surgical procedure	56
4.2.1	Stent pre-expansion	56
4.2.2	Stent-vein assembly and vein pressurization.....	57
4.2.3	Stent crimping and post-crimping biomechanics during the cardiac cycle ...	57
5	Conclusions	68
5.1	Conclusions.....	68
5.2	Limitations and Future developments.....	70
	References.....	72

Abstract

Introduction

Hypoplastic left heart syndrome - The hypoplastic left heart syndrome (HLHS) is one of the most complex and severe congenital heart defects seen in the new-born; in this pathology, the left atrium and ventricle are completely unable to support the circulation needed by the body's organs. HLHS treatment requires a heart transplant, however, it is possible to initially resort to a three-step surgical procedure, called staged palliation: in this thesis work the first stage of this procedure was taken into account [1].

Innovative surgical procedure for first stage treatment of HLHS - At Boston Children's Hospital, a novel Sano procedure for the first stage palliation in HLHS treatment was developed: the implantation in the right ventricle to pulmonary artery position of a valved venous conduit compressed within a Palmaz Biliary Stent [2]. If clinical monitoring suggests that the shunt allows for too much retrograde flow to the lungs, it might be externally crimped, either in the operating room or later in the intensive care unit. This procedure prevents a blood reverse flow into the right ventricle, using a valved conduit; it reduces the shunt diameter by stent crimping, in case of patients with pulmonary hypertension; moreover, it allows the re-expansion of the RV-PA conduit, accommodating it to the child's growth. However, this crimping is done manually and so there is a risk of inaccurate maneuvers that can result in an irregular conformation of the valved shunt and in an increase of the hydraulic impedance of the conduit, leading to the development of pulmonary hypertension.

Numerical modelling for HLHS treatment - The pioneering use of a stent sewn and crimped on the outer surface of a vessel, presented by the Boston group [2], is a new promising approach, which impacts has not yet been assessed by clinical follow-up data. Numerical modelling, and in particular Finite Element (FE) method, could help gaining insight into its

potential effects, and in order to perform a robust computational simulation of the surgery [2], firstly it was necessary to find a suitable modeling of its components: the Palmaz stent and the valved venous shunt.

As concerns the Palmaz XL Transhepatic Biliary stent, in scientific literature only studies intended to study the use of the device for intra-lumen implantations can be found. Besides, to the best of the author's knowledge, the study published by J. Vesely in 2015 [3] is the only one presenting a comprehensive set of material parameters for human saphenous veins, suitable for describing multi-axial stress states and characterized through the Holzapfel model. With regard to the venous valve leaflets, the study of Hammer et al. [4] was chosen as reference work: in this study, the authors used a structural FE model of valve leaflet grafts and the leaflets mechanical properties were described using a Fung-like hyperelastic model.

Aim of the thesis - This thesis aimed at reproducing the novel procedure proposed by Boston Children's Hospital [2] for the first stage palliation of HLHS treatment and studying the different geometrical configurations and stress patterns that may occur after a crimping, ideally cylindrical or resulting in an elliptical profile of the reinforced shunt, of a Palmaz stent on a saphenous conduit, using the FE solver Abaqus/Explicit (Simulia, Dassault Systèmes, Providence, RI, USA).

Materials and Methods

Introduction - The models of the Palmaz stent, a saphenous vein conduit and a bileaflet venous valve were designed. Their dimensions and their material properties were selected according to pre-existent studies [3] [4]. For each one of these components, multiple meshes with different element densities were generated and the corresponding results were compared by means of a mesh convergence analysis in order to select the most convenient discretizations for the complete simulation of the surgical procedure.

As stated in [2], the valved graft was inserted in the Palmaz stent, pre-expanded, and pressurized; then, this assembly was crimped. Moreover, during a successive cardiac cycles simulation, the crimped valve dynamics and the valvular orifice area behavior were studied. In parallel, it was also assembled an unstented valved venous conduit, to be used as a comparison for the crimped one's dynamics and orifice area.

The schematic workflow that was followed in this thesis work is shown in **Figure 1**.

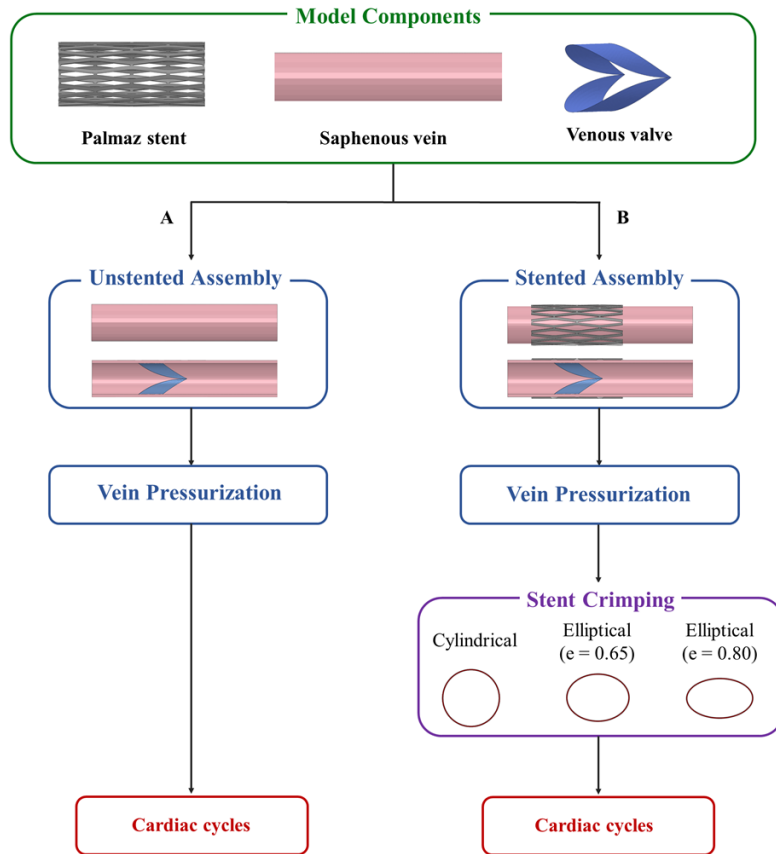


Figure 1: Workflow of the thesis.

Saphenous valved conduit cardiac cycles simulation (Figure 1.A) - The venous valve leaflets and the saphenous vein were assembled; the nodes of the valve leaflet insertion lines were tied to the inner wall of the saphenous vein conduit. A ventricular surface and an arterial one were defined on the inner surface of the vein conduit and they were loaded by a pressure ramp from 0 to 80 mmHg over a 2.0 s time-frame. After a 0.5 s stabilization time interval, two cardiac cycles were simulated, each one lasting 0.8 s, by applying three different time-dependent surface pressures, whose definition was consistent with the surgical procedure to be mimed [2] and its use for HLHS patients. The vein ventricular and arterial surfaces were loaded by a time-dependent pressure (i.e., the left ventricular and the aortic physiological pressures) and the ventricular side of the saphenous valve leaflets was loaded by the difference between ventricular and aortic pressure. Along the whole simulation, the nodes at the two ends of the saphenous vein conduit were constrained in order to allow only radial displacements. Valve dynamics and maximum principal stress patterns were monitored throughout the second simulated cardiac cycle; these data were used as baseline reference when analyzing the data yielded by the subsequent simulation of venous stenting.

Simulation of the surgical procedure (Figure 1.B) - The external stenting of the venous shunt and the post-stenting biomechanics of the system were simulated consistently with the features of the procedure to be modeled [2]. Four processes were simulated:

1. Stent pre-expansion: In order to allow the insertion of the saphenous graft, the Palmaz stent was expanded up to 8 mm internal diameter, through a radial expansion of a co-axial cylinder. The plastic strains (PEEQ) computed at the end of the expansion procedure were extracted, in order to be imported in the subsequent simulation of the stent crimping procedure.
2. Stent-vein assembly and vein pressurization: The pre-expanded stent was positioned co-axially around the vein to have its central cross section at the position of the vein valve. Then, a uniform pressurization of 80 mmHg was described to the internal surface of the graft.
3. Stent crimping: A cylindrical crimper was modelled and placed externally to all the other set-up components, so to be coaxial with the stent and the vein, and it was shrunk by imposing nodal displacements. Three different crimping modalities were simulated in order to mimic distorted configurations: cylinder with a perfectly circular (*CIL*) cross-section with a 6 mm diameter; two cylinders with an elliptic cross-section whose perimeters were the same as the cylindrical cross-section and whose eccentricity was 0.65 (*E65*) or 0.80 (*E80*).
4. Cardiac cycles simulation: Two cardiac cycles were simulated by imposing the same boundary conditions adopted when simulating the behavior of the valved saphenous conduit in the pre-stenting condition.

Postprocessing - During both the simulation of the un-stented conduit and the simulation of the complete surgical procedure, the geometric configuration of the set-up parts as well as their mechanical behavior were analyzed. Concerning the saphenous conduit, the maximum principal stresses were examined, while the Von Mises Stress and the equivalent plastic strain (PEEQ) were considered for the stent. Furthermore, boxplots and statistical tests were performed on these data. Moreover, the maximum principal strains obtained at the level of the leaflets' commissures when considering the different crimping modalities were compared, computing the time-course of the respective 90th and the 50th percentiles during the second cardiac cycle simulation.

In addition, to evaluate the valve behavior during the cardiac cycle, the time-dependent valve geometric orifice area (GOA) was assessed by acquiring images of the valve geometry on a plane transversal to the vein axis, along the entire systolic phase of the second cardiac cycle, through an ad-hoc MATLAB (MathWorks, Natick, MA, USA) code. This procedure was carried out both for the non-stented vein and for every crimped venous conduit, to measure the behavior of the valve GOA over time and to compare the different outcomes of the three different crimping, also by means of maximum, 90th and mean GOA values.

Results and Discussion

Stresses on the vein wall after crimping – With the increasing eccentric shapes of the stent cross-section, an increasing corrugation of the crimped portion of the saphenous vein conduit was highlighted, and a progressive enhancement of the range of the maximum principal stresses σ_I was detected (**Figure 2**). High stress regions were identified close to the ends of the venous conduit, conversely, in the crimped part of the conduit, stresses were progressively lower. A Kruskal-Wallis test and a Dunn’s multiple comparisons test proved the highly statistical difference between the groups *CIL* and *E65* and the groups *CIL* and *E80*, while they rejected the statistical difference of *E65* and *E80*. Hence, it was assessed that a non-ideal cylindrical crimping modality may overstress the saphenous conduit; however, a lower or higher deviation of the defective crimping final configuration to the ideal one may not change the resulting stress pattern of the saphenous vein conduit.

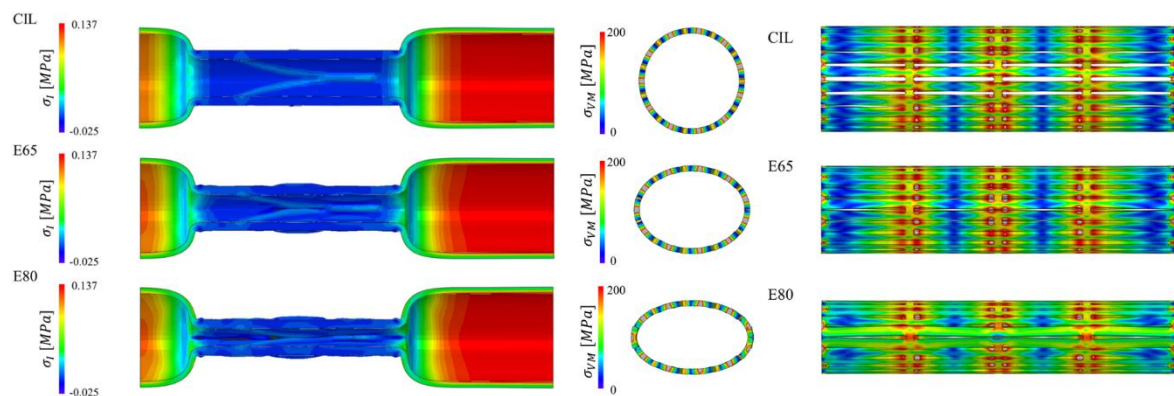


Figure 2: Abaqus color maps showing the σ_I pattern of the venous conduit, axially cut, (left) and the σ_{VM} of the Palmaz stent (right) after crimping with the three evaluated modalities: *CIL*, *E65* and *E80*.

Stresses and plastic strains on the stent after crimping - An increasing eccentricity of the stent crimped cross-section led to increase the values of the σ_{VM} (**Figure 2**): in particular, the 50th percentile increased from 126.08 MPa in the *CIL* configuration to 132.42 MPa in the *E65* configuration and up to 160.10 MPa in the *E80* configuration; the maximum σ_{VM} value increased from 526.66 (*CIL*), to 550.87 (*E65*) and to 574.74 (*E80*). This result confirms that the execution of a defective crimping procedure may lead to an actual variation of the stress distribution in the Palmaz stent, causing an overstressing with respect to the ideally cylindrical procedure.

It was found that an increase in the eccentricity of the stent crimped cross-section resulted in a progressively higher number of yielded elements, in particular in elliptical crimping a higher plasticization was obtained in the region of maximum struts “squeezing”, due to the final configuration imposed by the virtual crimper.

Post-crimping stent stresses during the cardiac cycle - A significant increase in the maximum stresses was detected, from *CIL* to *E80* the σ_{VM_MAX} was almost doubled; however, the 90th and 50th percentiles exhibited an inverse trend.

Post-crimping valve leaflet strains during the cardiac cycle - When the conduit was crimped in an elliptical way the strains at the commissure increased, but it was slightly higher in the *E65* case with respect to the *E80* one. The difference in the deformation level could potentially accelerate the deterioration of the valve leaflets and lower their long-term durability, however, given the short-term application considered in this thesis work [2], the long-term durability of the implanted shunt was not a major issue.

Valve orifice area during the cardiac cycle - In the post-crimping configurations of the reinforced conduit the GOA vs. time waveform of the uncrimped case was preserved. However, the amount of GOA was highly different in the three crimped cases: In *E65* the GOA was reduced by about 15% with respect to *CIL*, while in *E80* the reduction was almost by 60% of the *CIL* GOA (**Figure 3**). This was related to the higher obstruction of the conduit due to the leaflets, which was caused by the increasing eccentricity of the stent cross-section. Generally, the crimped leaflets exhibited a refold configuration, during the whole cardiac cycle simulation: however, the resulting orifice was still approximately circular in the *CIL* case, while in *E65* case the valve leaflets were so folded on themselves that they protruded into the lumen of the saphenous conduit for over a third of its height and in *E80* they even came into contact, splitting the orifice area of the valve in two separate sections.

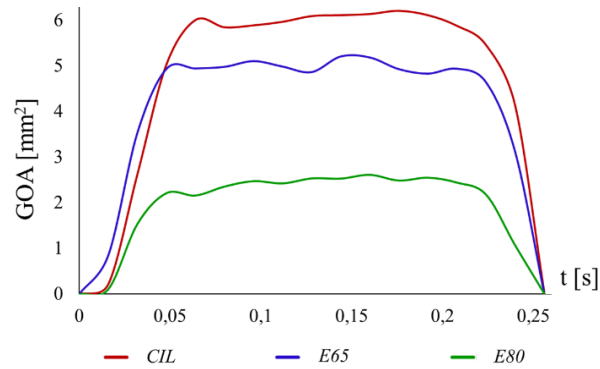


Figure 3: Geometric orifice area obtained for the crimped valved conduit in the different crimping modalities (*CIL*, *E65*, *E80*).

Conclusions

The employed methods succeeded in providing a complete simulation of the innovative Sano procedure performed at Boston’ Children Hospital [2], including the crimping of a Palmaz stent on the outer surface of the valved venous shunt, a novelty for the numerical modelling scientific literature, in which, so far, only the stent intra-lumen implantation was taken into account.

It was possible to establish the effects of different crimping on a stent and a venous conduit, through the evaluation of the stress patterns and plastic strains that arose. It was assessed that a non-ideally cylindrical crimping modality may lead to an actual variation of the stress distributions with respect to the ideally cylindrical procedure, overstressing both the stent and the saphenous conduit.

Indeed, the vein geometric orifice area was gradually reduced passing from the cylindrical crimping to the most elliptical one; the elliptical crimping simulation led to a protrusion of the folded valve leaflets into the lumen resulting in a higher hydraulic encumbrance caused by the shunt conduit. This could produce an increase in the hydraulic resistance of the conduit, that could in effect enhance the work done by the right ventricle to overcome it and in result produce an associated hypertension at the level of the pulmonary circulation or of the lungs.

Besides, a validation of the model would be required: a parallel experimental study is at the development stage at Boston Children’s Hospital in order to assess the behavior of a concrete reinforced valved saphenous vein subjected to a crimping procedure, when placed in a hydraulic experimental set-up.

References

- [1] E. Braunwald, D. Zipes and P. Libby, *Heart Disease: A Textbook of Cardiovascular Medicine* (sixth edition), Chapter 43 - Congenital Heart Disease in Infancy and Childhood, W. B. Saunders Company, 2001.
- [2] E. Roberts, L. Quinonez, B. Piekarski and S. E. C.W. Baird CW2, “Expandable Valve for Pediatric Application Constructed From Human Venous Valved Conduit Within a Stent,” *Ann Thorac Surg*, vol. 100, no. 6, pp. 2320-4, 2015.
- [3] J. Veselý, L. Horný, H. Chlup, T. Adámek, M. Krajíček and R. Žitný, “Constitutive modeling of human saphenous veins at overloading pressures,” *J Mech Behav Biomed Mater.*, vol. 45, pp. 101-8, May 2015.
- [4] P. Hammer, E. Roberts, S. Emani and P. D. Nido, “Surgical reconstruction of semilunar valves in the growing child: Should we mimic the venous valve? A simulation study,” *J Thorac Cardiovasc Surg*, vol. 153, no. 2, pp. 389-396, Feb 2017.

Sommario

Introduzione

Sindrome del cuore sinistro ipoplasico – L'ipoplasia ventricolare sinistra (HLHS) è una delle cardiopatie congenite più gravi e complesse osservate nei neonati; in questa patologia, l'atrio e il ventricolo sinistro risultano essere inadeguati a fornire il flusso circolatorio necessario a tutti gli organi. Il trattamento della HLHS richiede un trapianto cardiaco, tuttavia, è possibile ricorrere inizialmente a una procedura chirurgica palliativa in tre fasi: in questo lavoro di tesi è stata presa in considerazione la prima fase di questa chirurgia [1].

Procedura chirurgica innovativa per il trattamento di primo stadio di HLHS - Al Boston Children's Hospital è stata sviluppata una nuova procedura di Sano per il primo stadio della palliazione nel trattamento di HLHS: l'impianto tra il ventricolo destro e l'arteria polmonare di un condotto venoso valvolato compresso all'interno di un Palmaz biliary stent [2]. Se il monitoraggio clinico mostra che lo shunt consente un eccessivo flusso retrogrado ai polmoni, il condotto potrebbe essere crimpato, direttamente in sala operatoria, o successivamente in terapia intensiva. Questa procedura consente la prevenzione del flusso sanguigno retrogrado nel ventricolo destro, grazie all' utilizzo di un condotto valvolato e la riduzione del diametro dello shunt mediante *crimping* dello stent, in caso di pazienti con ipertensione polmonare. Inoltre, permette la re-espansione del condotto, per adattarlo alla crescita del bambino. Tuttavia, questa procedura di *crimping* viene eseguita manualmente e vi è dunque il rischio che si verifichino manovre inaccurate che potrebbero comportare una conformazione irregolare dello shunt e un conseguente aumento dell'impedenza idraulica del condotto, inducendo lo sviluppo di ipertensione polmonare.

Modellizzazione numerica per il trattamento di HLHS – L'uso inedito di uno stent suturato e crimpato sulla superficie esterna di un vaso, presentato dal gruppo di ricerca di Boston [2], è un nuovo promettente approccio, il cui impatto non è stato ancora accertato per mancanza

di dati di follow-up clinico. La modellazione numerica, e in particolare il metodo degli elementi finiti (FE), potrebbe fornire un aiuto per comprendere meglio i suoi potenziali effetti e, per poter eseguire una simulazione computazionale attendibile dell'intervento [2], è stato necessario sviluppare, innanzitutto, un modello adeguato per i suoi componenti: il Palmaz stent e lo shunt venoso valvolato.

Per quanto riguarda il Palmaz XL Transhepatic Biliary stent, nella letteratura scientifica si possono trovare studi che riguardano solo l'uso del dispositivo per impianto endovascolare. Inoltre, per quanto noto all'autore, lo studio pubblicato da J. Vesely nel 2015 [3] risulta essere l'unico a presentare un completo set di parametri per la descrizione del materiale della vena safena umana, adatto a descrivere stati di stress multi-assiale, e caratterizzato attraverso il modello di Holzapfel. Per quanto riguarda i lembi valvolari venosi, lo studio di Hammer et al. [4] è stato scelto come lavoro di riferimento: gli autori hanno utilizzato un modello strutturale FE di *graft* valvolari venosi e le proprietà meccaniche dei lembi sono state descritte utilizzando un modello iperelastico di tipo Fung.

Scopo della tesi - Questo lavoro di tesi mirava a riprodurre l'innovativa procedura sviluppata presso il Boston Children's Hospital [2] per il primo stadio della chirurgia palliativa per HLHS e a studiare le diverse configurazioni geometriche e le distribuzioni di sforzo che si potrebbero verificare dopo il *crimping*, cilindrico o risultante in una sezione ellittica dello *shunt* rinforzato, di un Palmaz stent su un condotto safenico, utilizzando il solutore FE Abaqus/Explicit (Simulia, Dassault Systèmes, Providence, RI, USA).

Materiali e Metodi

Introduzione - Sono stati realizzati i modelli del Palmaz stent, di una vena safena e di una valvola a due lembi venosa. Le loro dimensioni e proprietà dei materiali sono state scelte sulla base di studi presenti in letteratura [3] [4]. Per ognuno di questi componenti, sono state generate varie *mesh* con diversa densità di elementi, che sono state confrontate mediante un'analisi di sensitività per selezionare le discretizzazioni più adatte per la simulazione della procedura chirurgica completa.

Come nella chirurgia sopra citata [2], il *graft* valvolato è stato inserito all'interno del Palmaz stent, pre-espanso, e pressurizzato; dopodiché questo set-up è stato crimpato. Inoltre, sono stati studiati la dinamica della valvola crimpata e il comportamento dell'area geometrica dell'orifizio valvolare (GOA), durante una successiva simulazione di cicli cardiaci.

In parallelo, è stato assemblato anche un condotto venoso valvolato privo di stent, da utilizzare come confronto per il condotto crimpato, in termini di dinamica valvolare e GOA. Il *workflow* che è stato seguito in questo lavoro di tesi è mostrato in **Figure 1**.

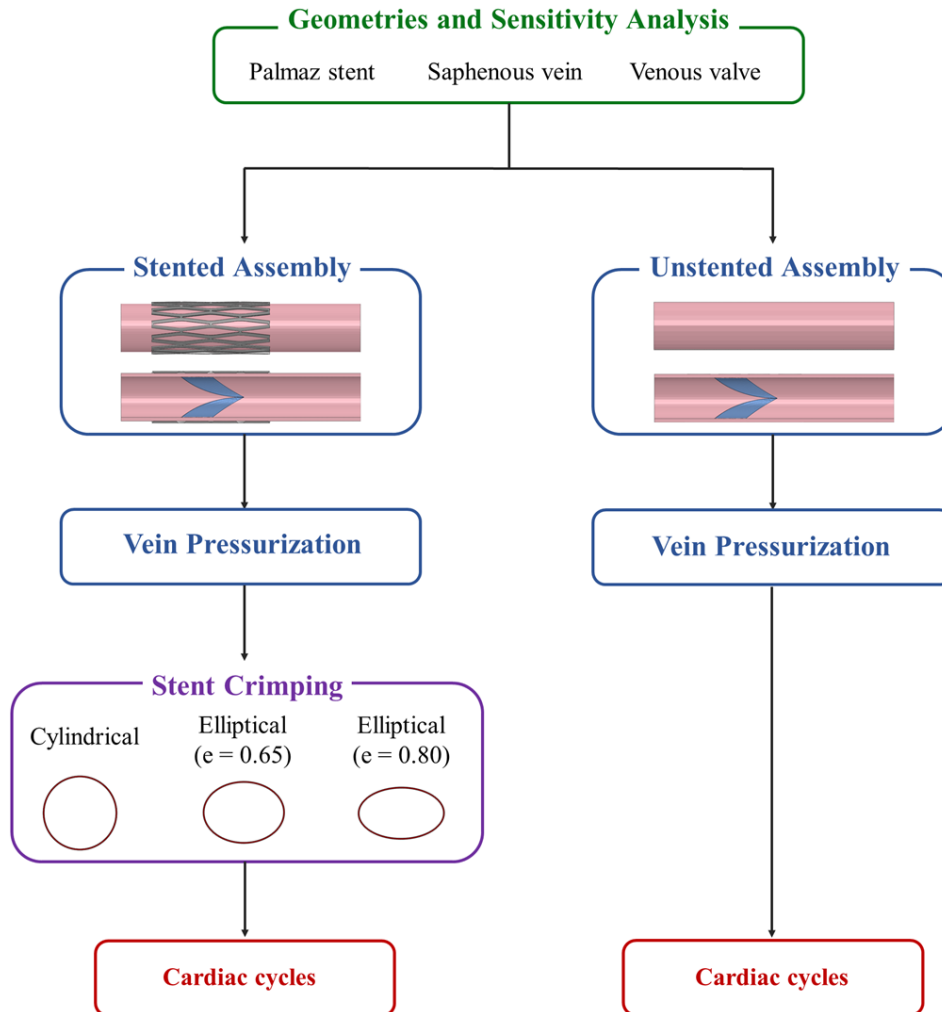


Figura 1: Workflow della tesi.

Simulazione dei cicli cardiaci nella safena valvolata (Figura 1.A) - I lembi valvolari venosi e la vena safena sono stati assemblati; i nodi dei margini di attacco dei foglietti valvolari sono stati connessi alla parete interna della safena. Sulla superficie interna del condotto della vena sono state definite una superficie ventricolare ed una arteriosa, che sono state caricate con una rampa di pressione da 0 a 80 mm Hg, in un arco di tempo di 2 s. Dopo un intervallo di stabilizzazione di 0.5 s, sono stati simulati due cicli cardiaci, ciascuno della durata di 0.8 s, applicando tre diverse pressioni superficiali tempo-dipendenti, definite coerentemente con la procedura chirurgica da replicare [2] e il suo uso per pazienti con HLHS. Alla superficie

ventricolare della vena e a quella arteriosa sono state imposte pressioni tempo-dipendenti (i.e., le pressioni del ventricolo sinistro e dell'aorta) e sulla superficie ventricolare dei lembi valvolari è stata applicata la differenza tra pressione ventricolare e aortica. In ogni fase, i nodi alle due estremità del condotto della vena safena sono stati vincolati a muoversi solo radialmente. La dinamica valvolare e le distribuzioni degli sforzi principali massimi sono state monitorate durante il secondo ciclo cardiaco simulato; questi dati sono stati utilizzati come riferimento nell'analisi dei dati ottenuti dalla successiva simulazione dello *stenting*.

Simulazione della procedura chirurgica - Lo *stenting* esterno dello shunt venoso e la biomeccanica del sistema *post-stenting* sono stati simulati coerentemente con la procedura da modellizzare [2]. Sono stati simulati quattro processi:

1. Pre-espansione dello stent: al fine di consentire il successivo inserimento del *graft* safenico, il Palmaz stent è stato espanso ad un diametro interno di 8 mm, utilizzando un cilindro, coassiale con esso. I valori delle deformazioni plastiche (PEEQ) calcolate alla fine della procedura di espansione sono stati estratti per poter essere assegnati allo stent nella successiva fase di *crimping*.
2. Assemblaggio dello stent-vena e pressurizzazione della vena: lo stent pre-espanso è stato posizionato esternamente alla vena e coassialmente con essa, in modo da avere la sua sezione trasversale centrale in corrispondenza della valvola. Dopodiché, la vena è stata uniformemente pressurizzata a 80 mmHg.
3. *Crimping* dello stent: è stato modellizzato un crimpatore cilindrico, collocato esternamente a tutti gli altri componenti del set-up, coassiale con lo stent e la vena, ed è stato ristretto imponendo spostamenti nodali. Tre modalità di *crimping* sono state simulate in modo da replicare diverse configurazioni finali: un cilindro con una sezione trasversale perfettamente circolare (*CIL*) con un diametro di 6 mm; due cilindri con una sezione trasversale ellittica i cui perimetri erano gli stessi della sezione cilindrica e la cui eccentricità era 0.65 (*E65*) o 0.80 (*E80*).
4. Simulazione dei cicli cardiaci: sono stati simulati due cicli cardiaci imponendo le stesse condizioni al contorno adottate durante la simulazione del comportamento del condotto valvolato safenico nella condizione di *pre-stenting*.

Postprocessing - Durante le simulazioni della safena valvolata non stentata e della procedura chirurgica completa, sono state analizzate le configurazioni geometriche dei componenti del *set-up* ed il loro comportamento meccanico. Per quanto riguarda il condotto safenico, sono

state valutate le sollecitazioni principali massime, mentre per lo stent sono stati considerati gli sforzi di Von Mises e le deformazioni plastiche equivalenti (PEEQ). Inoltre, con questi dati sono stati realizzati dei *boxplot* e sono stati eseguiti test statistici. Oltre a ciò, le massime deformazioni principali ottenute a livello delle commessure dei lembi ventricolari sono state usate per confrontare le diverse modalità di *crimping*, ricavando l'andamento dei rispettivi 90° e 50° percentile durante la simulazione del secondo ciclo cardiaco.

In aggiunta, per valutare il comportamento della valvola durante il ciclo cardiaco, è stato valutato l'andamento dell'area geometrica dell'orifizio valvolare (GOA) acquisendo immagini della geometria della valvola su un piano trasversale all'asse della vena, durante l'intera fase sistolica del secondo ciclo cardiaco, utilizzando un codice MATLAB (MathWorks, Natick, MA, USA). Questa procedura è stata eseguita sia per la vena senza stentata che per ogni condotto venoso crimpato, per misurare il comportamento della GOA valvolare nel tempo e per confrontare i diversi esiti dei tre *crimping*, anche per mezzo del calcolo del massimo, del 90° percentile e del valore medio della GOA.

Risultati e Discussione

Sforzi sulla parete venosa dopo il crimping - All'aumentare dell'eccentricità imposta alla sezione trasversale dello stent crimpato, sono stati rilevati una crescente corrugazione della porzione crimpata del condotto safenico ed un aumento progressivo del range delle sollecitazioni massime principali σ_1 (**Figura 2**). Le regioni ad alta sollecitazione sono state identificate vicino alle estremità del condotto venoso, al contrario, nella parte crimpata del condotto, gli stress erano progressivamente minori. Con un test di Kruskal-Wallis e un test di Dunn per i confronti multipli è stata verificata un'elevata differenza statistica tra i gruppi *CIL* ed *E65* e tra i gruppi *CIL* ed *E80*, mentre non è stata rilevata una differenza statistica tra *E65* ed *E80*. Ne consegue che una modalità di *crimping* cilindrica non ideale potrebbe sovrasollecitare il condotto safenico; tuttavia una deviazione più o meno grande della configurazione risultante dal *crimping* inesatto, rispetto al caso cilindrico, potrebbe non modificare la distribuzione di sforzo nel condotto safenico.

Sforzi e deformazioni plastiche dello stent dopo il crimping - L'aumento dell'eccentricità della sezione trasversale dello stent crimpato ha indotto un aumento dei valori σ_{VM} (**Figura 2**): in particolare, il 50° percentile è aumentato da 126.08 MPa nella configurazione *CIL* a 132.42 MPa nella configurazione *E65* e fino a 160.10 MPa nella configurazione *E80*; il

valore massimo di σ_{VM} è aumentato da 526.66 (*CIL*), a 550.87 (*E65*) e a 574.74 (*E80*). Questi risultati confermano che l'esecuzione di una procedura di *crimping* difettosa può portare ad una variazione effettiva della distribuzione degli sforzi nel Palmaz stent, causando un'eccessiva sollecitazione rispetto alla procedura cilindrica ideale.

Si è riscontrato che un aumento dell'eccentricità della sezione trasversale crimpata dello stent ha comportato progressivamente un maggiore numero di elementi plasticizzati, in particolare nel *crimping* ellittico è stata ottenuta una maggiore plastificazione nella regione massimamente compressa a seguito della configurazione finale imposta dal *crimper*.

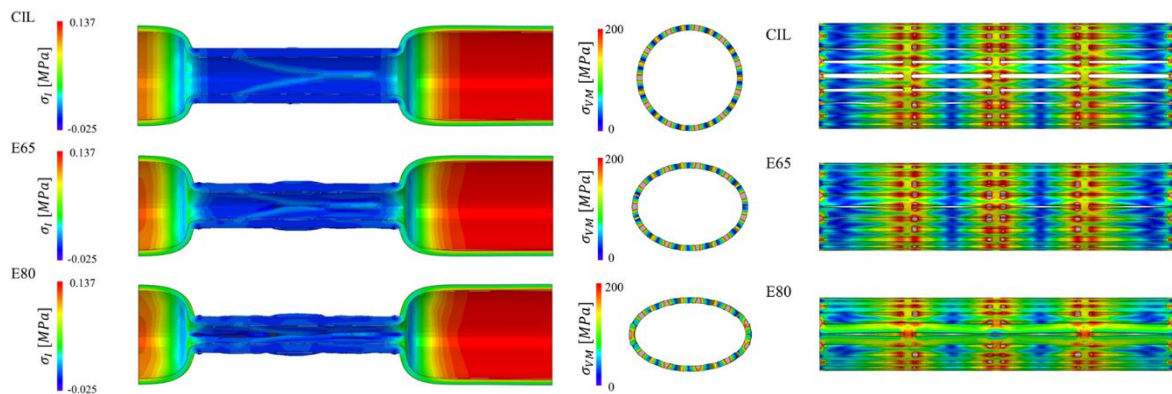


Figura 2: Mappe colore delle distribuzioni dei σ_t nel condotto venoso, sezionato assialmente, (sinistra) e dei σ_{VM} del Palmaz stent (destra) dopo il *crimping* con le tre diverse modalità: *CIL*, *E65* and *E80*.

Sforzi dello stent post-crimping durante i cicli cardiaci - È stato rilevato un aumento significativo degli sforzi massimi, da *CIL* a *E80* σ_{VM_MAX} è stato quasi raddoppiato; tuttavia, il 90° e il 50° percentile hanno mostrato *trend* inverso.

Deformazioni dei foglietti valvolari post-crimping durante i cicli - Quando il condotto è stato crimpato in modo ellittico, la deformazione delle commissure valvolari è aumentata, ed è risultata di poco superiore nel caso *E65* rispetto a quello *E80*. La differenza nel livello di deformazione potrebbe potenzialmente accelerare il deterioramento dei lembi valvolari, diminuendone la durabilità, tuttavia, data l'applicazione a breve termine considerata in questo lavoro di tesi [2], la resistenza a lungo termine dello shunt impiantato non è stata considerata una problematica rilevante.

Area dell'orifizio valvolare durante i cicli cardiaci - Nelle configurazioni *post-crimping* del condotto rinforzato è stata mantenuta la forma d'onda della GOA nel tempo rispetto al caso non crimpato. Tuttavia, l'entità della GOA è risultata molto diversa nei tre casi crimpati: in

E65 la GOA si è ridotta di circa il 15% rispetto al caso *CIL*, mentre in *E80* la riduzione è stata di quasi il 60% rispetto a *CIL* (**Figura 3**). Ciò è stato correlato alla maggiore ostruzione del condotto dovuta ai lembi valvolari, causata dalla crescente eccentricità della sezione trasversale dello stent. Generalmente, i foglietti crimpati hanno mostrato una configurazione ripiegata, durante l'intera simulazione del ciclo cardiaco: tuttavia, l'orifizio risultava essere ancora approssimativamente circolare nel caso *CIL*, mentre nel caso *E65* i lembi valvolari erano così ripiegati da sporgere nel lume del condotto safenico per oltre un terzo della sua altezza e in *E80* i lembi sono persino entrati in contatto, suddividendo l'area dell'orifizio valvolare in due sezioni distinte.

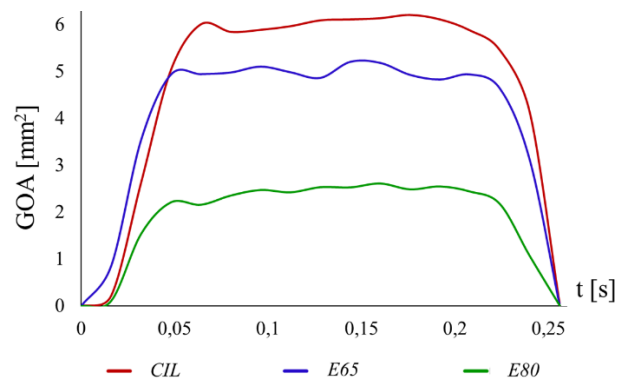


Figura 3: Area geometrica dell'orifizio valvolare, ottenuta per il condotto valvolato crimpato secondo le diverse modalità (*CIL*, *E65*, *E80*).

Conclusioni

Con i metodi impiegati si è riusciti ad ottenere una simulazione completa dell'innovativa procedura di Sano eseguita al Boston' Children Hospital [2], compreso il *crimping* di un Palmaz stent sulla superficie esterna di uno shunt venoso valvolato, una novità per la letteratura scientifica nel campo della modellazione numerica, in cui, finora, era stato preso in considerazione solo l'impianto endovascolare dello stent.

È stato possibile stabilire gli effetti di un diverso *crimping* sullo stent e su un condotto venoso, attraverso la valutazione delle distribuzioni di sforzo e di deformazione plastica che sono sorte. È stato osservato che una modalità di *crimping* non idealmente cilindrica potrebbe portare ad una effettiva variazione delle distribuzioni di sforzo rispetto alla procedura ideale, sovrasollecitando sia lo stent che il condotto safenico.

Inoltre, l'area dell'orifizio geometrico della vena ha subito una graduale riduzione passando dal *crimping* cilindrico al più ellittico; la simulazione di *crimping* ellittico ha portato a una protrusione dei lembi valvolari ripiegati nel lume, provocando un maggiore ingombro idraulico dello shunt. Ciò potrebbe produrre un aumento della resistenza idraulica del condotto, che potrebbe causare un aumento del lavoro svolto dal ventricolo destro in risposta e produrre una conseguente ipertensione a livello della circolazione polmonare o dei polmoni.

Una validazione del modello sarebbe necessaria: un parallelo studio sperimentale è in fase di progettazione presso il Boston Children's Hospital, al fine di valutare il comportamento di una reale vena safena rinforzata sottoposta ad una procedura di *crimping*, qualora collocata in un *set-up* idraulico sperimentale.

Bibliografia

- [1] E. Braunwald, D. Zipes and P. Libby, *Heart Disease: A Textbook of Cardiovascular Medicine* (sixth edition), Chapter 43 - Congenital Heart Disease in Infancy and Childhood, W. B. Saunders Company, 2001.
- [2] E. Roberts, L. Quinonez, B. Piekarski and S. E. C.W. Baird CW2, “Expandable Valve for Pediatric Application Constructed From Human Venous Valved Conduit Within a Stent,” *Ann Thorac Surg*, vol. 100, no. 6, pp. 2320-4, 2015.
- [3] J. Veselý, L. Horný, H. Chlup, T. Adámek, M. Krajíček and R. Žitný, “Constitutive modeling of human saphenous veins at overloading pressures,” *J Mech Behav Biomed Mater.*, vol. 45, pp. 101-8, May 2015.
- [4] P. Hammer, E. Roberts, S. Emani and P. D. Nido, “Surgical reconstruction of semilunar valves in the growing child: Should we mimic the venous valve? A simulation study,” *J Thorac Cardiovasc Surg*, vol. 153, no. 2, pp. 389-396, Feb 2017.

Chapter 1

Clinical background

1.1 The human heart

The heart is the motor and the main organ of the circulatory system. It functions as a pump and provides a continuous flow of blood throughout the whole body.

1.1.1 Anatomy of the heart

The heart is a muscular organ that pumps blood through the circulatory system, and it is divided in four cavities: two atria and two ventricles. The right atrium collects de-oxygenated blood from two large systemic veins, i.e., the superior and inferior vena cava. When the atrium contracts, blood is pumped into the right ventricle. The latter, in turn, ejects blood into the pulmonary circulation through the pulmonary arteries. The left atrium, instead, receives oxygenated blood from the pulmonary veins and pumps it into the left ventricle, which ejects blood into the systemic circulation, through the aorta, and to all the tissues of the body.

Blood flows from systemic and pulmonary veins to the atria continuously. The flow between each atrium and the corresponding ventricle is regulated by a unidirectional valve, called mitral valve in the left heart and tricuspid valve in the right heart. Ventricles are separated

from and the downstream arteries by two other unidirectional valves, called semilunar aortic valve and semilunar pulmonary valve in the left and right heart, respectively.

From the ventricles, blood flows into two great arteries: the aorta, which takes blood from the left ventricle to the systemic circulation, and the pulmonary artery, which brings the blood from the right ventricle to the lungs (**Figure 1.1**) [1].

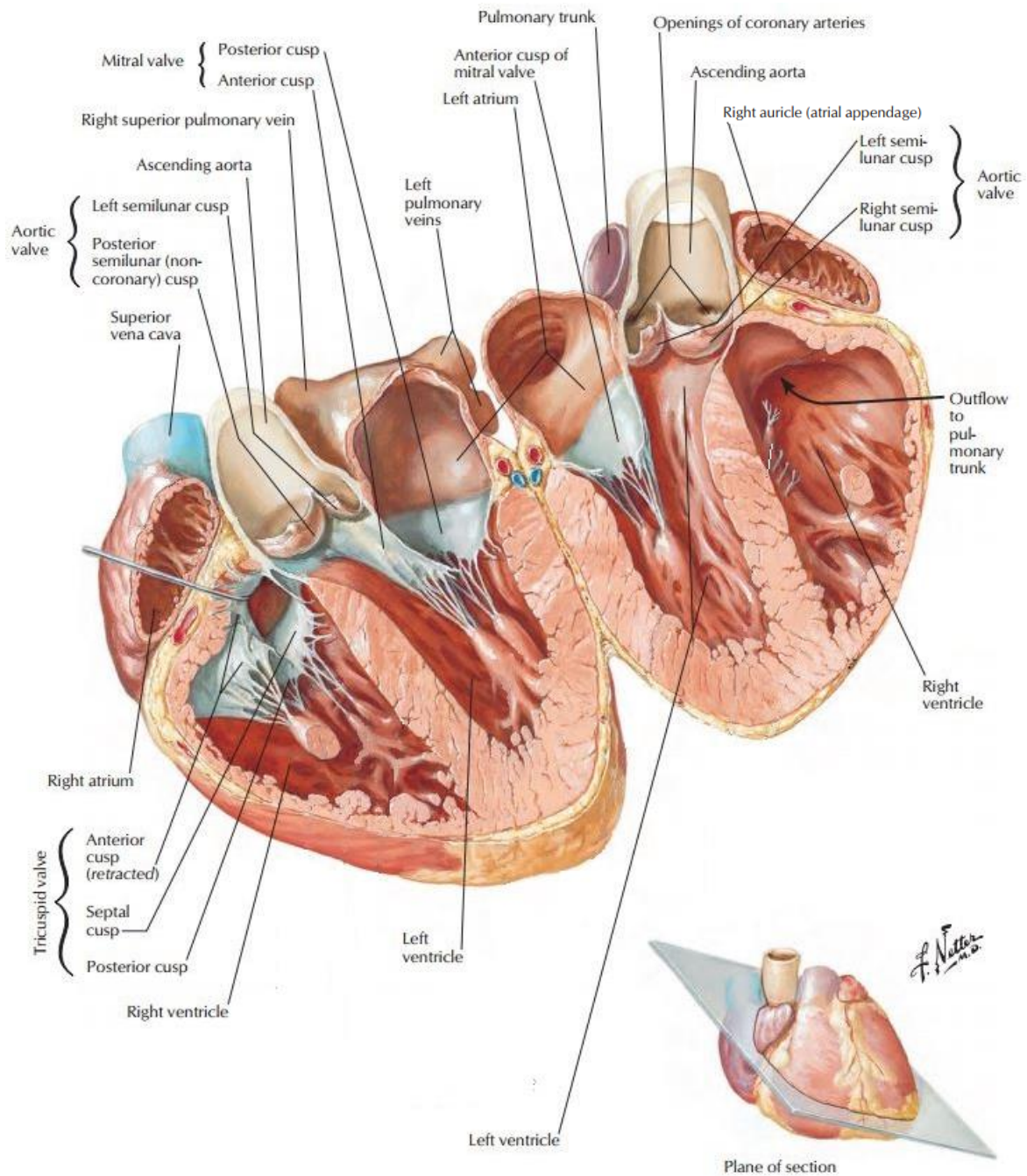


Figure 1.1: Heart and principal vases, ventral view. Adapted from [2].

A typically human adult heart weights 250-350 g and it has about the size of the fist of the respective person. It is located medially between the lungs, in the space known as the mediastinum. The heart is separated from the other mediastinal structures by a double-layered membrane called pericardium, which protects the heart and maintains its position in the thorax.

The wall of the heart is composed of three layers of unequal thickness: the outer epicardium, the middle myocardium and an inner lining layer of endocardium (**Figure 1.2**). The epicardium is the outermost layer of the heart wall and the innermost layer of the pericardium, it is a thin layer of serous membrane. The endocardium is the innermost layer of the wall, it is connected to the myocardium by a thin layer of connective tissue and it is made of smooth endothelium. The myocardium is the thickest layer and is formed mostly by cardiac muscle cells; the contraction of the myocardium allows for blood pumping from the heart and the vascular circulation.

The thickness of the myocardium varies between the chambers: atria have a thin muscular wall; ventricles have a thick muscular layer, much thicker in the left ventricle than in the right one, although the ventricles pump the same amount of blood per contraction. As a matter of fact, the left ventricle must produce a higher amount of pressure to overcome the great hydraulic impedance provided by the systemic circuit, while the right ventricle does not need to generate as much pressure, since the pulmonary circuit is significantly shorter, and it is characterized by a lower hydraulic impedance [1].

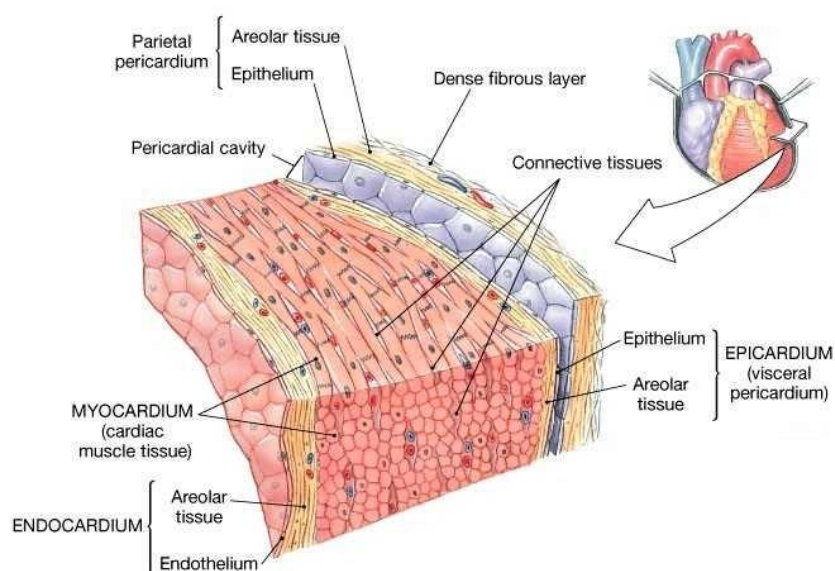


Figure 1.2: Pericardial Membranes and Layers of the Heart Wall.

1.1.2 The cardiac cycle

From a functional point of view, the heart is composed by two pumps in series: the left heart and the right heart. Each one consists of a low-pressure chamber, the atrium, and a high-pressure chamber, the ventricle. The two pumps are synchronized so that first atria and then ventricles contract simultaneously, with an average frequency at rest of 70-75 beats per minutes. The heart pumping activity is cyclic and can be split in two basic phases: the contraction phase, systole, and the filling phase, diastole. The lapse between the beginning of a diastole, or a systole, and the next one is called a cardiac cycle and it lasts approximately 0.8 seconds [3].

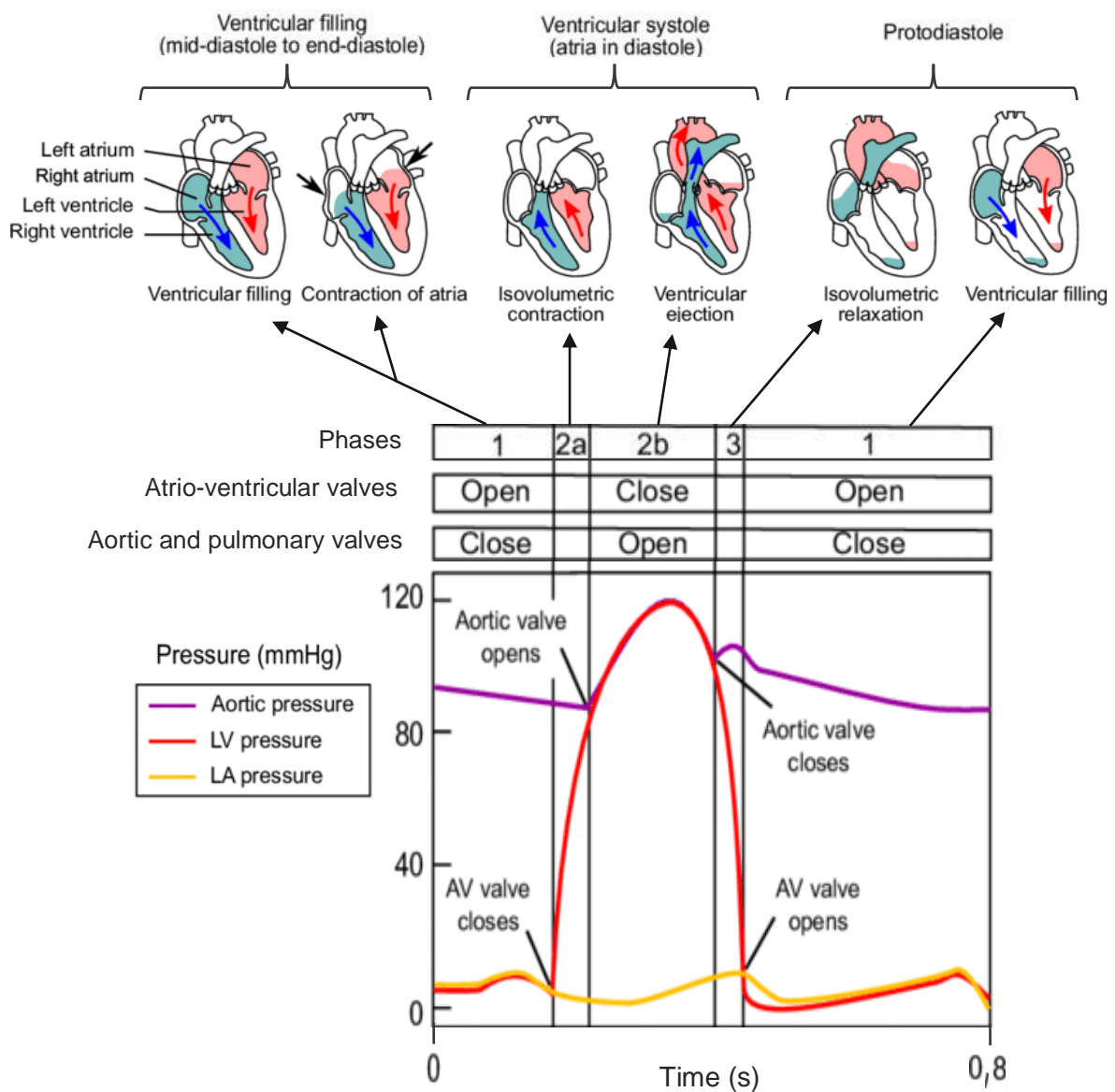


Figure 1.3: Overview of the cardiac cycle phases and the pressures behavior in the left heart during the cardiac cycle.

If we consider ventricular dynamics, during systole both the left and the right ventricle contract and eject blood into the arterial system, while during diastole the cardiac muscle is relaxed, blood flows passively from the veins into the atria and past the atrioventricular valves into the ventricles and then it is pushed into ventricles by atrial contraction (**Figure 1.3**).

Although the contraction dynamics is the same in the left and the right heart, the pressure behavior is very different. The left heart and the aortic arch are a high-pressure system: in physiological conditions, pressures in the left atrium and ventricle range between 0-18 mmHg and 0-120 mmHg respectively, while in the aorta pressure varies between 80 and 120 mmHg. Pressures in the right heart follow the waveform of the corresponding ones in the left heart, but they reach significantly lower values. Pressures in the right atrium range from 0 to 5 mmHg, during atrial systole, while in the ventricle they vary between 0-2 to 25 mmHg, during contraction; in the pulmonary artery the diastolic pressure is 8 mmHg and the systolic one is about 25 mmHg (**Figure 1.3**) [3].

1.2 Congenital heart diseases

Congenital heart disease, or a congenital heart defect, is the phrasing used to indicate an abnormality in cardiocirculatory structure or function that is present at birth, even if it is discovered much later. Congenital cardiovascular malformations usually result from an early developmental problem in the heart's structure, an altered embryonic development of a normal structure or a failure in the complete development of a structure. The anatomical defect may interfere significantly with the structural and functional development of the remainder of the circulation [4].

1.2.1 Hypoplastic Left Heart Syndrome

The hypoplastic left heart syndrome (HLHS) is one of the most complex cardiac defects seen in the new-born. This designation is used to describe a rare congenital heart defect characterized by several aspects: a critical underdevelopment of the left cardiac chambers, or in some cases a complete absence of the left ventricle, atresia or stenosis of the aortic and/or the mitral orifices, and hypoplasia of the aorta (**Figure 1.4**). The degree of underdevelopment differs from child to child.

The left atrium and ventricle are completely unable to support the circulation needed by the body's organs. Pulmonary and systemic circulation are not well separated and, in the heart, oxygenated blood mixes with deoxygenated blood. At birth, this condition allows for the introduction of a part of oxygenated blood in the systemic circulation. In fact, for the first days of life, a dilated and hypertrophied right ventricle acts both as the systemic and pulmonary ventricle: the right atrium receives also pulmonary venous blood from a patent foramen ovale, and the right ventricle pumps blood also to the systemic circulation by way of a patent ductus arteriosus.

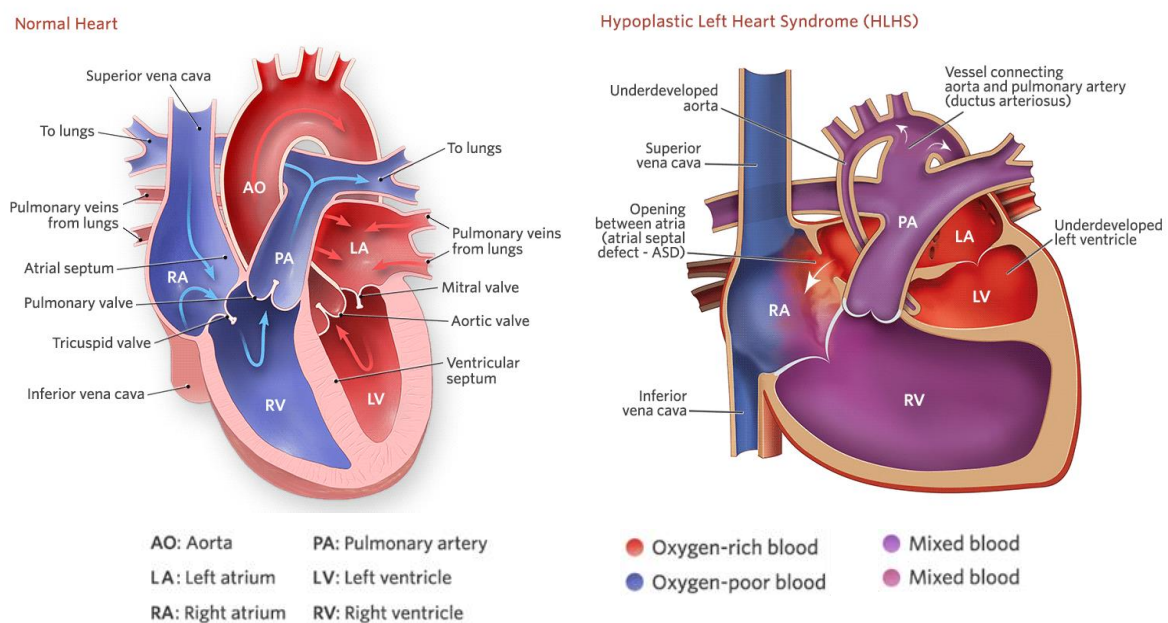


Figure 1.4: Comparison between anatomy and fluid dynamic in physiological heart (left) and in a pathological heart affected by HLHS (right).

If not treated, these anomalies commonly cause heart failure in the first week of life, because after one or two days of life the foramen ovale and the ductus arteriosus close and the right side of the heart has no way to pump blood to the systemic circulation.

Keeping these connections open with medication is necessary to prolong survival beyond the first days of life in babies with hypoplastic left heart syndrome, constriction of the patent ductus arteriosus and limited flow through a restrictive patent foramen ovale are the principal factors responsible for early death.

Stenting of the ductus arteriosus can be used as an ambulatory bridge to transplantation, then, after few days of life, heart surgery is performed [4].

1.2.2 Surgical treatments for HLHS

The treatment of HLHS requires a heart transplant, however, it is possible to initially resort to a three-step surgical procedure, called staged palliation, to delay the actual transplant.

The first stage of this palliation procedure, called Norwood operation (**Figure 1.5**), is performed shortly after birth, within the first two weeks of a baby's life. It consists in the conversion of the right ventricle into the main ventricle, which pumps blood to both the lungs and the body, the creation of a communication between the right ventricle and the aorta, and an enlargement of the ascending aorta.

The connection of the right ventricle and the aorta is accomplished by the creation of a neo-aorta: this can be done using homografts or prosthetic conduits from the right ventricle or pulmonary trunk to the descending aorta, or by direct connection between the proximal pulmonary trunk and the ascending aorta, which also enlarges the ascending aorta. Since the right ventricle is no longer directly pumping blood to the lungs, pulmonary blood flow and pressure are controlled by a systemic-pulmonary shunt to the distal pulmonary artery. The patent ductus arteriosus is ligated. A large interatrial communication also must be ensured in stage 1 to allow for free access of pulmonary venous blood to the tricuspid valve.

The systemic-pulmonary connection can be achieved in different ways. In classic Norwood pulmonary blood flow is supplied by a modified Blalock-Taussig shunt (MBT), which connects the subclavian or innominate artery to the pulmonary artery. This type of shunt provides continuous blood flow to the pulmonary circulation, during both systole and diastole, causing retrograde diastolic flow in the descending aorta and in the coronary arteries. This anomalous coronary blood flow may cause circulatory instability.

Pulmonary over-circulation through a systemic-pulmonary shunt has been one of the major causes of early death after the Norwood procedure. To avoid this lethal complication, it is possible to use a Sano or RVPA shunt, which is placed directly between a small right ventriculotomy and a distal stump of the pulmonary artery. The result is that a single ventricle, the right one, is linked to both the aorta and the pulmonary artery. This variant has the advantage of the elimination of diastolic runoff, reducing coronary steal, providing a stable systemic circulation as well as an adequate pulmonary blood flow and a better transplantation-free survival at 12 months. Nevertheless, potential disadvantages of the RV-PA conduit may be ventricular dysfunction, aneurysm formation, and arrhythmias after ventriculotomy [5] [6].

Norwood operation

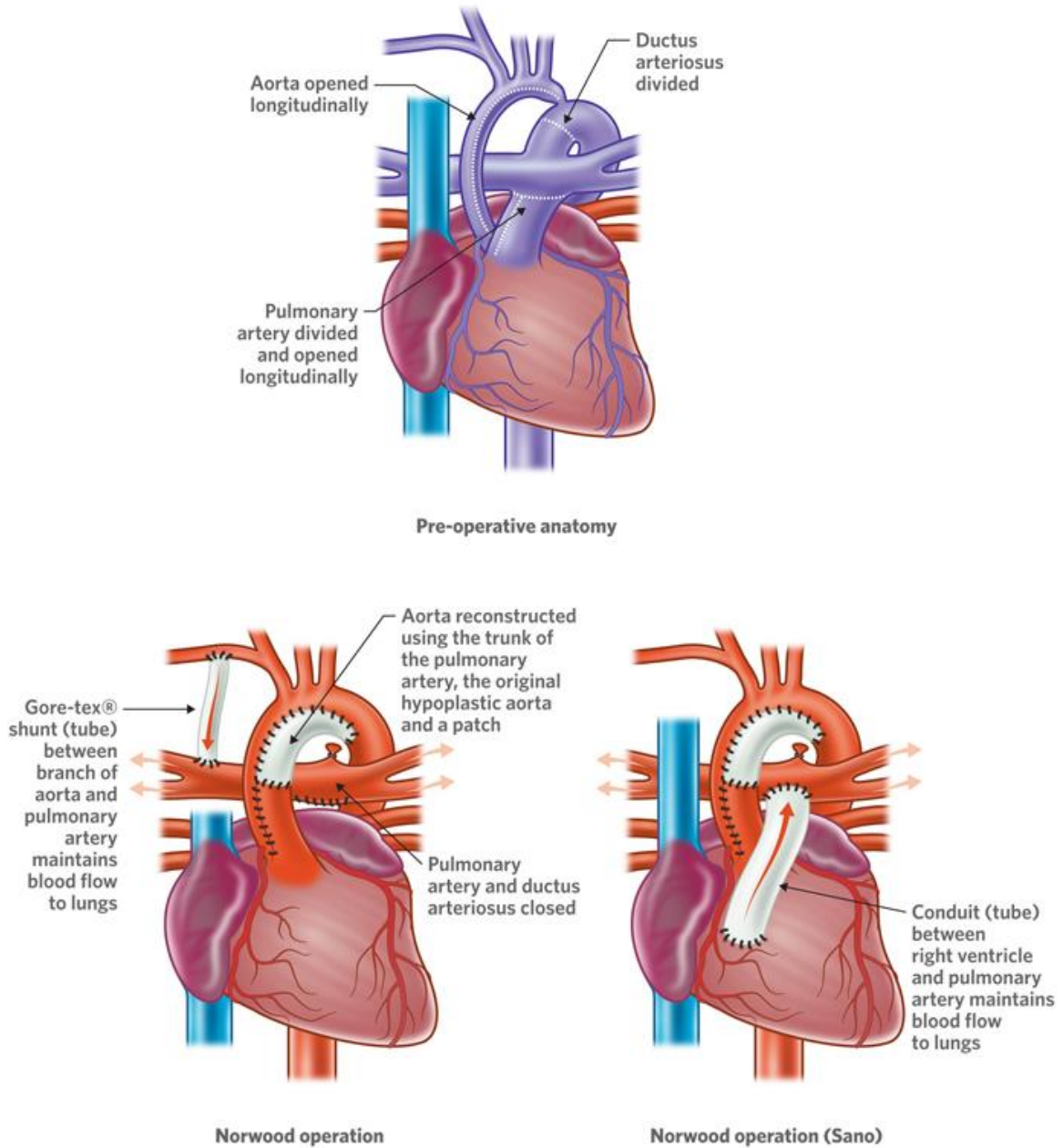


Figure 1.5: Stage I. The Norwood procedure, with the two possible systemic-pulmonary shunts.

The second stage of the palliation of HLHS is the hemi-Fontan procedure (**Figure 1.6**) (or bidirectional Glenn operation), which is usually performed within the first six months after birth. During this surgery, the shunt previously inserted is removed and the superior vena cava is disconnected from the heart and attached to the pulmonary artery. This allows blood returning from the body to flow directly to the lungs, without passing through the heart, and reduces the work that the right ventricle has to do.

Bidirectional cavo-pulmonary connection (BCPC)

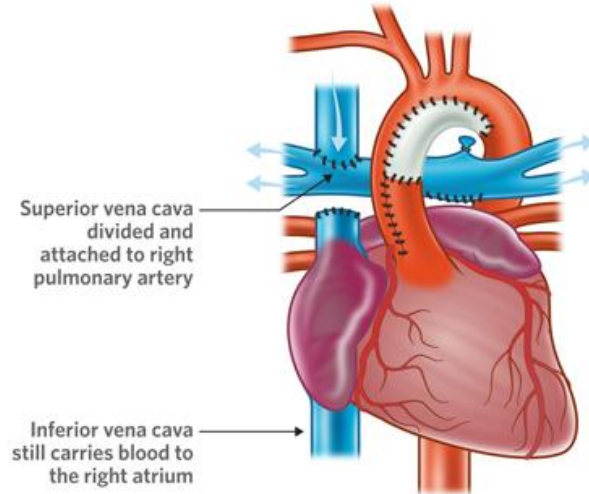


Figure 1.6: Stage II. Bi-directional Glenn Shunt Procedure.

The third and last stage of this surgical treatment is the Fontan procedure (**Figure 1.7**). It is usually performed between the eighteen months and the three years of age of the patient. During this surgical operation the inferior vena cava is disconnected from the heart and attached to the right pulmonary artery. Once this procedure is complete, the deoxygenated blood from the systemic circulation goes to the lungs without passing through the heart, so oxygen-rich and oxygen-poor blood no longer mix. Therefore, the two circulations in series, systemic and pulmonary, are restored.

Fontan operation

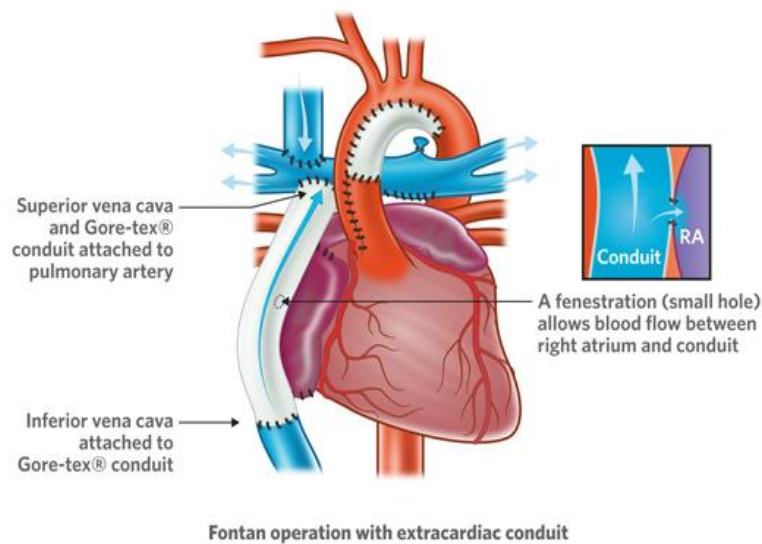


Figure 1.7: Stage III. Fontan Procedure.

1.2.3 Innovative surgical procedures for first stage treatment of HLHS

It has been shown that patients with hypoplastic left heart syndrome which receive a right ventricle-to-pulmonary artery (RVPA) conduit in stage I Norwood palliation have a higher incidence of transplant-free survival as compared to those who receive a modified Blalock-Taussig shunt. This happens because the use of a Sano or RVPA shunt avoid lethal complication caused by coronary steal and the subsequent circulatory instability [6]. However, the RVPA group has more unintended inter-stage interventions, mainly for balloon dilation or stent placement, due to proximal conduit stenosis.

To overcome a potential drawback of proximal conduit compression, the Clinic for Cardiovascular Surgery and Department of Pediatric Cardiology of Munich developed a modified Sano technique for Norwood stage I palliation and they began it in 2006. This surgery involved the use of a 5mm stretch vascular Gore-Tex graft with removable rings.

One extremity of this conduit is anastomosed with the right ventricle, the other is inserted either into the pulmonary tree, at the cranial part of this patch, or into the right pulmonary artery (**Figure 1.8**). The use of a ring-enforced polytetrafluoroethylene conduit between the right ventricle and the pulmonary artery in this procedure resulted in an effectively prevention of substernal compression and a reduction of inter-stage morbidity [7].

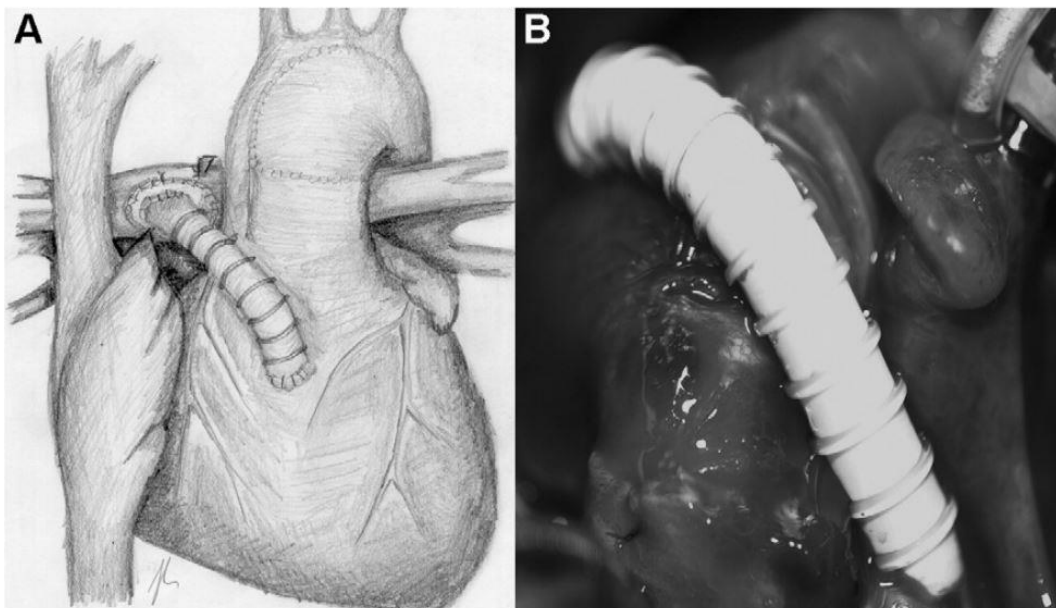


Figure 1.8: Schematic drawing depicts the ring-enforced right ventricle to pulmonary artery conduit directed towards the right of the augmented aorta (A). Intraoperative image shows the ring-enforced conduit after the procedure (B).

This approach has been applied also by the department of Cardiac Surgery of Boston Children's Hospital (Harvard Medical School), since 2010. They used a 5-6mm ring-reinforced expanded polytetrafluoroethylene graft to address potential compression of the proximal RVPA conduit. The proximal portion of the Gore-Tex shunt is inserted transmurally through the right ventricle with a limited ventriculotomy, while the distal part is anastomosed directly to the right pulmonary, or alternatively a gusset of ePTFE or pericardium is used. This ring-reinforcement of the RV-PA shunt provides acceptable results, with a low incidence of inter-stage reinterventions in patients undergoing stage I palliation [8].

Afterwards, the department of Cardiac Surgery of Boston Children's Hospital and the Division of Materials Science and Engineering of Boston University has developed an improved prototype design for the aforementioned surgical procedure. The latter consists in the implantation in the RV-PA position of a cryopreserved venous valved conduit compressed within a bare-metal stent scaffold and sutured at the proximal and distal ends. The shunt is made by an allograft femoral or saphenous vein, while the stent used is a Palmaz Biliary Stent (**Figure 1.9**) [9].



Figure 1.9: Saphenous vein-stent construct (left) and its implant (right).

Pediatric valve replacement options for diameters of less than 15 mm are limited, and all prosthetic valves suffer from having a fixed diameter and from the subsequent inability to adapt to the child growth [10]. Furthermore, the attempts to enlarge RV-PA outflow tract conduits of bioprosthetic valves often result in regurgitation. Everything considered, a cryopreserved allograft femoral or saphenous vein was found to be a suitable source of small-sized expandable valves, because of venous valves capability of retaining competence over a wide range of sizes. Moreover, these venous conduits provide a thin support structure

surrounding the valve, with a high internal diameter (ID) to outer diameter (OD) ratio, making them convenient for intracardiac implantation within small annuli, and the leaflet tissue texture matches that of a neonate or infant.

This expandable design was tested *in vitro*, confirming valve competence, and then used for implantation in the RV-PA position in 2 patients in whom the presence of a competent valve was clinically desirable. The general surgical procedure consists of sequential phases. First, on the back table in the operating room, the unexpanded stent is pre-expanded enough to fit the vein inner diameter. The vein is inserted into the stent and then the balloon is dilated to the goal size. Afterwards, the externally-stented vein segment is sewn into the patient in the RV-PA position. If clinical monitoring suggests that the shunt allows for too much retrograde flow to the lungs, it might be externally crimped, either in the operating room or later in the intensive care unit, to limit flow to the lungs. On the other hand, if the shunt is too restrictive, it can be balloon-dilated in the operating room or later in the cath lab.

The first patient described in this paper was a 4-day-old child and for the surgical treatment a saphenous vein graft was used, containing an 8-mm OD valve, compressed and sutured within an 8-mm Palmaz Biliary Stent, pre-expanded to 6 mm. At 4 months, the valved construct was balloon-dilated to 8 mm ID, resulting in trivial-to-mild regurgitation. The second patient was a 4-month-old girl for whom was used a 10-mm OD femoral valve segment, compressed and sutured within an 8-mm Palmaz Biliary Stent, pre-expanded to 8 mm.

The prototypal expandable design described in this paper demonstrates *in vitro* the competence of the valve, at a range of diameters, and a satisfactory short-term performance in the RV-PA position in pilot clinical testing. Moreover, valvular competence after expansion was validated in 1 patient 4 months after the initial surgery. This trial has shown that the use of a venous valve allows for favorable ID/OD ratio and effective orifice area, even when the construct is compressed to diameters significantly smaller than the native diameter of the valve. External support with a stent is a crucial design feature of this expandable valve construct, because it is necessary to maintain the valve in a compressed state avoiding the incompetence normally shown by venous valves once expanded beyond a threshold ID [9].

To perform the surgery presented by Roberts et al. [9], one of the stents used was the Palmaz XL Transhepatic Biliary, which was also the stent considered in the current work. It is a bare

metal balloon expandable stent, made of stainless steel (AISI 316L). This stent is a one-piece laser-cut stainless steel slotted tube, with a closed-cell design and no welds, ensuring device integrity.

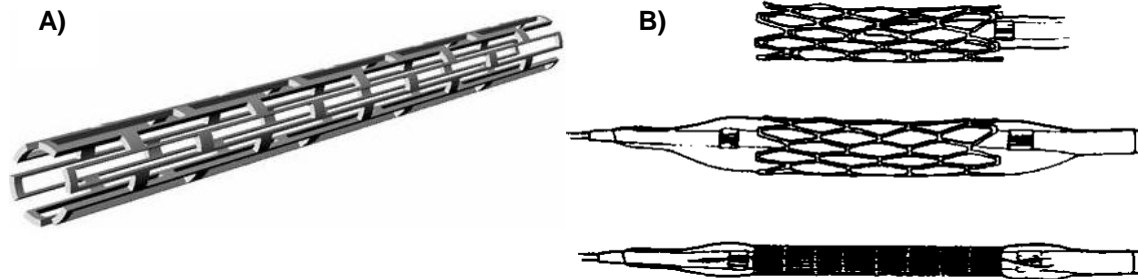


Figure 1.10: Palmaz stent in its initial configuration (A) and its expansion with a balloon (B).

The Palmaz XL Transhepatic Biliary stent is provided unmounted. It is built from a steel tube from which a laser cuts rectangular cells. Once expanded, the stent appears as a multiple vertical sequence of rhombuses, wrapped around a cylinder (**Figure 1.10**). This configuration guarantees high radial strength, optimized flexibility, easy deliverability and minimal foreshortening.

Chapter 2

State of the art

2.1 Numerical modelling of HLHS treatment

Hypoplastic left heart syndrome (HLHS) is one of the most severe congenital heart diseases seen in newborns, nowadays treated by heart transplant or by a three-step surgical procedure. To provide a lower incidence of post-operative complications to these baby patients, innovative surgical procedures have been developed for the first stage palliation of HLHS treatment. A significant example is the one of Boston Children's Hospital [9], consisting of a vein conduit RV-PA shunt, reinforced by a stent. The latter provides several benefits, such as: prevention of blood reverse flow into the right ventricle using a valved conduit; reduction of the shunt diameter by crimping of the stent, in case of patients with pulmonary hypertension; re-expansion of the RV-PA conduit, accommodating it to the child's growth. However, this crimping is done manually and so there is a high risk of inaccurate maneuvers that can result in an irregular conformation of the shunt and thus an increase in the hydraulic impedance of the conduit, leading to the development of pulmonary hypertension. This pioneering use of a stent sewn and crimped on the outer surface of a vessel has no match in scientific literature and the impact of the aforementioned procedure has not yet been studied.

Numerical modelling could help gaining insight into such potential effects. For many years, computational modelling and simulation studies have been used to support clinical applications, such as design of medical devices or selection of best suited surgical procedures. Numerical simulation techniques are taking an increasingly important role in the engineering field, because they allow to predict the dynamics and the behavior of very complex systems by approximately solving the equations that describe their mechanics. Furthermore, a computational model can provide accurate results without the costs and complications of an experimental approach, and this makes it a useful method of investigation and study.

Numerical models are used to solve boundary value problems, whose physics can be described by partial differential equations with the imposition of proper boundary conditions. For this kind of problems, the exact analytical solution is not always available, especially for the most complex situations. Therefore, numerical models are often used to overcome these limitations and provide an approximate solution to the problem.

In particular, in this work the Finite Element (FE) method was chosen, which consists in the discretization of the differential operator in the equations that describe the physical phenomenon to be represented. The FE method is particularly indicated in structural mechanics problems, which focus on the consequences of the application of specific loads and displacements on deformable solids.

In the FE method the continuous domain, with infinite degrees of freedom, is divided into a collection of subdomains and discretized with a set of simpler, finite dimensional elements. The latter are characterized by elementary forms and they are interconnected in predefined points, called nodes. The grid obtained by this process is called mesh. In each one of these elements the solution of the problem is assumed to be expressed by the linear combination of functions, called basis functions or shape functions, which link the degrees of freedom in a generic point of the finite element to the value of the corresponding degrees of freedom at the nodes.

A variety of factors contribute to obtain a suitable FEM model: the quality of the discretization of the geometry, the selection of adequate mechanical properties for the materials, the use of the appropriate boundary conditions, such as external loads and kinematics constraints, and the proper definition of the interactions between the different part of the system. Therefore, in order to perform a robust computational simulation of the

aforementioned surgical procedure [9], first of all, it is necessary to find a suitable modeling of its components.

2.1.1 Palmaz stent FE models

The FE modeling of stents and of their behavior after implantation is well established and allows for investigating various aspects, including the stent deployed geometry, the resulting stress distributions and the strain patterns, and the stresses induced on the surrounding native tissues.

As for the Palmaz XL Transhepatic Biliary stent in particular, clinical, experimental and computational studies regarding various aspects of its application can be found in scientific literature; however, these studies concern only the evaluation of the stent expansion, having as rationale the use of the device for intra-lumen implantations.

In [11], FE models were used to study the deformation and stress distribution of a stainless steel Palmaz stent after balloon dilatation. Three different numerical models were used: Panel, based on the assumption of a cyclically symmetrical condition; RUG (repeated unit cell), which exploited the periodicity exhibited by the stent in the longitudinal direction; RUG⁺, which consisted of a RUG model with the addition of the stent free margin reproduction (**Figure 2.1**).

The stainless steel stent was described as a bilinear isotropic elasto-plastic material with an elastic modulus equal to 193 GPa, a shear modulus of 692 MPa, a Poisson ratio of 0.27 and a 207 MPa yield strength.

The stent geometry was meshed using eight-node linear hexahedral elements with reduced integration (C3D8R), i.e., with only one Gauss point in the element (**Figure 2.1**).

Using the proposed model, the mechanical behavior of the Palmaz stent following free balloon expansion was analyzed from multiple standpoints, including the relationship between the expanded diameter and the balloon pressure, the stent dog-boning and stress distributions.

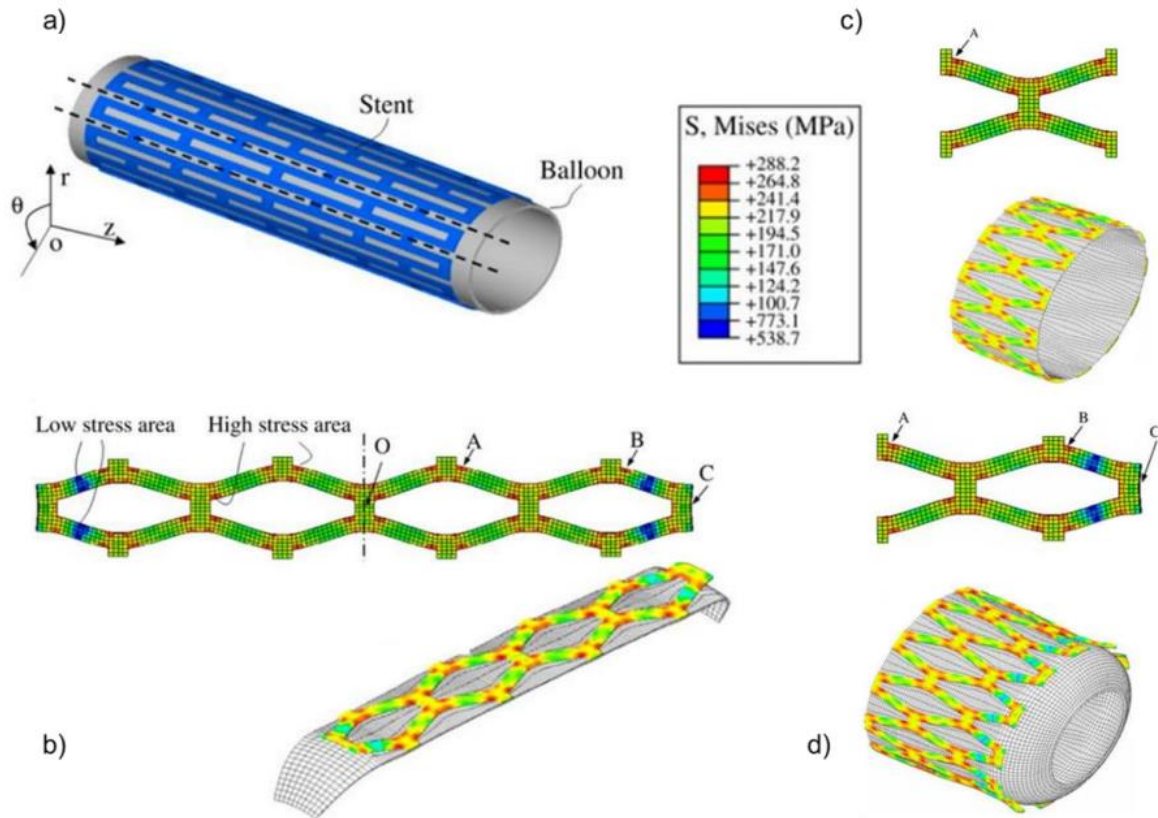


Figure 2.1: Palmaz stent geometry before expansion (a). Deformation and stress distribution of the Palmaz type stent according to the Panel model (b), RUG (c) and RUG+ model (d).

Another paper [12] proposed the study of stent geometrical parameters after non-uniform stent expansion with a balloon, to investigate potential stent design parameters to reduce restenosis risk driven by foreshortening or dogboning. A comparative study of seven commercial stents, including the Palmaz stent, was performed using the realistic FE simulation of the stent expansion with a balloon.

For the stainless steel (AISI 316L Palmaz) stent, an elasto-plastic behavior was assumed, with a Young's modulus of 196 GPa, a yield stress equal to 308 MPa and a Poisson's ratio of 0.33.

Three-dimensional FE models of the stents were created based on manufacture's structural specification, and the stent geometries were discretized using eight-node 3D solid elements with the reduced integration (C3D8R).

A transient non-uniform balloon simulation was performed and all stents showed similar expansion patterns (**Figure 2.2**): at the beginning of inflation, the radial displacement in the distal region of the stent was larger than the central displacement (**Figure 2.2.b-c**), however

the radial displacement in the distal region of the stent was equal to the central displacement at the final phase of the expansion (**Figure 2.2.d**).

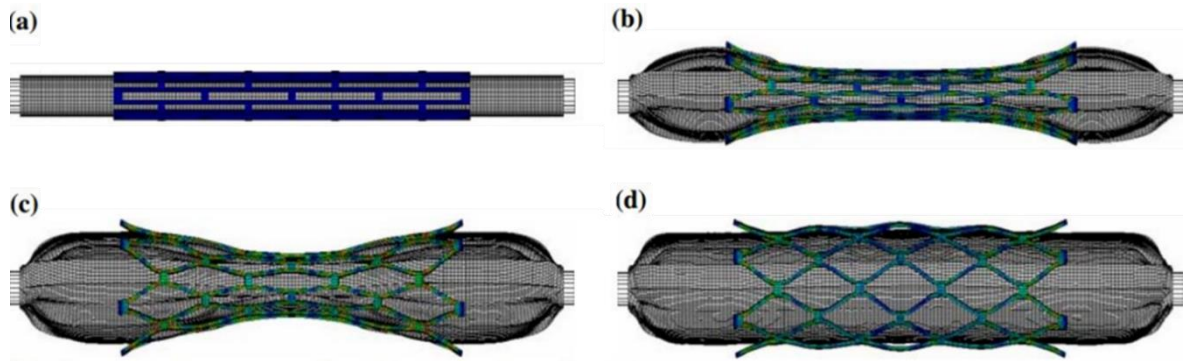


Figure 2.2: Pattern of the transient non-uniform balloon-stent expansion at four different instants during the expansion process. Palmaz stent is shown (a) before expansion, (b) and (c) during expansion, and (d) after expansion.

The pressure-diameter curves predicted from this FE simulations compared favorably with those reported in literature. The changes in axial length and the radial displacement in the central and distal regions of the stent were evaluated and used to calculate stent foreshortening and dogboning. The results obtained from the different stent types considered were compared: generally, the stent with closed unit cells connected to themselves or by a bar link structure had higher foreshortening values with respect to the ones with the opened unit cells connected by bend-shaped connector link structures; the dogboning values were positive for all stents.

As for the application of a Palmaz stent sewn outside a vessel [9], crimped or unloaded, there are no studies in scientific literature that evaluate experimentally or computationally the potential risks of this procedure.

2.1.2 Saphenous vein

The saphenous vein is a large subcutaneous vein that runs through the entire lower limb, starting from the foot up to the groin area. It is the longest vein of the human body.

Human saphenous conduits have an established use in clinics, in particular in the field of cardiovascular surgery. In fact, this type of vein is one of the major possible sources of vascular grafts to be used as autografts or allograft during surgical procedures. For example, the use of autologous saphenous vein grafts is the gold standard in coronary and peripheral bypass surgery [13].

However, their behavior at implant sites is not always easily predictable, because of the remodeling phenomena that may occur after the intervention, especially if they are used in procedures where they are subjected to conditions very different from their physiological environment. This happens particularly in some surgical operations where a saphenous graft can be used to replace or to connect arterial segments. Vein properties are optimized for a mechanical environment that is very different from the arterial conditions, in particular due to the much lower pressure loads. Consequently, after surgery remodeling processes are triggered and modulated by the high blood pressure, flow rate and oscillatory wall shear stresses [14].

Therefore, computational simulations of the vein behavior in these specific procedures it could be clinically relevant, in that these could assess the stresses that veins have to bare when they are subjected to arterial pressure loads, as well as a measure of their compliance and of other factors with significance for the considered application. Nevertheless, in contrast to the work done on arteries, there is a lack of scientific literature on this kind of studies. In particular, only few papers describe the multi-axial nonlinear mechanical response of vein wall tissue or propose the realistic constitutive modeling of venous wall mechanical properties.

To the best of my knowledge, the study published by J. Vesely in 2015 [15] is the only one presenting a comprehensive set of material parameters for human saphenous veins, modelled as a thick wall tube suitable for describing multi-axial stress states. Fifteen samples of vena saphena magna, collected either during coronary-artery bypass surgery or during autopsies, were placed in the physiological solution and mechanically tested in 3 h after excision. The specimens were without side branches and they had a minimal length of 40 mm. Vein samples were marked with a black liquid eye-liner and used in inflations tests: after four pre-conditioning cycles, specimens were pressurized by an intraluminal pressure ranging from 0 up to about 15 kPa using a motorized syringe.

The intraluminal pressure was monitored by pressure transducer and the deformed geometry was recorded by a CCD camera (**Figure 2.3**).

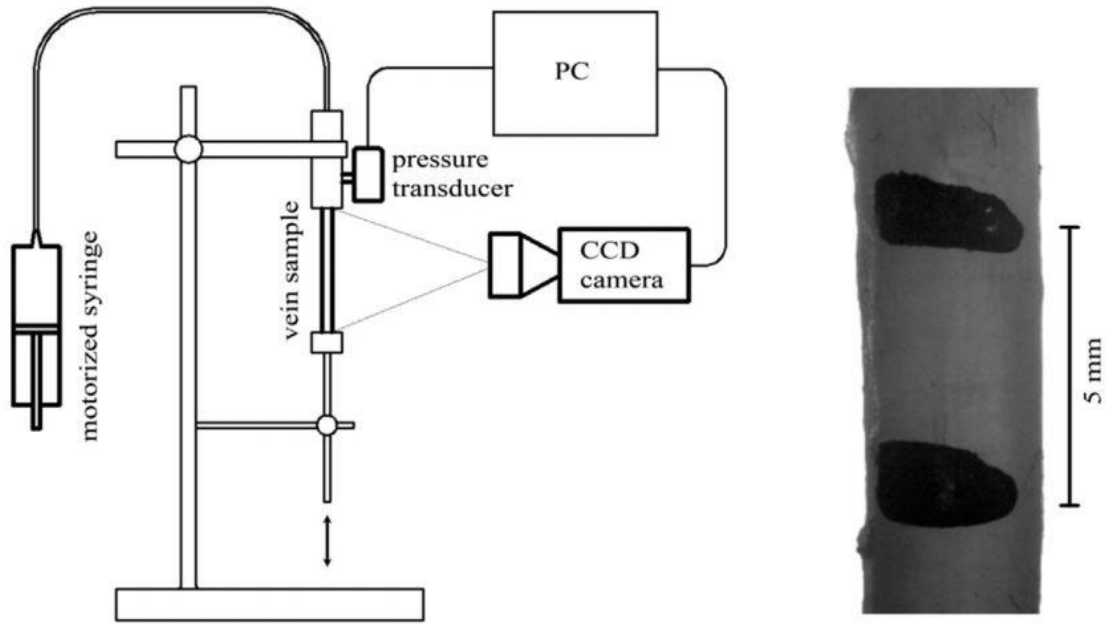


Figure 2.3: Drawing of the experimental inflation–extension test set-up (left), and a picture of a vein sample taken with a CCD camera (right).

The changes in the length and average changes in the silhouette, between the black marks, were determined in the data post processing, using the edge detection algorithm in Matlab (MathWorks, Natick, MA, USA). Then, the axial stretch ratio and the circumferential stretch ratio at the outer radius were computed.

The analytical description of the venous wall tissue stress-strain response and the corresponding pressure-OD response of the samples were derived upon assuming that veins were homogeneous, incompressible cylindrical thick-walled tubes, stress-free in their cylindrical configuration (i.e., with no residual stresses). In this process, the saphenous vein tissue was considered anisotropic and hyperelastic, and it was characterized through the Holzapfel model. In that model, tissue anisotropy arises from the presence of two families of fibers, symmetrically aligned with respect to the circumferential direction of the cylindrical geometry, forming angles β and $-\beta$ with respect to it. Hence, the strain energy density function, W , is defined as:

$$W = W_{isotropic} + W_{anisotropic} = \frac{\mu}{2}(I_1 - 3) + \frac{k_1}{2k_2} \sum_{i=4,6} \{exp[k_2(I_i - 1)^2] - 1\}$$

Where I_1 is the first invariant of the right Cauchy-Green strain tensor, \mathbf{C} , with a positive stress-like material parameter μ . I_4 and I_6 are additional strain invariants arising from the existence of two preferred directions.

$$\mathbf{C} = \mathbf{F}^T \mathbf{F}$$

$$I_1 = \lambda_r^2 + \lambda_\theta^2 + \lambda_z^2$$

$$I_4 = I_6 = \lambda_\theta^2 \sin^2 \beta + \lambda_z^2 \cos^2 \beta$$

The terms λ_r , λ_θ and λ_z represent, respectively, the radial, the circumferential and the axial stretch ratios, while β denotes the inclination of the fibers from the circumferential axis.

The constitutive equation for an incompressible hyperelastic material can then be written as:

$$\boldsymbol{\sigma} = 2\mathbf{F} \frac{\partial W}{\partial \mathbf{C}} \mathbf{F}^T - p\mathbf{I}$$

Here $\boldsymbol{\sigma}$ represents the Cauchy stress tensor and p is an undetermined multiplier induced by incompressibility constraint.

In this study, the material parameters (μ , k_1 , k_2 , β) of the constitutive model were determined by fitting the analytical solution provided by the Holzapfel model for an inflated thick-walled hollow cylinder to the experimental data.

In these experiments it was observed that the saphenous veins are characterized by an initial highly deformable behavior in the pressure–circumferential stretch response, followed by progressive large strain stiffening. Vein samples were much stiffer in longitudinal direction. This behavior was well fit by the theoretical model assumed (**Figure 2.4**, **Figure 2.5**).

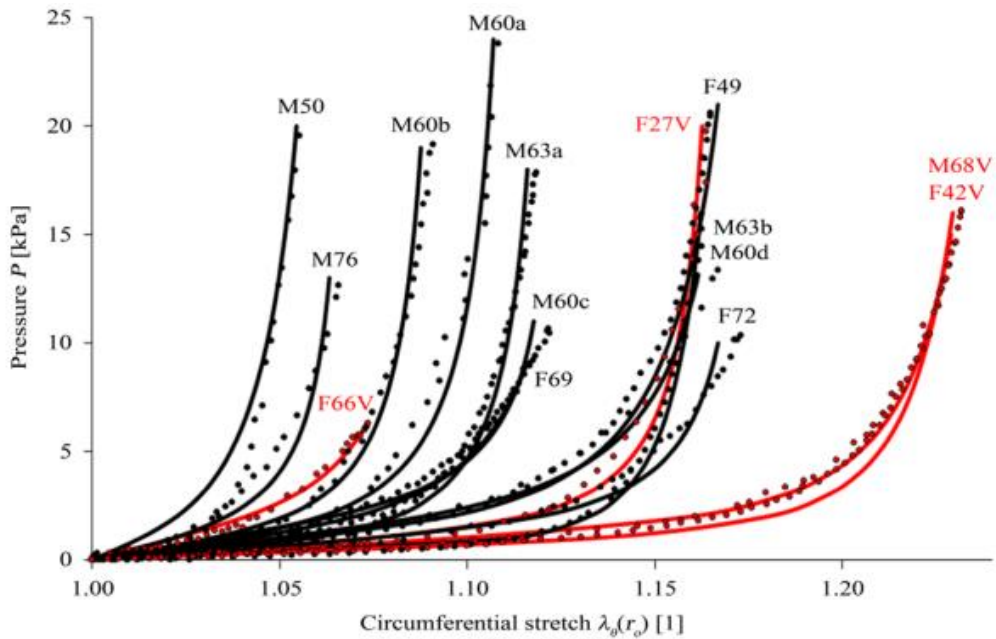


Figure 2.4: Pressure–circumferential stretch at the outer radius: experimental data (dotted curves) are compared with data predicted by the constitutive model (solid curves). The donors with varicose disease are in red.

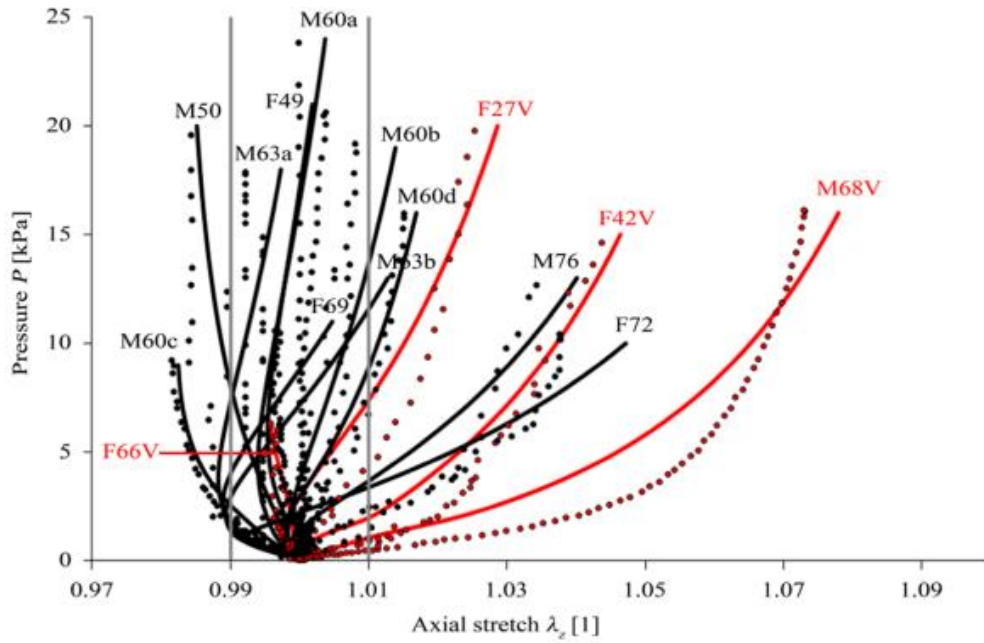


Figure 2.5: The resulting pressure-axial stretch dependences. The experimental data (dotted curves) are compared with data predicted by the constitutive model (solid curves). The donors with varicose disease are in red. The interval in axial stretch from 0.99 to 1.01 in panel B identified by gray lines represents bounds of uncertainty caused by resolution of digital cameras.

The material parameters obtained and presented in this paper are suitable for use in mechanobiological simulations of the autologous vein wall adaptation after bypass surgery and they can be helpful as input in numerical simulations of this kind.

2.1.3 Venous valve leaflets

One of these studies that tackled this aspect is [16], which reports results from a 3D fluid-structure interaction model of a venous valve. The venous valve geometry was represented in a parametric form, including the valve sinus, as shown in (Figure 2.6).

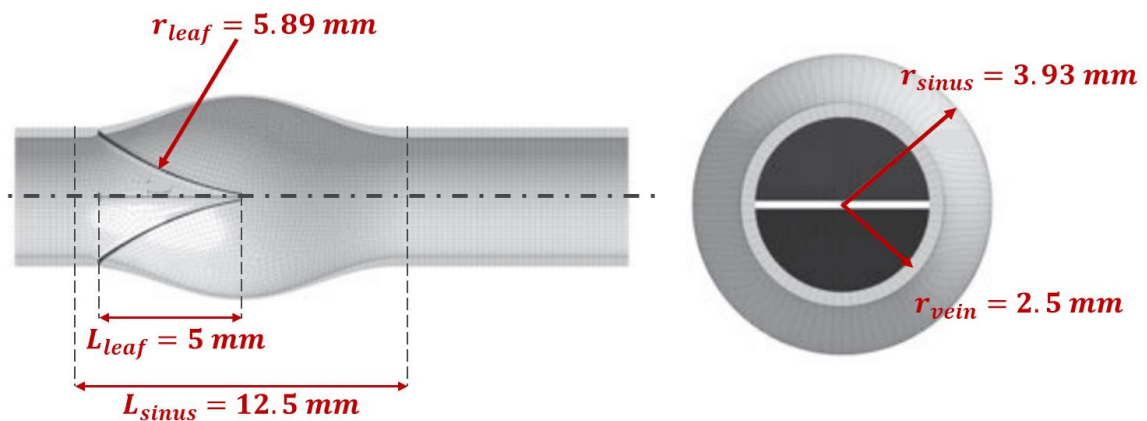


Figure 2.6: YZ view (left) and XY view (right) of solid model mesh geometry used in the paper.

The thickness of the valve leaflets was set to 0.050 mm. The valve leaflets and vessel wall were simulated using a linear elastic material model with Young's modulus 50.7 MPa and 0.507 MPa, respectively, Poisson ratio 0.499 and density $10^5 \text{ kg}\cdot\text{m}^{-3}$.

This geometric model was used to perform the analysis of valve orifice deformation, trans-valvular pressure drops and fluid velocity, for different Reynolds number. The results obtained in this paper can be used to inform 0D models of valve behavior in the context of 1D modelling of circulatory hemodynamics, along with the extension of the model to transient valve behavior and pulsatile flows.

The elastic material hypothesis used for both the vein wall and the valve leaflets represent an acceptable simplification for a fluid-structure interaction simulation, but they can be refined in a structural FE simulation. The same consideration applies to the geometry of the valve leaflets, which in Narracott et al. [16] is defined using a simplified conformation, which does not reproduce the real valve shape.

In another work [17], a different approach to model venous leaflets was proposed. Here, a FE model was used to simulate the ability of a non-growing reconstructed cardiac semilunar valve to close competently in a growing vessel. A three-leaflet design was compared to a two-leaflet design that mimics a venous valve. The proportions between the dimensions needed to characterize the leaflets of the two valve types were obtained by the observation of excised samples of a femoral vein and a porcine valve. In the normal semilunar valve, the axial length of the valve (L_a) is approximately half the vessel diameter. As for the venous valve, the axial length of the valve is almost 1.3 times greater than the vessel diameter and the free edge of the leaflet is considerably longer than the vessel diameter (**Figure 2.7**).

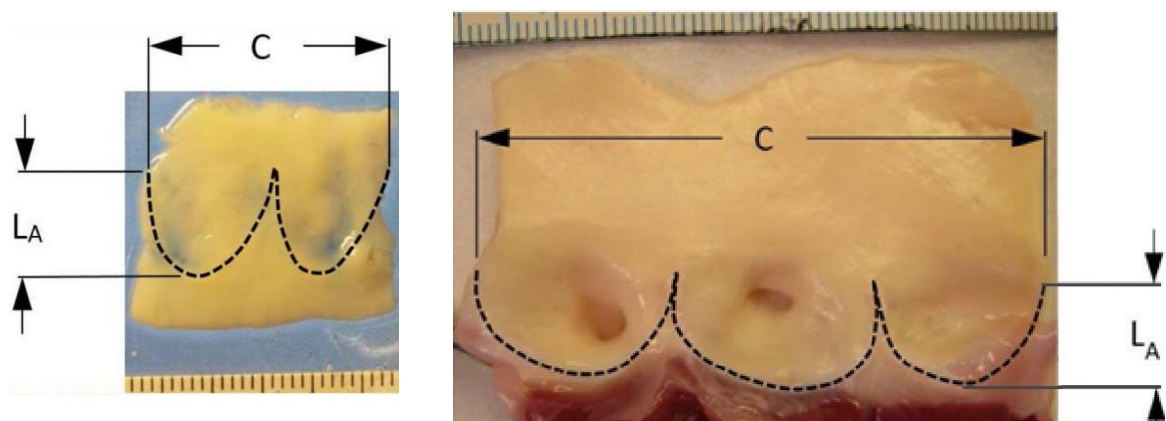


Figure 2.7: Segments of a human femoral vein (left) and porcine aortic valve (right) from which the valve leaflets have been excised. C is the circumference of the vessel at the top of the leaflet attachment, L_A is the length of the leaflet attachment in the axial direction of the vessel. Scales in both photographs indicate mm.

In this study, the authors used a structural FE model of valve leaflet grafts attached to the walls of a cylindrical vessel of varying diameter. The valve closure was numerically simulated to evaluate the possibility of blood regurgitant flow during growth.

To create the bi-leaflet venous valve design, one single human femoral vein was measured, and the resulting leaflets were scaled to shape to a 12 mm diameter root. The planar leaflet outlines were meshed with triangular elements, replicated, and connected to the other component of the system at their endpoints. The planar meshes were wrapped into cylinders to represent the valve leaflet surface in each modelled valve morphology. Three different venous valves were considered, using different ratios of leaflet midline height to circumferential leaflet width: VV1, with this ratio approximately of 40%; VV2 with a ratio equal to 50%; and VV3 with 60%. Approximately 300 triangular elements were used for each mesh (**Figure 2.8**).

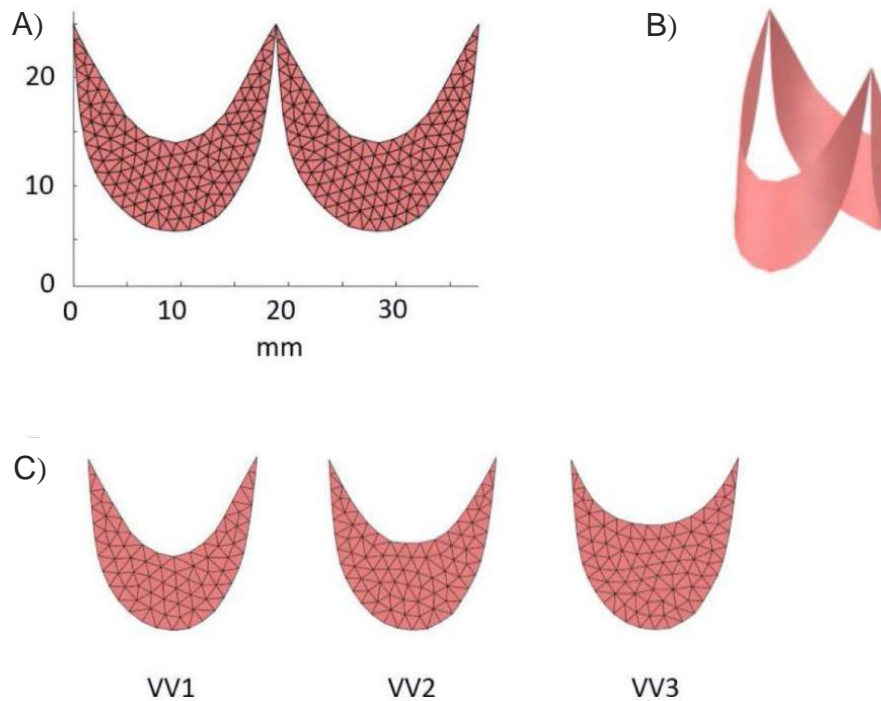


Figure 2.8: (A) Planar outlines of the leaflets from a venous valve design, meshed with triangles and replicated. (B) Planar leaflet mesh wrapped into a cylinder with diameter of 12 mm. (C) The three different venous valve leaflet designs tested: VV1, VV2, VV3.

In this case, the leaflets mechanical properties were described using a Fung-like hyperelastic model, with an exponential strain energy function, W , in the form of:

$$W = \frac{c}{2}(e^Q - 1)$$

$$Q = A_1 E_{11}^2 + A_2 E_{22}^2 + 2A_3 E_{11} E_{22} + A_4 E_{12}^2$$

A_1, A_2, A_3, A_4 and c are constant parameters, while E_{11}, E_{22} and E_{12} are the normal and shear components of the Green strain tensor. The values of parameters c and A_i were chosen to approximate general distensible tissue suitable for valve reconstruction: $c = 50$ kPa, $A_1 = 4, A_2 = 4, A_3 = 0, A_4 = 4$. The leaflets were modelled as a mesh of triangular membrane elements with constant thickness of 0.5 mm.

The structural finite element analysis method that was developed and applied in this work was validated using simulated biaxial loading of square patches of leaflet tissue.

The results of this study show that morphologic features of the venous valve design allow it for a competent closure over a wider range of vessel sizes than the normal semilunar valve design, suggesting its use as a model for aortic or pulmonary valve reconstruction in the growing child.

2.2 Aim of the thesis

Roberts et al [9] presented an innovative procedure for the first stage palliation of HLHS treatment, consisting in the implantation in the RV-PA position of a cryopreserved venous valved conduit compressed within a bare-metal stent scaffold and sutured at the proximal and distal ends. This pioneering use of a stent external to the vessel is not present in scientific literature and the impact of the aforementioned procedure has not yet been studied quantitatively.

Therefore, this thesis work aimed at studying the different geometrical configurations and stress patterns that occur after the crimping of a Palmaz stent on a saphenous vein conduit, using the FE solver Abaqus/Explicit (Simulia, Dassault Systèmes, Providence, RI, USA). This analysis was done both in case of an ideal cylindrical crimping and a malapposition of the stent resulting in an elliptical profile of the reinforced conduit. At first, the shunt conduit was considered as non-valved, then a valved saphenous vein was implemented to assess also the effects of stent crimping on valvular dynamics and valve orifice area.

Chapter 3

Materials and Methods

3.1 Introduction

As previously stated, the aim of this thesis work was to use numerical modelling to evaluate the effects caused to both the saphenous conduit and the vein valve dynamics by different crimping modalities, resulting from ideal or defective crimping in the Roberts et al. procedure [9].

In order to achieve this objective, the geometries of the Palmaz stent, a saphenous vein conduit and a bileaflet venous valve were designed. Their dimensions and their material properties were selected according to pre-existent studies found in scientific literature. For each one of these components, multiple meshes with different element densities were generated and the corresponding results were compared by means of a mesh convergence analysis in order to select the most convenient discretizations for the complete simulation of the surgical procedure.

As in the above-mentioned surgery [9], the Palmaz stent was initially pre-expanded alone and then coupled to the valved saphenous vein, which was inserted in the stent and pressurized. This assembly was then crimped with three different modalities, so to examine

the resulting final configurations of the valved conduit and to assess the behavior of the differently crimped components of the numerical model by means of a stress and strains distributions' evaluation. Moreover, during a successive cardiac cycles simulation, the crimped valve dynamics and the valvular orifice area behavior were studied and compared among the three crimping procedures.

In parallel, it was also assembled an unstented valved venous conduit, to be used as a comparison for the crimped one's dynamics and orifice area.

The schematic workflow that was followed in this thesis work is shown in **Figure 3.1**.

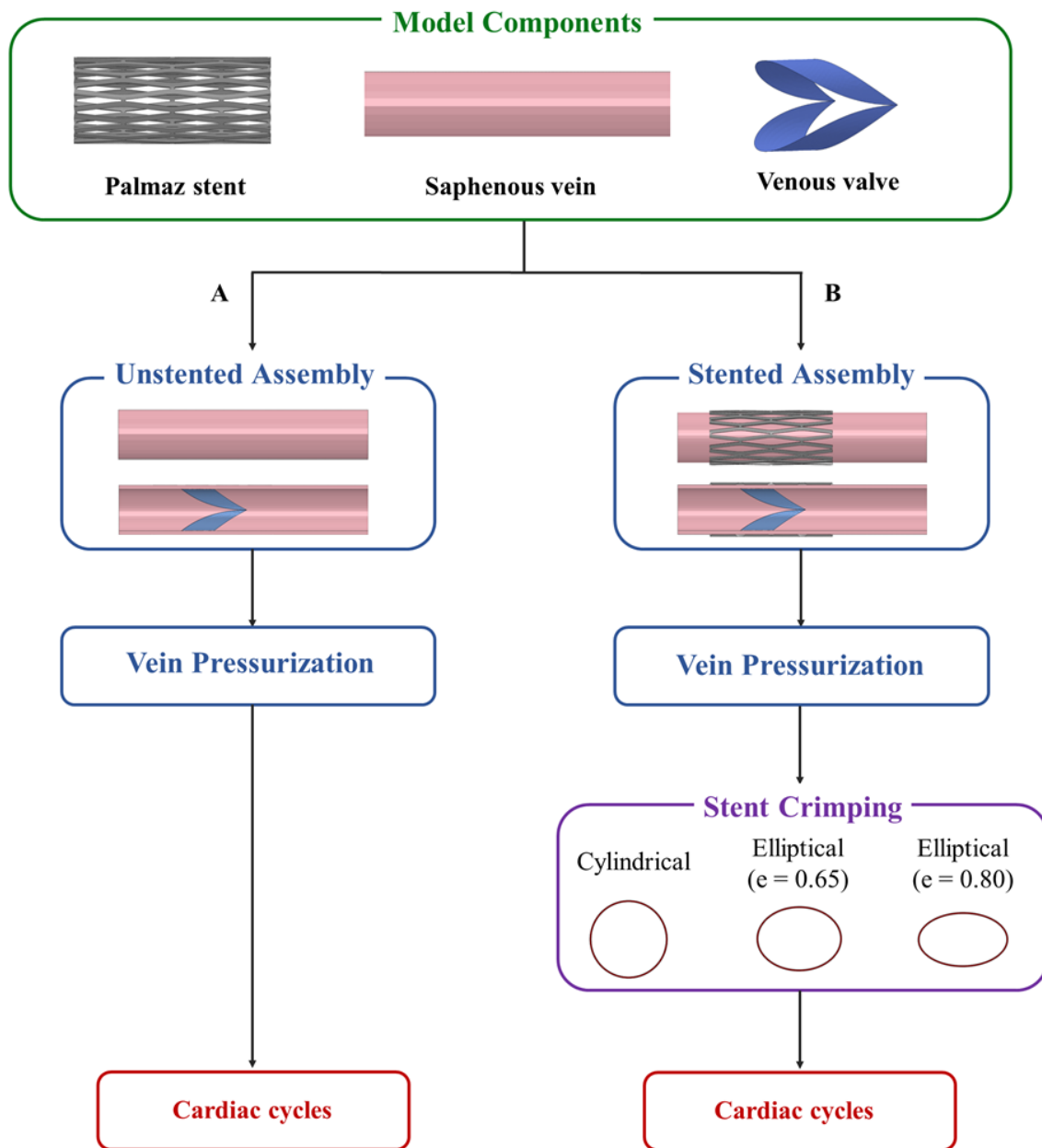


Figure 3.1: Workflow of the thesis and of the subsequent chapters.

3.2 Geometries, meshes and sensitivity analysis

3.2.1 Palmaz Stent

The stent geometry used in this thesis was obtained by direct measurement of the real device. The planar repetitive module of the Palmaz stent was drawn in SolidWorks® (SolidWorks Corporation, Dassault Systèmes, Waltham, MA, USA), it was then repeated 10 times along its axis and 11 times in the perpendicular direction to obtain the planar geometry of the whole stent. The latter was wrapped onto a cylinder with 4.5 mm diameter to build the stent internal surface, which was extruded outwards by a thickness equal to 300 μm . In its unexpanded configuration, the stent had an axial length of 50 mm (**Figure 3.2**).

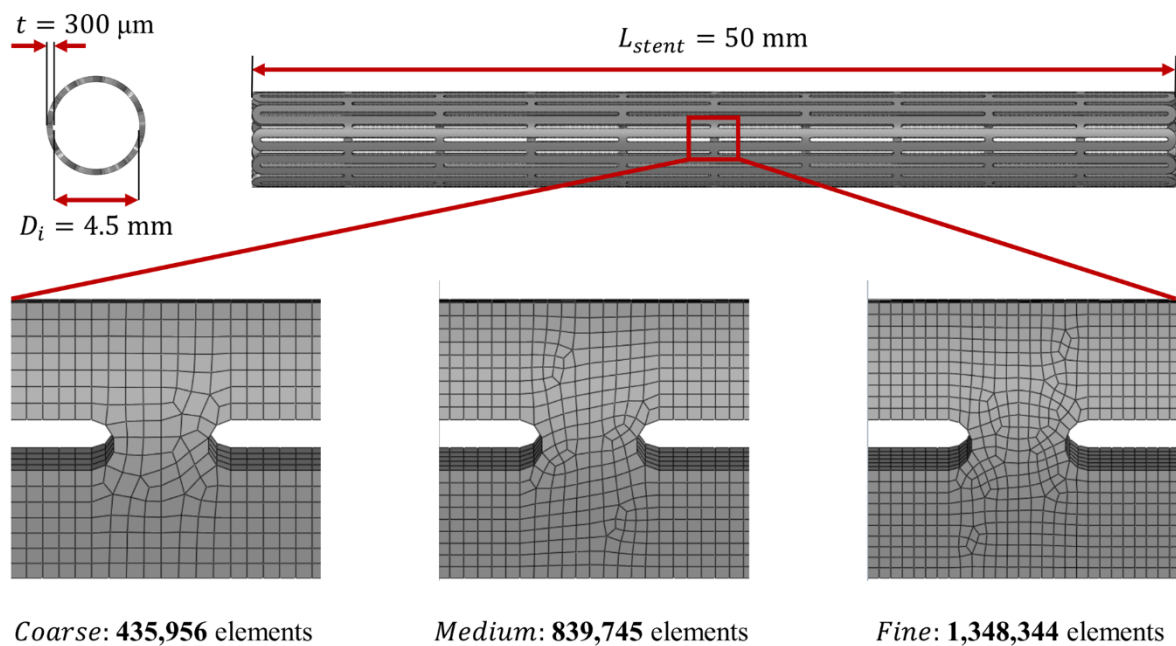


Figure 3.2: Reproduction of the stent geometry. Transversal and longitudinal views of the Palmaz stent with its characteristic dimensions; details of the different refinement in the three meshes used for the convergence analysis.

The geometry of this model was discretized using eight-node 3D solid elements with the reduced integration (C3D8R), accordingly with the indications by published studies [11] [12]. Three different meshes were implemented, with an increasing number of elements (**Figure 3.2**).

An expansion-crimping simulation was performed on the three stent discretizations, using Abaqus. In order to minimize the computational expense of the test, the stent was expanded to an inner diameter of 8 mm by an inner cylinder, which was initially co-axial with the stent

and was radially dilated through displacement boundary conditions. Similarly, the subsequent crimping to a final outer diameter of 6 mm was simulated by radially shrinking an external cylinder, co-axial with the stent and radially reduced through displacement boundary conditions. Both the inner and outer cylinders were 60 mm long and were discretized into 4-node shell elements (S4R) with a characteristic dimension of 0.4 mm. Between expansion and crimping, a stabilization phase took place, in which the stent was free to move, allowing for recoil.

In this simulation, the simulated expansion phase and the crimping phase lasted 300 ms each, while the stent stabilization lasted 200 ms.

The von Mises stress (σ_{vm}) distribution, the equivalent plastic strains (PEEQ, i.e., the sum of the initial equivalent plastic strain and the plastic strain accumulated during the simulation) and the stent recoil yielded by the simulations were analyzed in the mesh convergence analysis.

3.2.2 Saphenous vein

The saphenous vein was modelled as an ideal hollow cylinder, using the mean dimensions of great saphenous veins collected from coronary-artery bypass surgery (CABG), reported by Vesely et al. [15].

The resulting geometry had an axial length (L) of 40 mm, a 4.22 mm external diameter (D_o) and a wall thickness (H) of 0.62 mm.

The vein material was described as an anisotropic hyperelastic continuum, through an Holzapfel model. In this model, the anisotropic behavior is due to the presence of collagen fibers in the material. Fibers are assumed organized in multiple families; within each family, fibers have a preferential mean direction and their direction is stochastically described, accounting for its dispersion. It is assumed that all families of fibers have the same mechanical properties and the same dispersion along the whole length of the venous graft.

In this thesis work, the Holzapfel model was used in the case of an incompressible material with two families of perfectly aligned and symmetric fibers; considering this case, the strain energy density function, U , definition of the model in Abaqus became:

$$U = C_{10}(\bar{I}_1 - 3) + \frac{k_1}{2k_2} \sum_{\alpha=1}^2 \{ \exp[k_2 \langle \bar{I}_{4(\alpha\alpha)} - 1 \rangle^2] - 1 \}$$

Where C_{10} , k_1 and k_2 are temperature-dependent material parameters and \bar{I}_1 is the first deviatoric strain invariant. $\bar{I}_{4(\alpha\alpha)}$ are pseudo-invariants of \bar{C} , the distortional part of the right Cauchy-Green strain and A_α is a set of unit vectors that characterize directions of the fibers in the reference configuration.

The material coefficients needed by Abaqus to implement the Holzapfel model were chosen according to the average values of these parameters estimated in the work of Vesely et al. [15]. The fibers were assumed to be perfectly aligned and the material was considered nearly incompressible, since a perfectly incompressible condition is not allowed in Abaqus/Explicit (**Table 3.1**)

Saphenous vein material		
Density	ρ [t/mm]	$1.04 \cdot 10^9$
material parameter	C_{10} [MPa]	5.85
material parameter	k_1 [MPa]	8.3
material parameter	k_2	0
Fibers inclination with respect to the circumferential direction	[°]	40.6

Table 3.1: Summary of the material parameters values chosen for the Abaqus model of the saphenous vein conduit.

The venous conduit was meshed using eight-node brick elements with reduced integration (C3D8R). Three different discretizations were made, with decreasing circumferential and axial characteristic dimensions, which were set to 0.8, 0.4 and 0.2 mm in the “*Coarse*”, “*Medium*” and “*Fine*” mesh, respectively. There three layers of elements in the radial direction were generated in each mesh (**Figure 3.3**).

These three discretizations underwent a computational simulation that mimicked the experimental test done by Vesely et al. [15], where one end of the saphenous conduit was attached to the cannula of a syringe pump and the other to a stopper, so that one end was sealed and the vessel was able to expand freely in the radial and axial directions when loaded via inflation.

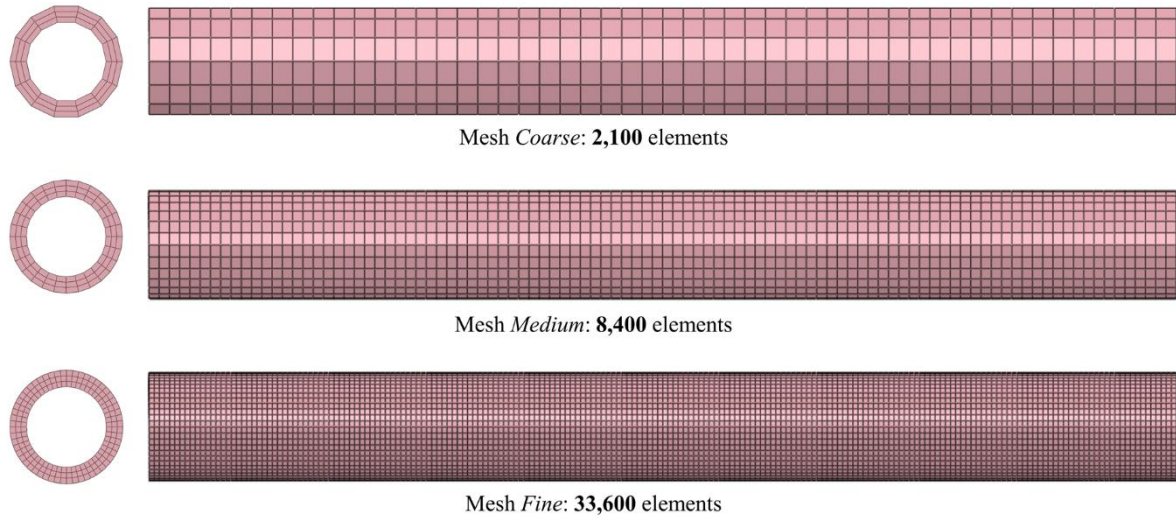


Figure 3.3: Traversal and longitudinal views of the different refinement in the three meshes used for the convergence analysis of the Saphenous vein mesh.

To reproduce this experimental procedure [15], it was necessary to model also the support plate, which was used both to transmit the axial pressure load, that in the real experiment was caused by the liquid inflation, to one extremity of the saphenous vein conduit and to constrain the same vein end to move only along the axial direction.

The plate was discretized into triangular shell elements (S3) with a characteristic dimension that reflected the one of the coupled saphenous vein mesh: 0.8 for the *Coarse* mesh, 0.4 for the *Medium* and 0.2 for the *Fine* one.

The plate material was idealized as linear elastic and isotropic, using the parameters listed in **Table 3.2**.

Plate material		
Density	ρ [t/mm]	$1.2 \cdot 10^9$
Young modulus	E [GPa]	2.3
Poisson's coefficient	ν	0.38

Table 3.2: Material parameters values chosen for the Abaqus model of the plate.

The computational procedure consisted in an inflation-extension test. One extremity of the saphenous vein was constrained in every direction, while the other end was tied to the support plate and forced to move only in the axial direction, following the plate displacement. An intraluminal pressure linearly increasing from 0 up to 15 kPa was imposed on the inner surface of the vein wall and of the plate (**Figure 3.4**).

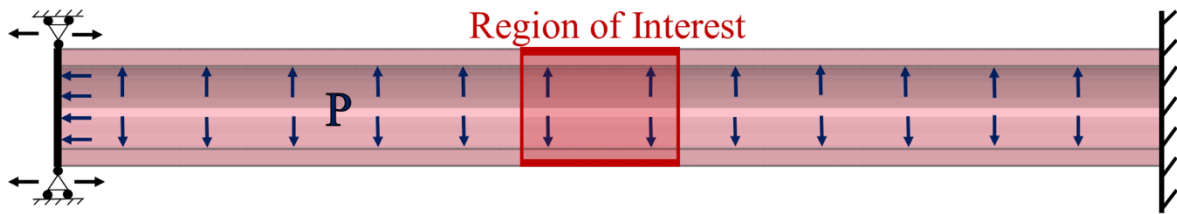


Figure 3.4: Experimental inflation-expansion set-up of Abaqus test.

To reduce the effect of the vein inertial behavior, due to the use of an explicit FEM method, the pressure ramp was applied in a relatively long time: 2.0 s for the smooth pressurization, followed by 0.5 s during which the pressure was hold to the maximal value of 15 KPa.

Moreover, since the inertial behavior could cause an oscillation of the numerical solution, the same inflation-extension computational test was simulated as a static phenomenon using the Abaqus/Standard solver, so to verify that these potential oscillations were caused only by the venous conduit inertia.

The stress and strain behavior during the inflation-extension simulation were acquired in a Region of Interest (ROI) that extended by 5 mm in the axial direction and was centered in the cross-section halfway between the two ends of the vein. In the ROI, the elements facing the outer surface of the vein wall were considered (**Figure 3.4**). This region was chosen both to comply with the displacement acquisition performed in the reference paper [15], and to assume as uniform the stress and strain distribution, due to the distance from the boundaries.

3.2.3 Venous valve leaflets

The saphenous valve leaflet geometry was designed following the same procedure and using the same proportions presented in the paper by Hammer et al. [17]. The leaflets were designed to fit a vein conduit with outer and inner diameter equal to 8 mm and 6.76 mm, respectively. These dimensions characterized the vein model used in the subsequent expansion-crimping computational simulation, that mimicked the aforementioned surgical procedure performed by Roberts et al. [9].

The geometry of one leaflet was drawn in SolidWorks®: the leaflet free margin and the leaflet attachment line was defined as a parabolic and elliptic arch, respectively. The distance between the two leaflet's commissures, L , was set to half the inner circumference of the considered vein vessel. Based on the reference paper by Hammer et al.[17], the height of the leaflet, H , was calculated as 1.3 times the outer diameter of the vein, while the ratio between the leaflet midline height, h , and its total height was set to 0.5 (**Table 3.3**)(**Figure 3.5**).

Leaflet geometry		
Leaflet length	L [mm]	10.4
Leaflet total height	H [mm]	10.6
Leaflet midline height	h [mm]	5.3
Leaflet thickness	t [mm]	0.1

Table 3.3: List of the geometrical characteristics of the leaflet.

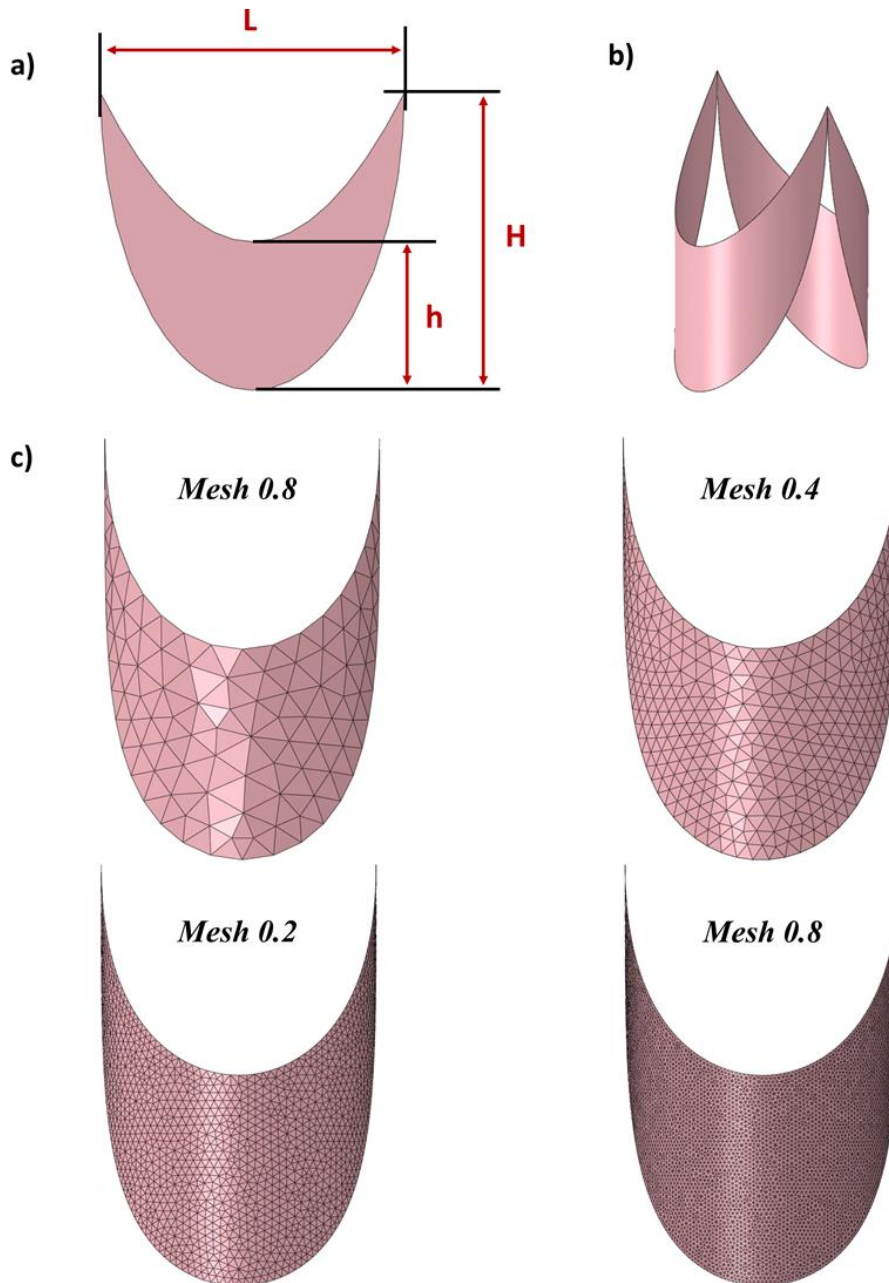


Figure 3.5: a) Planar outlines of the saphenous vein valve leaflet, with its characteristic dimensions. b) Wrapped cylindrical configuration of the two joint leaflets. c) The four different meshes tested in the sensitivity analysis, with the characteristic dimension of their element attached.

The leaflet geometry built with SolidWorks was imported in Abaqus CAE. Here the model was discretized, using triangular membrane elements (M3D4) with a 0.1 mm thickness. Four meshes of decreasing characteristic dimension were generated: 0.8 mm (*Mesh 08*), 0.4 mm (*Mesh 04*), 0.2 mm (*Mesh 02*) and 0.1 mm (*Mesh 01*). Each mesh was wrapped into a hollow cylinder with 6.76 mm inner diameter, corresponding to the internal diameter of the conduit that was used in the test of the valved saphenous vein (**Figure 3.5**).

Accordingly with [17], leaflet tissue was considered almost incompressible and its mechanical properties were described using a Fung-like orthotropic model. In this case, the Fung strain energy function per unit of reference volume, U , of the model in Abaqus has the following exponential form:

$$U = \frac{c}{2}(e^Q - 1)$$

c is a constant temperature-dependent material parameters and Q is defined as:

$$Q = A_1 E_{11}^2 + A_2 E_{22}^2 + 2A_3 E_{11} E_{22} + A_4 E_{12}^2$$

Where E_{11} , E_{22} , E_{12} are the normal and shear components of the Green strain tensor in the membrane plane. The value of the constitutive parameters and of the material density ρ were set as in Hammer et al. [17] (**Errore. L'origine riferimento non è stata trovata.**).

Venous leaflets material		
Density	ρ [t/mm]	1.04*10 ⁹
material parameter	c [KPa]	50
material parameter	A_1	4
material parameter	A_2	4
material parameter	A_3	0
material parameter	A_4	4
material parameter	D	10 ⁻⁶

Table 3.4: Material parameters values chosen for the Abaqus model of the saphenous valve leaflets.

On each valve mesh, the pressure-driven simulation of valve behavior throughout the cardiac cycle was simulated, imposing on the leaflets a pressure that replied the physiological transvalvular pressure of the aortic valve (**Figure 3.6**).

This was due to the application considered in this work for the venous valve: the Roberts et al. surgery [9], in which a saphenous valved conduit was used as a RV-PA shunt in a palliative Sano procedure for HLHS patients. In this pathological case the right ventricle and the pulmonary artery that departs from it undergo pressures much more similar to the ones physiologically developed in the left ventricle and in the aorta.

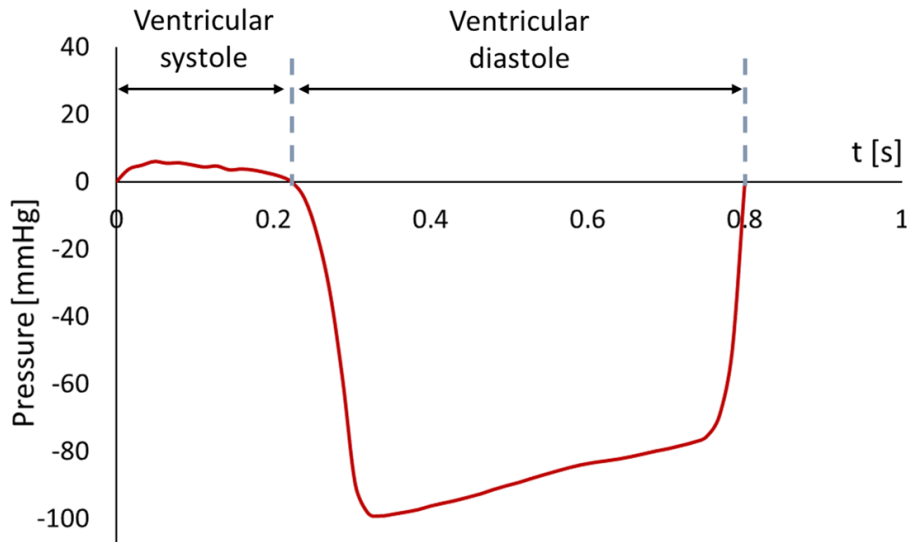


Figure 3.6: Time-dependent pressure curve applied to the saphenous vein leaflets during the simulation.

The leaflets basal margins, normally attached to the vessel wall, were fully constrained during this simulation and a time-dependent pressure was applied to the ventricular surface of each leaflet, as a uniformly distributed surface load. This pressure behavior was modelled according to the study of Sturla et al. [18].

The simulations performed were composed of two complete pressure cycles applied to the valve leaflets, lasting 0.8 s each. The first one was used as settling cycle, since the valve started from an initial configuration that was non-representative of its true dynamics: indeed, *in vivo* the valve is not yet open at the end of the diastole. During the second cycle, maximum principal stress and strain patterns over the leaflets were acquired, together with the valve dynamics and the simulation time.

3.2.4 Mesh convergence study

For all the components, the different discretizations were subjected to a sensitivity analysis, with the aim of choosing the most suitable mesh. Along with computation time, for each component specific biomechanical variables were considered.

Palmaz stent expansion-crimping – bio mechanical quantities were obtained on the whole stent in the most critical stages of the simulations: the end of the expansion, the last increment of the recoil phase and the end of crimping. In particular, the Von Mises stresses and the PEEQ values were compared among the three meshes both after the complete expansion and after the crimping phase, while the difference in radial displacement of the stent nodes between the end of stent expansion and the end of the spring-back phase was used to compute the amount of recoil of the stent during the stabilization. The stress distribution at the considered time-points was characterized by identifying the maximum, mean and minimum value of the von Mises stress distribution, as well as calculating the 90th and the 10th percentiles.

Vein inflation-extension - the maximum principal stresses and the relative strains behaviors during the inflation-extension test were acquired in axial, circumferential and radial directions. With the selected vein mesh, pressure/stretch curves were obtained and compared vs. the curves proposed in of Vesely et al. [15].

Valve function over the cardiac cycle - The time-course of the maximum principal stresses was acquired: the plots corresponding to the stress 10th, the 50th and the 90th percentiles were analyzed. Also, on each leaflet the node nearest to the leaflet belly center was identified the magnitude U of its displacement was acquired over time.

3.3 Saphenous valved conduit cardiac cycles simulation

Once the sensitivity analysis was completed, the venous leaflets and the saphenous vein were assembled. The latter was characterized by the thickness, the axial length and the Holzapfel model parameters previously identified based on Vesely et al. [15]. It was discretized with C3D8R elements with the characteristic dimension chosen from the sensitivity analysis, but with a new outer diameter of 8 mm, to mimic the reference surgical procedure [9]. The nodes of the valve leaflet insertions lines were tied to the inner wall of the saphenous vein conduit. In the modelled surgical procedure, the portion of the ventricular shunt located upstream from the valve is shorter than the downstream portion. Hence, the valve was positioned in the venous conduit so that the upstream and downstream vein section was 9.7 mm and 19.7 mm long, respectively (**Figure 3.7**). In the two subdomains, a ventricular surface and an arterial one were defined, respectively, on the inner surface of the vein conduit.

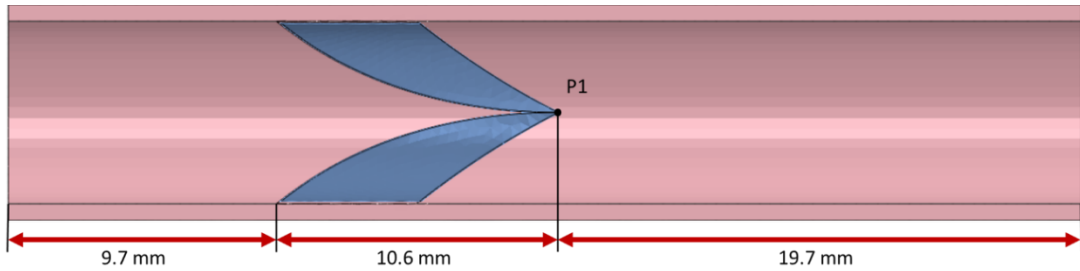


Figure 3.7: Longitudinal section cut of the experimental set-up of the surgical procedure simulation with highlighted the two leaflets' halves and their conjunction point (P1).

The simulation of the system biomechanics during the cardiac cycle consisted of three steps. In step 1, the ventricular and arterial surfaces were loaded by a pressure ramp from 0 to 80 mmHg over a 2.0 s timeframe; in this phase, the valve leaflets were unloaded. In step 2, pressure was kept constant over a 0.5 s time interval, so to obtain a stable condition. In step 3, two cardiac cycles were simulated, each one lasting 0.8 s, by applying three different time-dependent surface pressures, whose definition was borrowed from Sturla et al. [18] and was consistent with the surgical procedure to be mimed [9] and its use for HLHS patients. The vein ventricular surface was loaded by a time-dependent physiological ventricular pressure, the vein arterial surface was loaded by a time-dependent aortic pressure and the ventricular side of the saphenous valve leaflets was loaded by the difference between ventricular and aortic pressure (**Figure 3.8**).

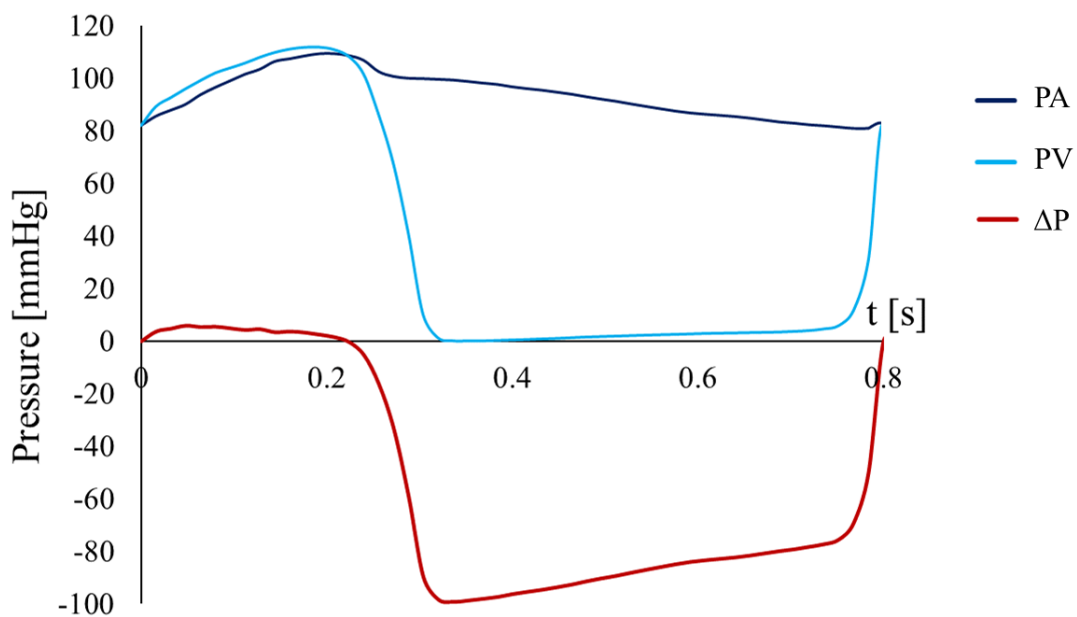


Figure 3.8: Time-dependent pressure curve applied, respectively, to the arterial inner surface of the venous conduit (PA), to the ventricular surface of the vein inner surface (PV) and to the saphenous vein leaflets during the simulation (ΔP).

In each step, the nodes at the two ends of the saphenous vein conduit were constrained allowed only for radial displacements.

A general contact algorithm was used to model contacts between the ventricular surfaces of the two leaflets, between the valve and the saphenous vein inner surface, as well as leaflet self-contact. A scale penalty method was used to model the mechanical interaction in the direction orthogonal to the contacting surface. A 0.1 friction coefficient was set to model tangential load interaction [19].

Valve dynamics and maximum principal stress patterns were monitored throughout the second simulated cardiac cycle; these data were used as baseline reference when analyzing the data yielded by the subsequent simulation of venous duct external stenting [9].

3.4 Simulation of the surgical procedure

The external stenting of the venous shunt and the post-stenting biomechanics of the system were simulated consistently with the features of the procedure to be modeled and with the stent manual crimping characterizing the procedure [9]. Four processes were simulated:

5. stent pre-expansion, so to allow the subsequent insertion of the valved saphenous vein graft in the stent;
6. Stent-vein assembly, vein pressurization up to 80 mmHg
7. Stent crimping, which was simulated in three different modalities to assess the effects of possible distortions associated to manual crimping in the real procedure;
8. Post-stenting response of the system over two cardiac cycles.

3.4.1 Stent pre-expansion

The unexpanded model of the Palmaz stent geometry had a total length of 50 mm, which unsuitable for a stent to be used in to reinforce a RV-PA shunt for the first stage palliation of HLHS treatment. Consistently with the real procedure a 20 mm long tract of the stent was extracted from the entire geometry (**Figure 3.9**).

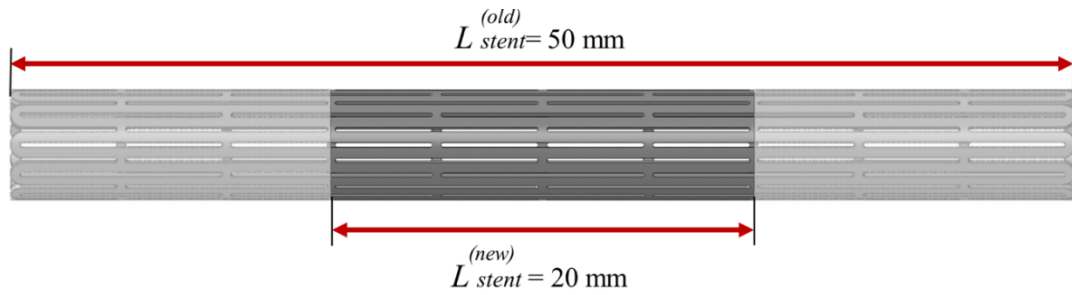


Figure 3.9: Stent old and new dimensions compared.

This new stent geometry was expanded up to an 8 mm internal diameter, using an ideal cylinder with 4 mm diameter. The latter was discretized into 4-node shell elements (S4R) with a characteristic dimension of 0.4 mm. The cylinder was initially co-axial with the stent; its nodes were radially displaced by 2 mm over a 400 ms timeframe. The plastic strains (PEEQ) computed at the end of the expansion procedure were extracted in order to be imported in the subsequent simulation of the stent crimping procedure.

3.4.2 Stent-vein assembly and vein pressurization

The pre-expanded stent was included in a new model and the previously computed plastic strains were assigned to it by means of the * INITIAL CONDITION keyword available in Abaqus/Explicit. The stent was positioned co-axially with the vein, so to encompass the vein and to have its central cross section at the position of the vein valve (**Figure 3.10**).

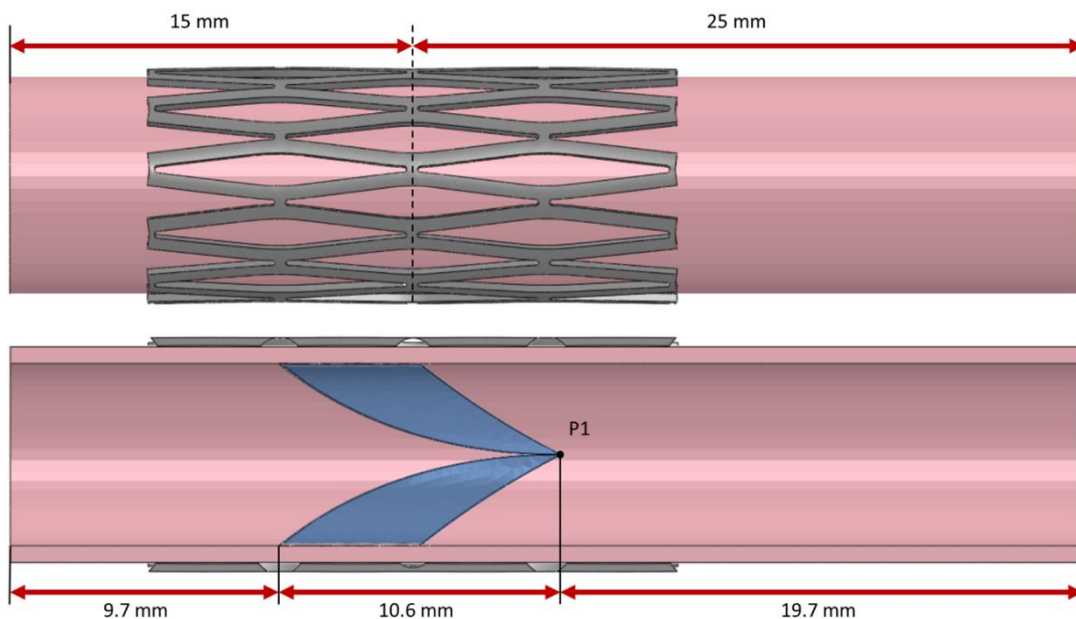


Figure 3.10: Set-up of the surgical procedure simulation: assembly (*top*) and longitudinal section cut (*bottom*). the two leaflets' halves and their conjunction point (P1) are highlighted in the *bottom* panel.

Vein pressurization up 80 mmHg was simulated as described in Section 3.3. In this process, contact between the stent and the vein outer surface was modeled as in the simulation of the pre-stenting function (Section 3.3).

3.4.3 Stent crimping procedures and cardiac cycles simulation

By means of the *RESTART keyword available in Abaqus/Explicit [20], a multi-step restart analysis was run to simulate stent crimping and the subsequent structural mechanics during two consecutive cardiac cycles. The starting point of the restart analysis consisted in final configuration of the stent-vein assembly and vein pressurization; such starting point included all of the associated field and history variables.

An ideal cylinder with an axial length of 40 mm was modelled and placed externally to all the other set-up components, so to be coaxial with the stent and the vein (Figure 3.11.a).

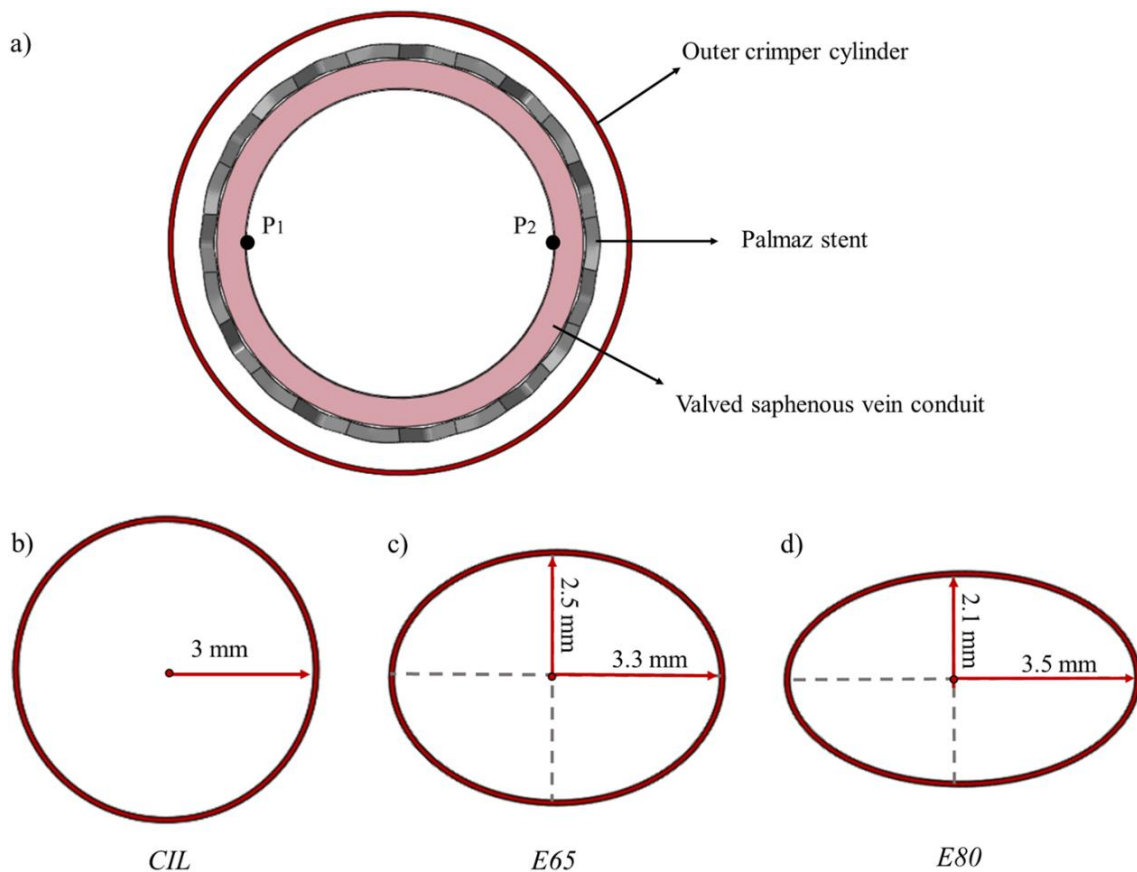


Figure 3.11: Transversal view of the initial set-up configuration of the experiment, with the outer crimper cylinder included (a). Transversal views of the crimper after the different crimping procedures: a perfectly cylindrical crimped form (b) or in an elliptical form of eccentricity 0.65 (c) or 0.80 (d).

The external cylinder was discretized into 4-node shell elements (S4R) with 0.4 mm characteristic dimension. This cylinder was used as a crimper: in the first step of the simulation, it was shrunk by imposing nodal displacements to all of its nodes. Three different crimping modalities were simulated in three different simulations, resulting in different final configurations of the crimper, which were idealized and yet characterized by different degrees or types of distortion (**Figure 3.11.a**).

In modality 1, the final configuration of the crimper was assumed as a cylinder with a perfectly circular cross-section (*CIL*) with a 6 mm diameter (**Figure 3.11.b**). In modality 2, the final configuration of the crimper was assumed as a cylinder with an elliptic cross-section whose perimeter was the same as in modality 1 and whose eccentricity was 0.65 (*E65*) (**Figure 3.11.c**). The major axis of the ellipse was aligned with the commissure-commissure axis of the venous valve. In modality 3, the final elliptic cross-section was modified to increase the eccentricity to 0.8 (*E80*) while still keeping the perimeter unchanged with respect to modality 1 and modality 2 (**Figure 3.11.d**).

To reduce possible oscillations associated to inertial effects, the crimping phase was performed in 2.0 s and it was followed by 0.5 s where the crimper was hold to its final configuration. After the crimping ending, the outer cylinder was removed.

In the subsequent steps, two cardiac cycles were simulated by imposing the same boundary conditions adopted when simulating the behavior of the valved saphenous conduit in the pre-stenting condition (Section 3.3). Contact was modeled as described in Section 3.3 to account for stent-crimper (only during crimping), valve-vein and leaflet-to-leaflet contacts, as well as for leaflet self-contact. Contact between the outer surface of the vein conduit and the inner surface of the stent during the cardiac cycles was modeled using a cohesive behavior surface interaction.

3.5 Post processing

During both the simulation of the un-stented saphenous valved conduit and the simulation of the complete surgical procedure, the geometric configuration of the set-up parts as well as their mechanical behavior were analyzed.

Contour plots of stresses and strains were plotted in Abaqus Viewer to evaluate their patterns in the different geometry components and their changes during the computational test: for

the saphenous conduit, the maximum principal stresses were observed, while the Von Mises Stress and the equivalent plastic strain (PEEQ) were considered for the stent.

Furthermore, in order to compare the different crimping modalities, both the stent's Von Mises stresses and the vein's maximum principal stresses at the end of the crimping phase were examined by computing their boxplots and statistical tests were performed on these data with GraphPad (GraphPad Software, San Diego, CA, USA): data normality was tested through a Kolmogorov-Smirnov test; an Anova or a Kruskal-Wallis test was used to compare data, depending on whether data were normally distributed; a Dunn's multiple comparisons test to examine the groups two by two. Moreover, the Von Mises stresses experienced by the stent during the cardiac cycles were acquired for the three crimped conduits; the respective 90th and 50th percentile over the cardiac cycle were compared.

Moreover, the maximum principal strains obtained at the level of the leaflets' commissures (**Figure 3.12**) when considering the different crimping modalities were compared, computing the time-course of the respective 90th and the 50th percentiles during the second cardiac cycle simulation. This was done on the basis of existing studies [20], regarding cardiac valves, stating that an eccentric distortion of the valve may cause an increase in the maximum principal strain concentration in the commissure regions of the leaflet, which have been shown to be a factor in lowering the durability of prosthetic valves, causing structural failure of the leaflets.

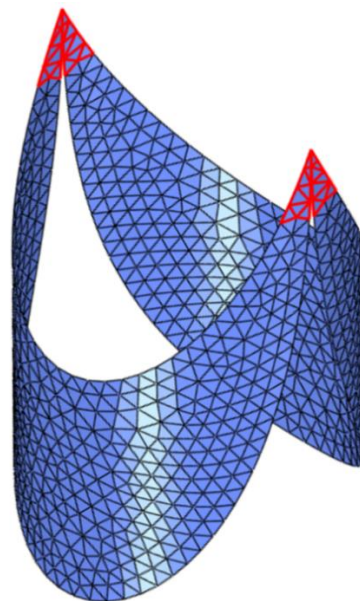


Figure 3.12: Valvular geometry in its undeformed configuration, with highlighted the elements taken into account for the maximum principal strain evaluation at the leaflets' commissures level.

In addition, to evaluate the valve behavior during the cardiac cycle, the time-dependent valve geometric orifice area (GOA) was assessed: GOA is a planimetric measure of the valve cross-section available to fluid flow.

To compute GOA, images of the valve geometry on a plane transversal to the vein axis were acquired, every 0.016 s during the systolic phase of the second cardiac cycle, and then converted into binary images. These images were imported in MATLAB (MathWorks, Natick, MA, USA), where all the boundary edges were detected and saved as matrixes of coordinates. The areas underlying these boundaries were calculated using *polyarea*.

This procedure was carried out both for the non-stented vein and for every crimped venous conduit, to measure the behavior of the valve GOA over time and to compare the different outcomes of the three different crimping, also by means of maximum, 90th and mean GOA values.

Chapter 4

Results and Discussion

4.1 Mesh convergence analysis

4.1.1 Palmaz stent

During the mesh sensitivity analysis, the Palmaz stent was expanded to an inner diameter of 8 mm and then crimped to a 6 mm outer diameter. Between expansion and crimping a spring-back phase took place. The average of the nodes radial coordinates of the whole stent were extracted from the simulation, the percentage radial recoil was calculated. The results are presented in **Table 4.1**.

	Recoil		
	<i>COARSE</i>	<i>MEDIUM</i>	<i>FINE</i>
$De - Dr$ [mm]	4.19 – 4.10	4.19 – 4.08	4.19 – 4.09
Recoil % [-]	2.27	2.59	2.49

Table 4.1: Average radial coordinates of stent nodes after expansion (De) and relaxation (Dr) and values of the resultant percentage radial recoils.

The difference in recoil obtained with the three stent discretizations was not significant: the recoil found varied in a range of 0.02 mm, corresponding to less than 27% and 40% of the radial dimension of the elements in the Coarse and Fine mesh, respectively.

Both at the end of expansion and at the end of crimping, the Von Mises stress (σ_{VM}) distribution highlighted peak values localized at the vertexes of the stent cells, while the lowest stresses were situated in the middle region of the struts (**Figure 4.1**).

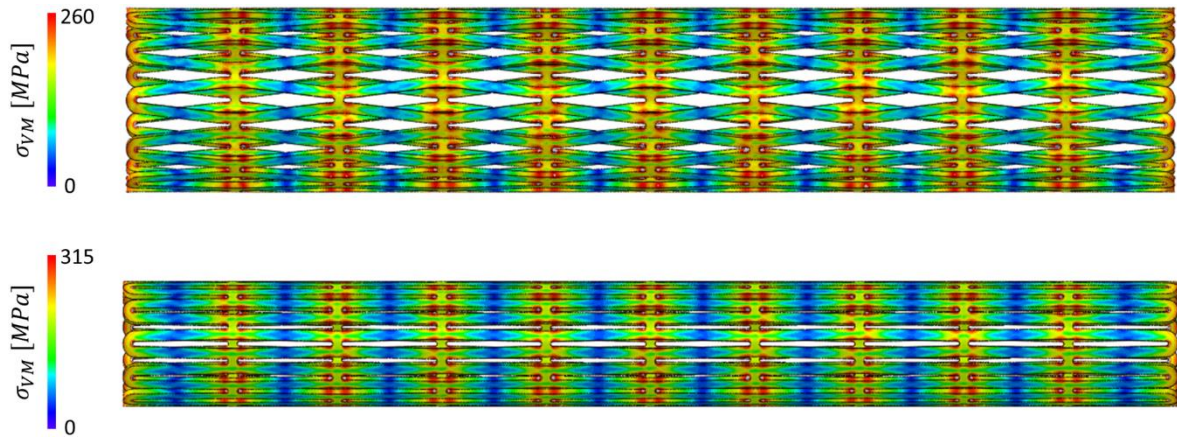


Figure 4.1: Abaqus colour map showing Von Mises stresses in the Coarse stent after the expansion phase (up) and after the crimping phase (down).

At every time-point during the simulation, σ_{VM} peak values were considerably lower than the true ultimate strength σ_{u_true} of the Palmaz stent, which is equal to 824 MPa (**Table 4.2** and **Table 4.3**).

σ_{VM} [MPa]	Expansion Phase		
	<i>COARSE</i>	<i>MEDIUM</i>	<i>FINE</i>
Maximum	358.97	373.42	382.19
90 th percentile	221.06	221.30	224.17
Mean	126.47	127.28	131.54
10 th percentile	33.82	34.19	35.03

Table 4.2: Von Mises stresses obtained in the stent convergence test at the end of the expansion procedure.

σ_{VM} values computed and the end of the stent expansion with the three meshes presented negligible percentage differences: the mean value, the 90th and 10th percentiles of the σ_{VM}

distribution differed by no more than 1.10% between the Coarse and Medium discretizations, and by no more than 3.35% between the Medium and Fine discretizations (**Table 4.2**).

σ_{VM} [MPa]	Crimping Phase		
	<i>COARSE</i>	<i>MEDIUM</i>	<i>FINE</i>
Maximum	433.70	453.17	462.77
90 th percentile	251.92	252.66	252.26
Mean	143.02	144.01	147.66
10 th percentile	40.06	40.50	40.94

Table 4.3: Von Mises stresses obtained in the stent convergence test after crimping ending.

Similarly, σ_{VM} values computed and the end of the stent crimping with the three meshes showed negligible percentage differences: the mean value, the 90th and 10th percentiles of the σ_{VM} distribution differed by no more than 1.08% between the Coarse and Medium discretizations, and by no more than 2.53% between the Medium and Fine discretizations (**Table 4.3**).

Using the extracted stress quantities, the portion of stent elements ($\%E_y$) experiencing a σ_{VM} higher than the yielding value was computed (**Table 4.4**). This $\%E_y$ values showed a similar expansion-crimping behavior for the three meshes, with a percentage difference within 1.6% and 4.8%, respectively, between Coarse and Medium meshes and between Medium and Fine discretizations.

	Percentage of elements above the yield stress $\%E_y$ [-]		
	<i>COARSE</i>	<i>MEDIUM</i>	<i>FINE</i>
Expansion	19.63	19.67	22.07
Crimping	39.56	40.19	42.12

Table 4.4: Table of percentage number of elements enduring a Von Mises stress higher than the Yielding stress, after the expansion phase and after the crimping phase.

To better evaluate the plasticization of the Palmaz stent during the computational test, the equivalent plastic strains (PEEQ) of the stent were analyzed: PEEQ values showed a similar expansion-crimping behavior for the three meshes, with a percentage difference within 1.6%

and 4.8%, respectively, between Coarse and Medium meshes and between Medium and Fine discretizations. Similarly to σ_{VM} , peak PEEQ values were computed at the strut junctions, while the elements in the middle of the struts were not plasticized neither by the expansion nor by the stent crimping (**Figure 4.2**).

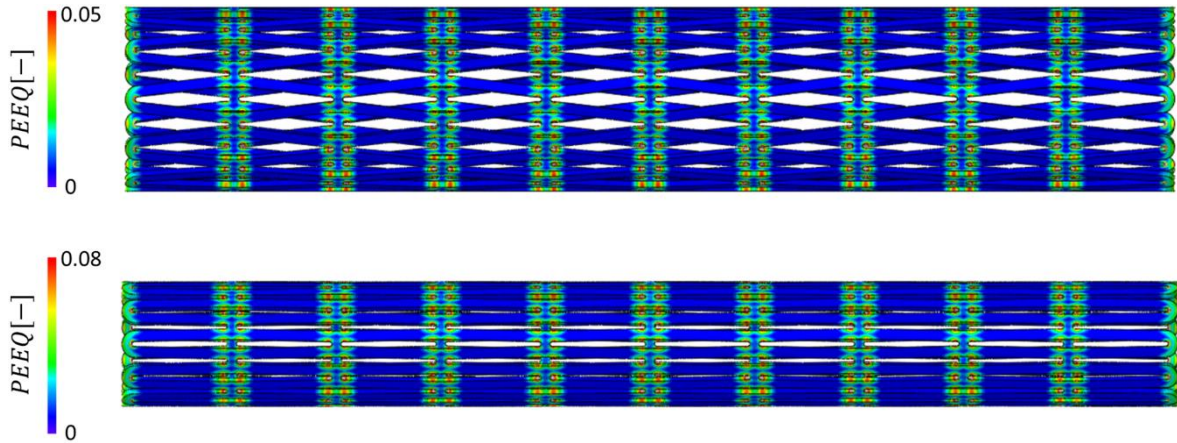


Figure 4.2: Abaqus contour plot of the equivalent plastic strains (PEEQ) in the Coarse Palmaz stent after the expansion phase (up) and after the crimping phase (down).

The percentage of plasticized elements ($\%Ep$) was computed by identifying the portion of elements with a $PEEQ > 0$ above the total stent element number (**Table 4.5**).

	Percentage of elements plasticized $\%Ep$ [-]		
	<i>COARSE</i>	<i>MEDIUM</i>	<i>FINE</i>
Expansion	38.35	38.56	40.50
Crimping	47.15	47.27	50.29

Table 4.5: Table of percentage number of elements with an equivalent plastic strain $PEEQ > 0$, after the expansion phase and after the crimping phase.

At the end of the simulated crimping, $\%Ep$ was markedly larger than at the end of the simulated expansion; this trend was observed for each mesh. The difference in $\%Ep$ was within 0.54% between the Coarse and Medium meshes, and within 6.39% between the Medium and Fine meshes.

The computational tests with the three stent meshes were performed using the same computational resources, i.e., 12 CPUs with 32 GB RAM. The comparison of the corresponding simulation time is reported in **Table 4.6**. The computational cost of the

simulation underwent significant changes based on the considered mesh: passing from the Coarse to the Medium mesh, the computational cost increased by more than 50%, while from the Coarse to the Fine discretization the simulation almost doubled its time length.

	Computational cost		
	<i>COARSE</i>	<i>MEDIUM</i>	<i>FINE</i>
Simulation Time [h: min]	85: 35	135: 33	176: 29

Table 4.6: Comparison between the different simulation times required with the three meshes.

Based on the results herein reported, the *Coarse* mesh was chosen to model the Palmaz stent in the subsequent simulations, because it proved more time-efficient at the expense of a minor loss in results accuracy.

4.1.2 Saphenous vein

In the saphenous sensitivity analysis, the dependence of the stress-strain behavior of the venous conduit from the mesh refining level was investigated. The time-course of the normal components of the stress and strain tensors in the circumferential, axial and radial directions were extracted and averaged over the ROI elements. Hence, the stress-strain curves in the three directions were obtained (**Figure 4.3**).

In this computational inflation-extension test, the effect of the radial load resulting from the intraluminal pressure prevailed on the axial load: the vein underwent negative axial and radial strains and a positive circumferential strain, as a result, the conduit was shortened and the wall thickness was thinned, instead the saphenous vein circumference increase.

The axial strain was one order of magnitude smaller, in magnitude, than the circumferential and radial strains. Conversely, the stresses reached higher values in axial and circumferential directions, while in the radial direction they were one order of magnitude lower in magnitude (**Figure 4.3**).

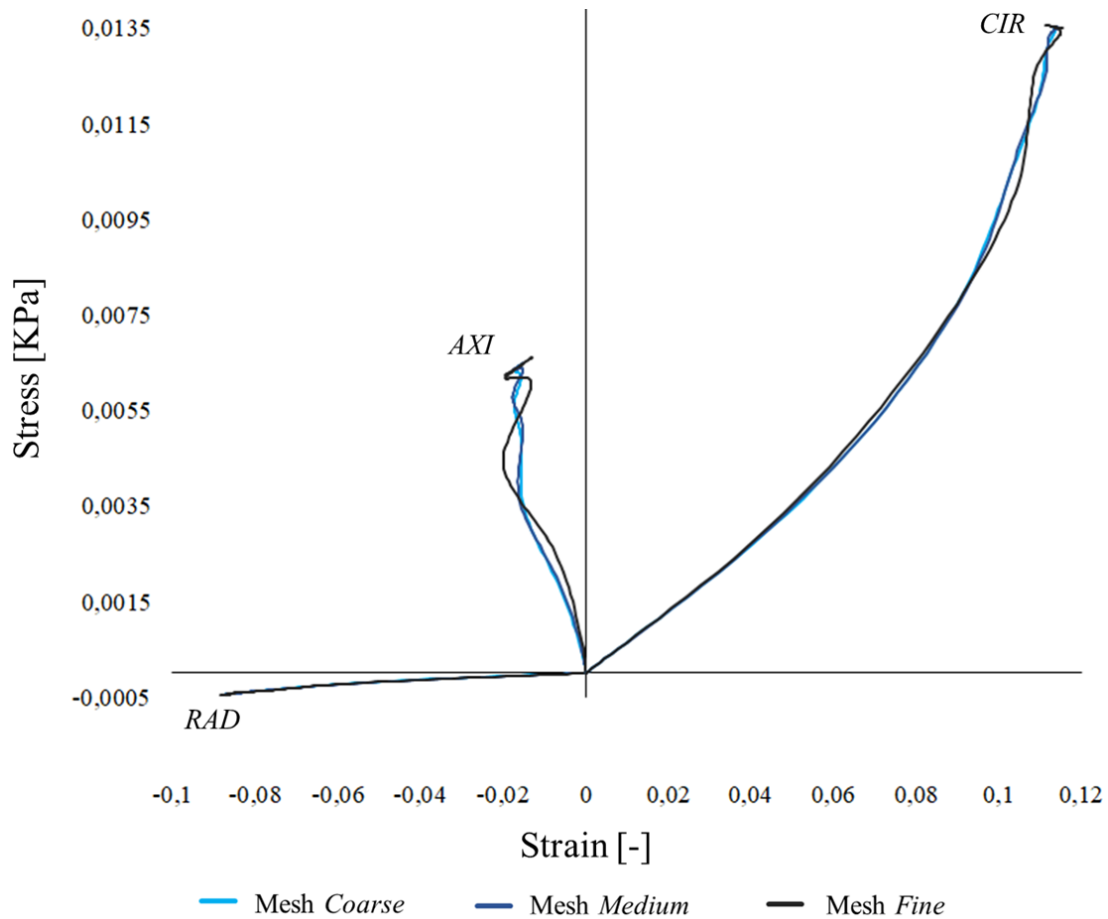


Figure 4.3: Comparison of the stress-strain behavior of the saphenous ROI elements within the different vein discretizations in circumferential (*CIR*), axial (*AXI*) and radial (*RAD*) directions.

The stress-strain curves did not change significantly when considering different mesh refinement levels. However, the more the discretization was refined, the more the inertial effects were relevant, causing an increasing oscillation of the solution. This inertial behavior was due entirely to the use of a fixed mass scaling when exploiting the explicit time-integration scheme: the smaller the elements, the higher the fictitious increase in density associated to the elements so to obtain a given stable time increment. Indeed, when simulating the same test using Abaqus/Standard, i.e., the implicit time-integration scheme, these oscillations were absent.

The sensitivity analysis of the saphenous vein model was performed using identical computational resources for the simulation of the three meshes. The tests were completed using the same 10 CPUs with 32 GB RAM; the computational costs are reported in **Table 4.7**. Of note, from the Coarse to the Fine mesh the time needed for the inflation-extension test increased by more than 27 times.

	Computational cost		
	<i>COARSE</i>	<i>MEDIUM</i>	<i>FINE</i>
Simulation Time [h: min]	0: 45	3: 15	20: 36
Δt % [-]	-	333.33	531.08

Table 4.7: Comparison between the different simulation times required with the three vein meshes.

Another crucial factor for the selection of the most suitable mesh was that the saphenous vein conduit was designed with the aim of interacting with the other components requested for the subsequent surgery simulation: at the inner surface of its conduit with the attached venous leaflets, while on the venous outer surface with the external Palmaz stent. Therefore, it was mandatory to choose a venous discretization appropriate to interact with both these other entities of the tested procedure [9]. To this purpose, sufficiently smooth inner and outer surfaces of the saphenous vein conduit were requested (**Figure 4.4**).

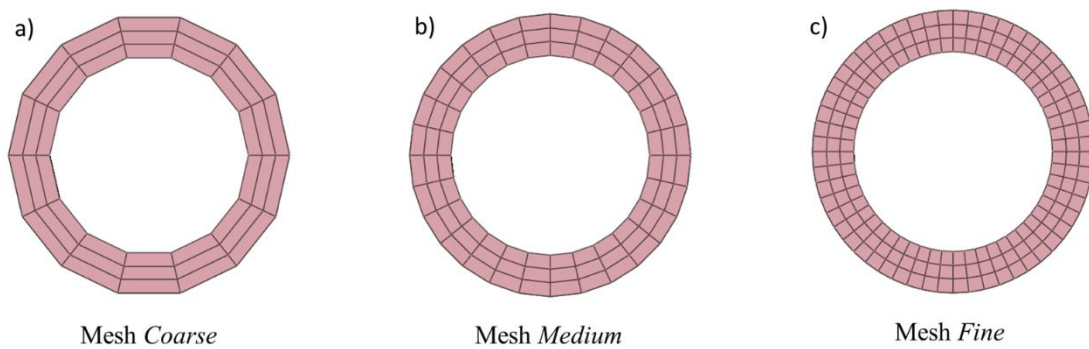


Figure 4.4: Transversal view of the three saphenous vein meshes tested.

Based on these considerations, although the Coarse mesh allowed to obtain highly convenient simulation times, it was judged inadequate to provide a smooth inner surface to be connected to the leaflets attachment line through the tie constraint, as well as a smooth outer surface interacting with the stent through contact (**Figure 4.4.a**) [9].

On the contrary, the Fine mesh offered a smooth cylindrical geometry (**Figure 4.4.c**), which was considered suitable to model the interaction with both the venous leaflets and the stent, however, this discretization required an excessive computational cost.

Hence, the Medium mesh was identified as a suitable trade-off between acceptable simulation times and an adequate rendering of the vein wall geometry, and it was chosen for

the modelling of the saphenous vein in the subsequent simulation of the complete surgical procedure [9] (**Figure 4.4.b**).

The circumferential and axial stretches obtained from the simulation run on the Medium mesh were correlated to the pressure applied in the Abaqus test. The resulting curves were filtered using MATLAB to remove the inertial effect, and then compared vs. the behavior of the saphenous vein samples presented in Vesely et al. work [15] (**Figure 4.5, Figure 4.6**).

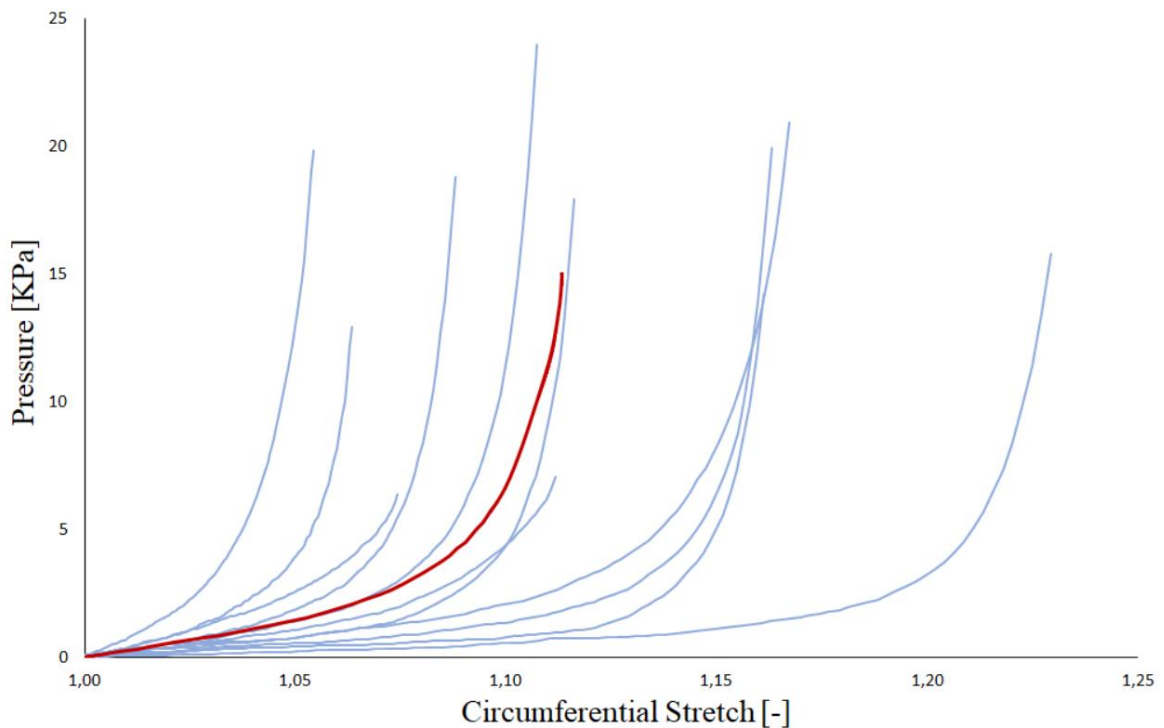


Figure 4.5: Pressure-circumferential stretch curves obtained from the fitting of experimental data with Holzapfel constitutive model (blue), taken from the reference paper [15], and the pressure-circumferential stretch behavior resulting from the inflation-extension computational test performed in this thesis work (red).

The pressure over circumferential stretch ratios behavior perfectly fit within the range of physiological curves acquired from the experimentally tested veins reported in Vesely et al. study [15] (**Figure 4.5**).

The pressure over axial stretch ratios provided by the computational inflation-extension test was comparable to the ones obtained from experimental data fitting [15] (**Figure 4.6**). In this graph, the interval in axial stretch from 0.99 to 1.01 identified by gray lines represents bounds of uncertainty caused by resolution of digital cameras used in the reference experimental test [15]. Because of this uncertainty, as well as because of the notably small

strains, results reported in [15] concerning pressure-axial stretch ratios curves were not considered fully reliable and the obtained level of agreement was considered satisfactory.

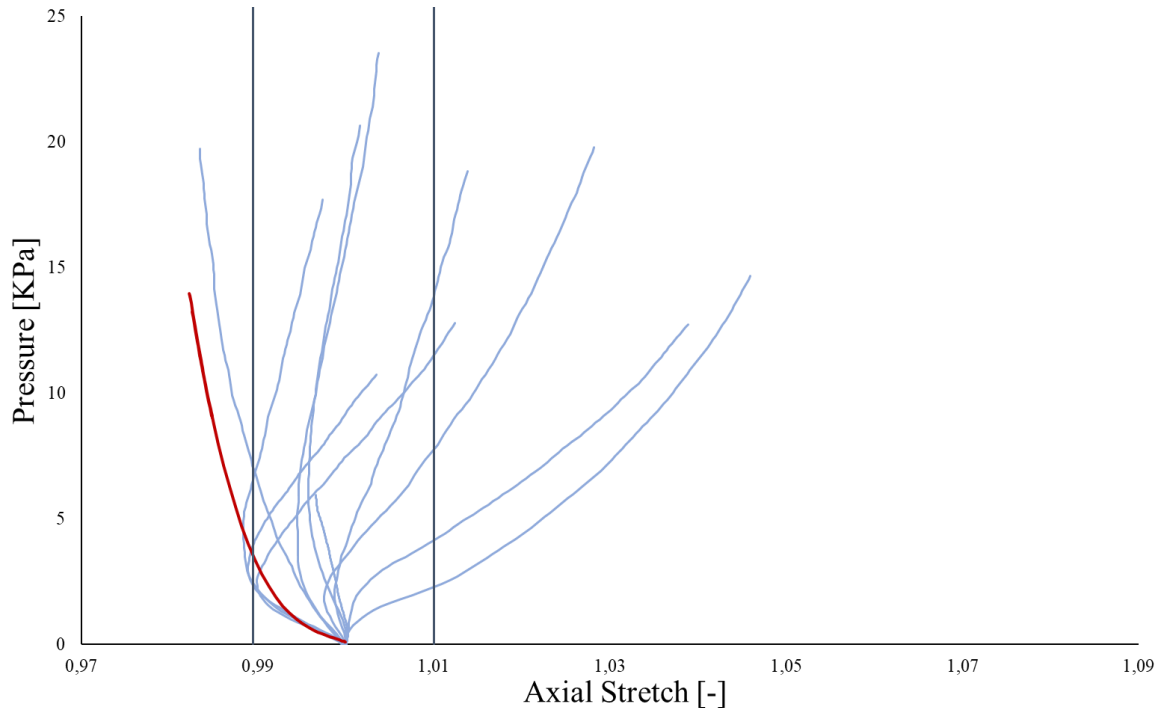


Figure 4.6: Pressure-axial stretch curves obtained from the fitting of experimental data with Holzapfel constitutive model (blue), taken from the reference paper [15], and the pressure-circumferential stretch behavior resulting from the inflation-extension computational test performed in this thesis work (red).

The pressure behavior over circumferential and axial stretch ratios of the computational inflation-extension test were assessed to be consistent with the curves presented by Vesely et al. [15], therefore the numerical model of the vein was considered an adequate representation of a possible physiological behavior of the saphenous conduit.

In the application considered in this thesis work [9], the selection of a specific patient sample pre-operatively is not practicable, because of both the tight deadlines for the surgery execution for a patient suffering from HLHS and the great physiological variability of the vein properties, which can be seen by the wide ranges of the parameters for the saphenous modelling obtained in the reference work [15]. Therefore, the plausible behavior of the modelled saphenous vein conduit was considered sufficient for an appropriate simulation of the vein response to the reinforced RVPA shunt implantation procedure performed subsequently to the sensitivity analysis of all the components involved in the surgery.

4.1.3 Venous valve leaflets

Valve leaflet dynamics and leaflet maximum principal stresses (σ_I) were verified in all the considered meshes. The time-course of σ_I during the cardiac cycle was assessed simulation based on contour plots and the values of stress over time were extracted (**Figure 4.7**).

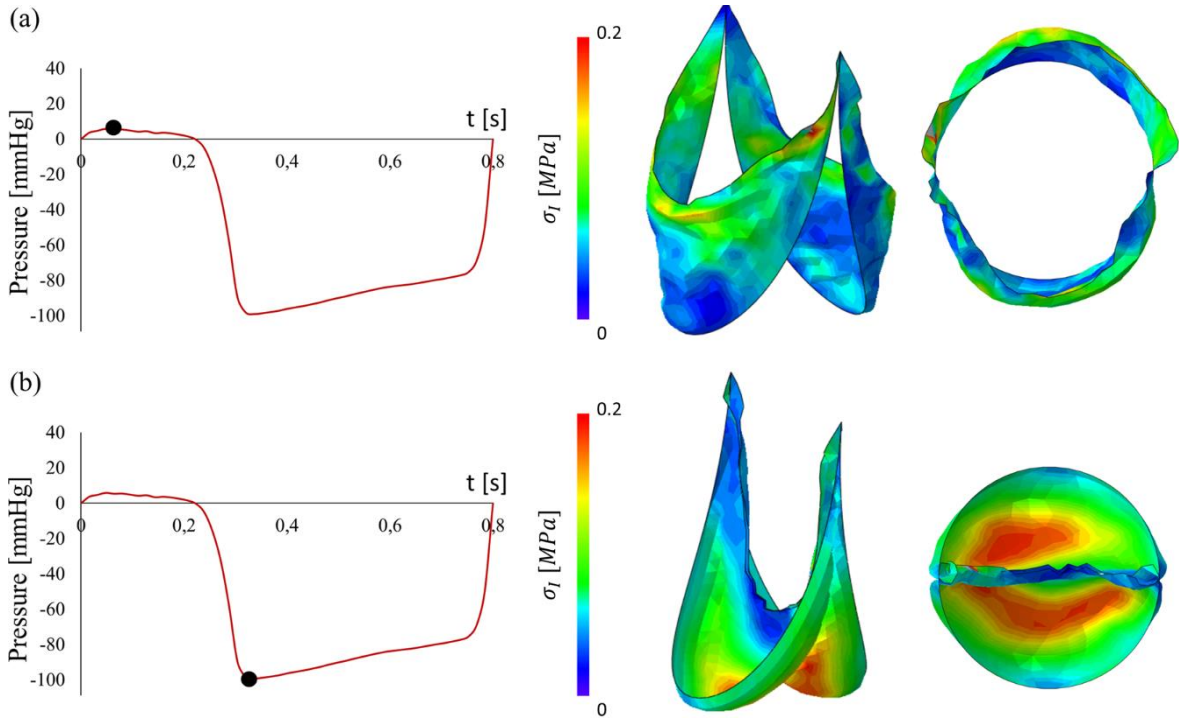


Figure 4.7: Geometrical configuration and σ_I contour plot, in the valve with Mesh 0.4, during the second cardiac cycle, respectively, at the instant of maximum opening ($t = 0.064$ s) and at the diastolic pressure pick ($t = 0.32$ s).

For every mesh refinement level, the stresses reached considerably higher values during ventricular diastole, while the valve was in its closed configuration, and it presented lower values during the valve opening in systole.

The time-course of σ_I 10th, 50th and 90th percentiles was computed (**Figure 4.8**). The finer the mesh, the more deformable the leaflet response to pressure and the more inertial effects became noticeable, leading to numerical artefacts in the σ_I behavior. This last effect was particularly visible in the most refined mesh, which underwent a sudden spike in the maximum principal stress after valve closure, followed by settling fluctuations of stress values.

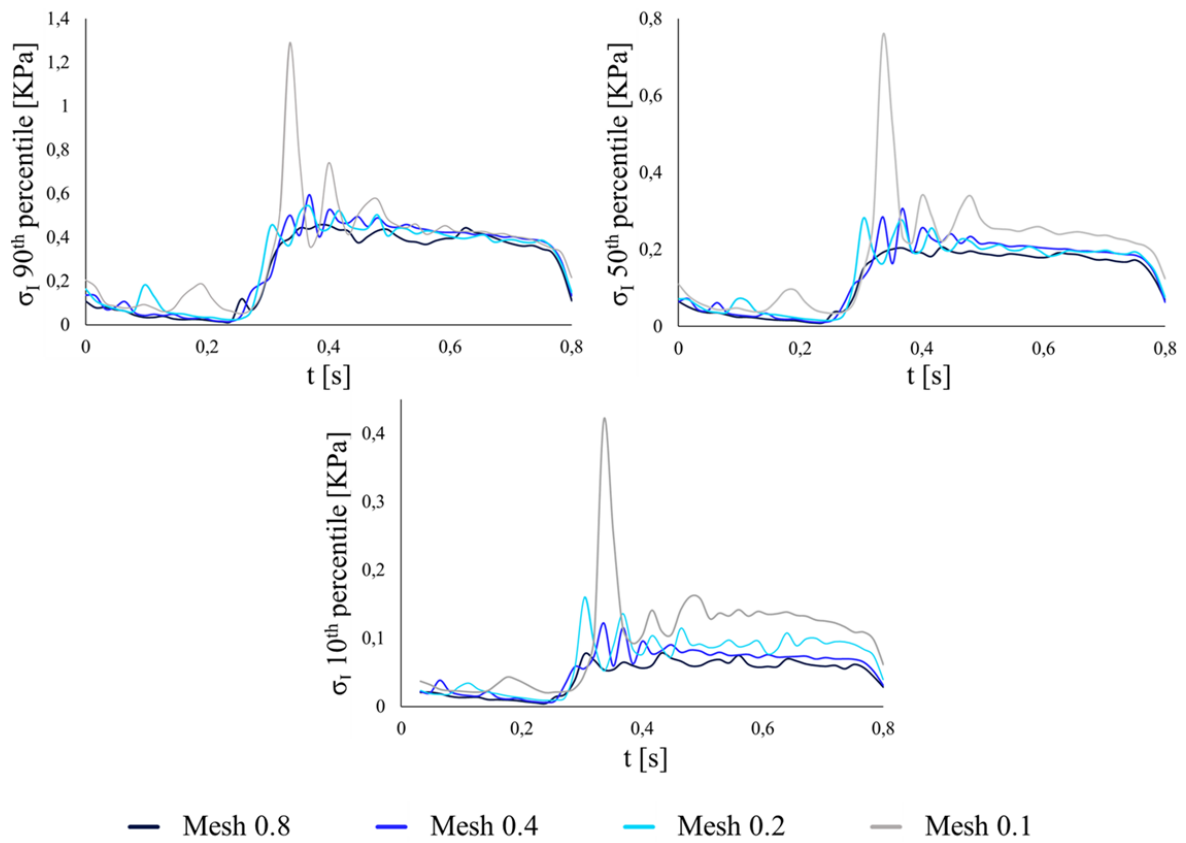


Figure 4.8: Comparison of the behaviors of maximum principal stresses 10th, 50th and 90th percentiles, obtained using the four valve meshes.

The same fluctuations could be seen, to a lesser extent, also during the first part of the cardiac cycle, corresponding to systole, and in the other meshes: the coarsest discretization, *Mesh 0.8*, was the one in which this behavior was least pronounced.

This oscillatory behavior of the stresses, likely caused by the inertial effects on leaflet motion, was due to the use of the Abaqus/Explicit solver. The same valve inertia had effects upon the valve leaflets opening and closure dynamics: the more the mesh was refined, the more the leaflets were fluttering. This can be noticed by the analysis of the time-course of the displacement magnitude, U , of the nodes closest to the valve leaflets belly centers, in the different discretizations (**Figure 4.9**).

In particular, in the most refined mesh the valve inertia reached such an extent that the valve dynamics was delayed with respect to the other discretizations. Moreover, shortly after the valve opening the leaflets oscillated and then reopened; the same oscillation was observed at leaflets closure. The fluctuating behavior was found, on a smaller scale, also in *Mesh 0.2* and it was even lower in *Mesh 0.4* and *Mesh 0.8*.

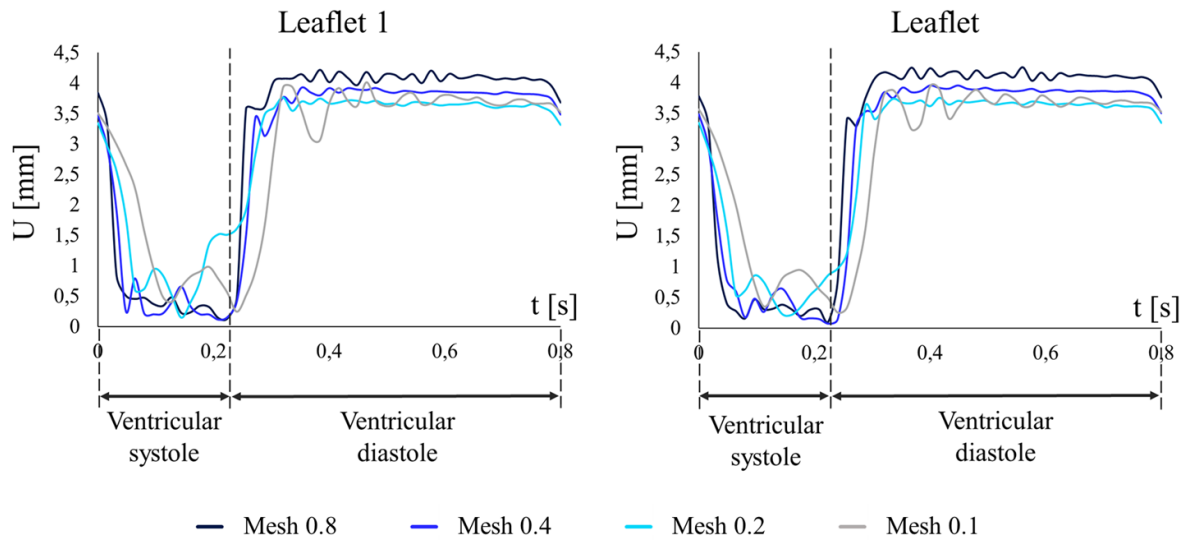


Figure 4.9: Displacement of nearest node to the leaflet belly center noticed that, since the valve was modelled in the opening configuration, displacement equal to zero corresponds to a return in the initial position.

These simulations were performed with the same computational resources (i.e., 8 CPUs with 8 GB RAM) and their time-expense varied highly among the different mesh refinement levels (**Table 4.8**)

	Computational cost			
	Mesh 0.8 mm	Mesh 0.4 mm	Mesh 0.2 mm	Mesh 0.1 mm
Simulation Time [h: min]	0: 13	0: 33	1: 44	5: 52
Δt % [-]	-	153.85	215.15	238.46

Table 4.8: comparison between the different simulation times required with the four valve meshes.

The last aspect that was taken into account for the valve sensitivity analysis was the geometrical configuration resulting from the simulations. In the subsequent tests, the valve would have to interact with the internal lumen of the saphenous conduit, in view of this, it was necessary an element dimension suitable to properly tie the valve basal margin to the vein internal surface.

Consequently, although the *Mesh 0.8* provided highly convenient simulation times and sufficiently smooth stresses behavior and dynamics, it was considered too coarse both to represent correctly the valve geometry and to provide a fair attachment to the vein. On the contrary, the *Mesh 0.1* presented the finest discretization and it was considered suitable for the interaction with the vein lumen, however, its stresses and displacement behaviors were

overly affected by the inertia of the leaflets and the computational cost demanded was considered excessive. The behaviors provided by *Mesh 0.2* and *Mesh 0.4* were almost comparable: the first offered a better discretized geometry, but it was affected by both a higher inertial behavior and a greater computational cost; the second, instead, provided a sufficiently stable valve dynamics, favorable simulation length and a characteristic element dimension suitable to interact with the inner surface of the chosen saphenous vein, whose element surfaces on the lumen of the conduit had the same dimension (i.e., 0.4 mm). Based on these considerations, *Mesh 0.4* was chosen as the best compromise for the valve discretization.

4.2 Simulation of the surgical procedure

4.2.1 Stent pre-expansion

The reduced geometry of the Palmaz stent used in the simulation of the surgical procedure was pre-expanded up to an 8 mm internal diameter: the new coordinates of the stent nodes were extracted (**Figure 4.10**).

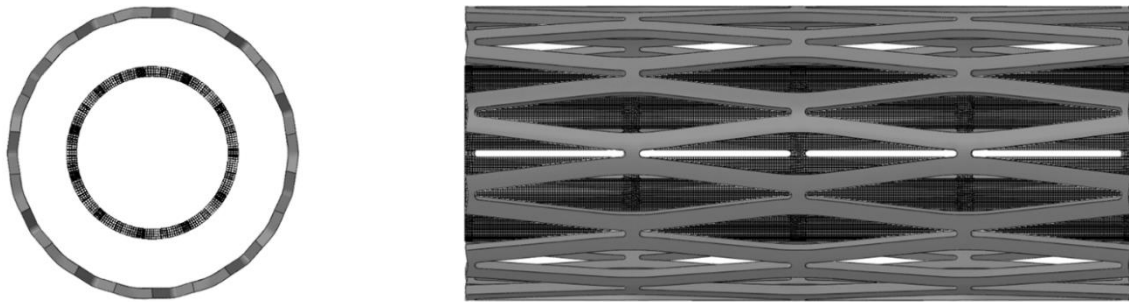


Figure 4.10: Comparison between the Palmaz stent geometrical conformation before and after the expansion: transversal view (left) and axial view (right).

Furthermore, the PEEQ values of the stent elements in their integration points were acquired at the end of the simulated expansion (**Figure 4.11**).

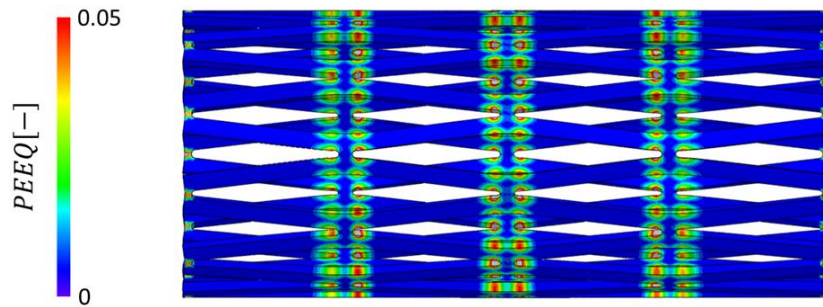


Figure 4.11: Palmaz stent equivalent plastic strain (PEEQ) contour plot after expansion, in Abaqus.

4.2.2 Stent-vein assembly and vein pressurization

Both these data were required to assemble the valved saphenous vein conduit reinforced with the Palmaz stent for the subsequent surgical procedure simulation: the expanded coordinates were used to establish the stent initial geometrical configuration in the surgery, while the PEEQ values were imported as initial condition to take into account the plastic deformation sustained by the stent in the previous expansion procedure.

In the resulting assembly, the inner surface of the saphenous conduit was pressurized to 80 mmHg, leading to the adhesion of the stent to the vein (**Figure 4.12**). This configuration was the starting point of all the three crimping simulations.

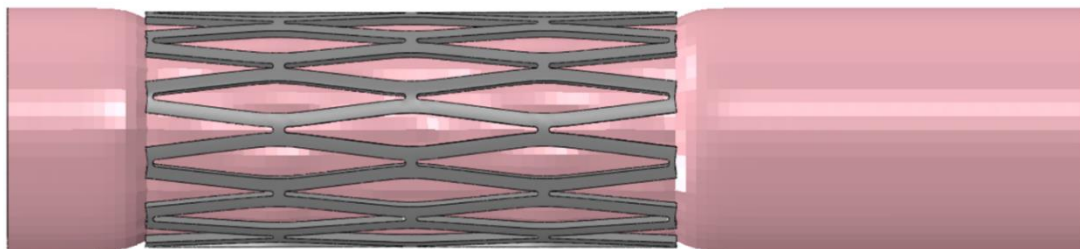


Figure 4.12: Configuration of the reinforced venous conduit after the preparatory pressurization of the saphenous vein.

4.2.3 Stent crimping and post-crimping biomechanics during the cardiac cycle

Stresses on the vein wall after crimping - A qualitative analysis of the three post-crimping configurations of the venous conduit highlighted an increasing corrugation of the crimped portion of the saphenous vein conduit as progressively more eccentric shapes were imposed to the crimped cross-section of the stent, i.e., when shifting from the perfectly circular

crimped stent (*CIL*) to the elliptical one with a 0.65 eccentricity (*E65*) and to the elliptical one with a 0.80 eccentricity (*E80*).

Moreover, Abaqus contour plots varied, based on the crimping modality used (**Figure 4.13**). From the cylindrical crimping to the most elliptical one, a progressive increase in the range of maximum principal stresses σ_I was detected. High stress regions were identified close to the ends of the venous conduit, and progressively higher values were computed ($\sigma_{I_Max}^{CIL} = 0.14$ MPa, $\sigma_{I_Max}^{E65} = 0.24$ MPa, $\sigma_{I_Max}^{E80} = 0.28$ MPa). Conversely, in the crimped part of the conduit, stresses were progressively lower.

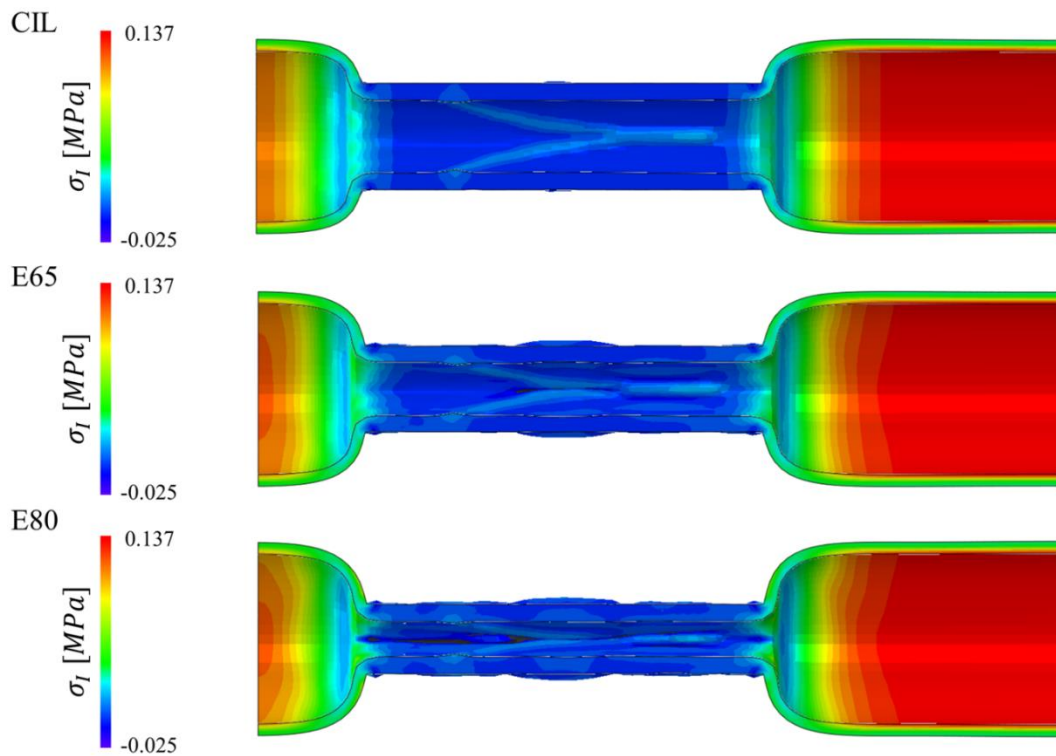


Figure 4.13: Abaqus color map of the venous conduit, axially cut, showing the σ_I pattern after crimping with the three evaluated modalities: *CIL*, *E65* and *E80*.

This observation was corroborated by the computation of the σ_I boxplots (**Figure 4.14**), and it was judged consistent with the increase in the maximum traction acting on the vein extremities and with the increase in the maximum radial compression imposed to the crimped portion of the venous conduit.

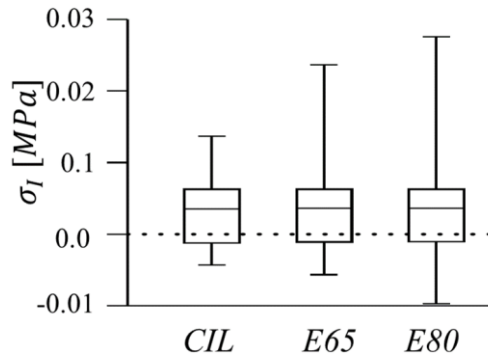


Figure 4.14: Boxplots of σ_l behavior in the saphenous vein depending on the crimping modality applied.

The difference in the stresses obtained in the three crimped configurations was evaluated statistically: after a Kolmogorov-Smirnov test that established the non-normality of σ_l values, a Kruskal-Wallis test was performed and it highlighted a highly statistically significant difference among the three data groups (p-value < 0.0001). In particular, with a Dunn's multiple comparisons test a highly statistically significant difference was found between the data from *CIL* and *E65* (p-value < 0.0001) and between the data from *CIL* and *E80* (p-value = 0.0001). Differences between data from *E65* and *E80* were not statistically significant (p-value > 0.9999).

Therefore, it was assessed that a non-ideal cylindrical crimping modality may overstress the saphenous conduit, however, a lower or higher deviation of the defective crimping final configuration to the ideal one may not change the resulting stress pattern of the saphenous vein conduit.

Stresses and plastic strains on the stent after crimping - A similar analysis was performed on the Von Mises stresses σ_{VM} , computed on the stent. The σ_{VM} contour plots were different in the three crimped configurations (**Figure 4.15**).

A more quantitative description of the σ_{VM} behavior was provided by the boxplots displayed in **Figure 4.16**. Increasing the eccentricity of the stent crimped cross-section led to increase the values of the stress percentiles: in particular, the 50th percentile increased from 126.08 MPa in the *CIL* configuration to 132.42 MPa in the *E65* configuration and up to 160.10 MPa in the *E80* configuration. The maximum σ_{VM} value increased from 526.66 (*CIL*), to 550.87 (*E65*) and to 574.74 (*E80*).

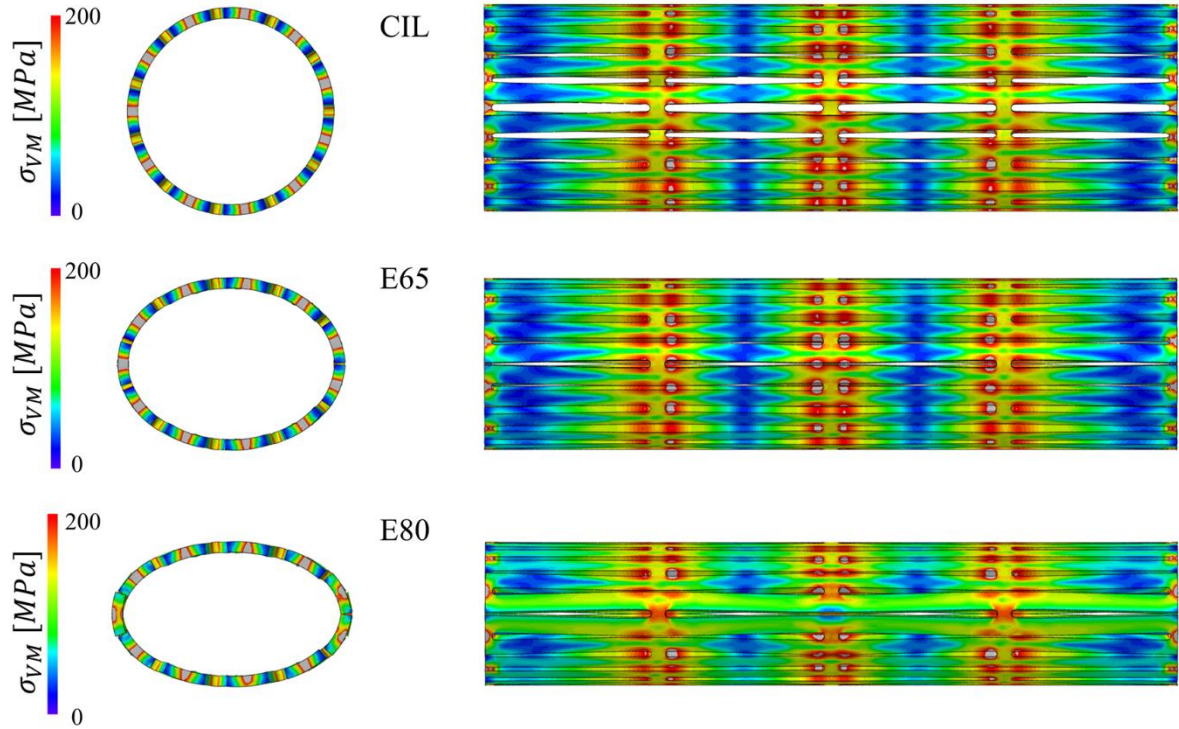


Figure 4.15: Abaqus color map showing σ_{VM} of the Palmaz stent after crimping with the different modalities: *CIL*, *E65* and *E80*.

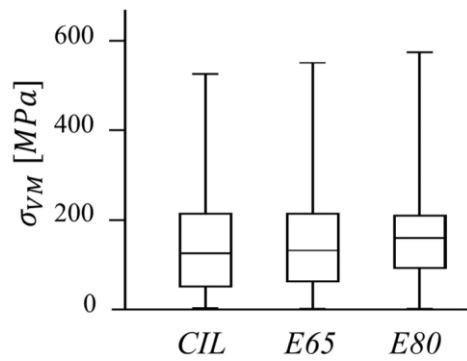


Figure 4.16: Boxplots of σ_{VM} behaviour in the stent depending on the crimping modality applied.

A Kolmogorov-Smirnov test highlighted the non-normality σ_{VM} values. Hence, a Kruskal-Wallis test was performed, and it highlighted a highly statistically significant difference among the three data groups (p-value < 0.0001). Moreover, the Dunn's multiple comparisons test proved the statistical difference when comparing data two by two: *CIL* and *E65* (p-value < 0.0001); *CIL* and *E80* (p-value < 0.0001); *E65* and *E80* (p-value < 0.0001).

In conclusion, it can be stated that the execution of a defective crimping procedure may lead to an actual variation of the stress distribution in the Palmaz stent, causing an overstressing with respect to the ideally cylindrical procedure.

In addition, the percentage of the plasticized elements after the crimping phase was computed. It was found that an increase in the eccentricity of the stent crimped cross-section resulted in a progressively higher number of yielded elements (**Table 4.9**).

Percentage of elements plasticized %Ep [-]		
<i>CIL</i>	<i>E65</i>	<i>E80</i>
37.89	38.63	42.02

Table 4.9: Table of percentage number of elements with an equivalent plastic strain PEEQ >0, after the crimping phase.

In all cases the PEEQs reached their maximum at the strut junctions, while the elements in the middle of the struts did not undergo yielding; however, the plastic strain distribution was different due to the applied crimping modality (**Figure 4.17**).

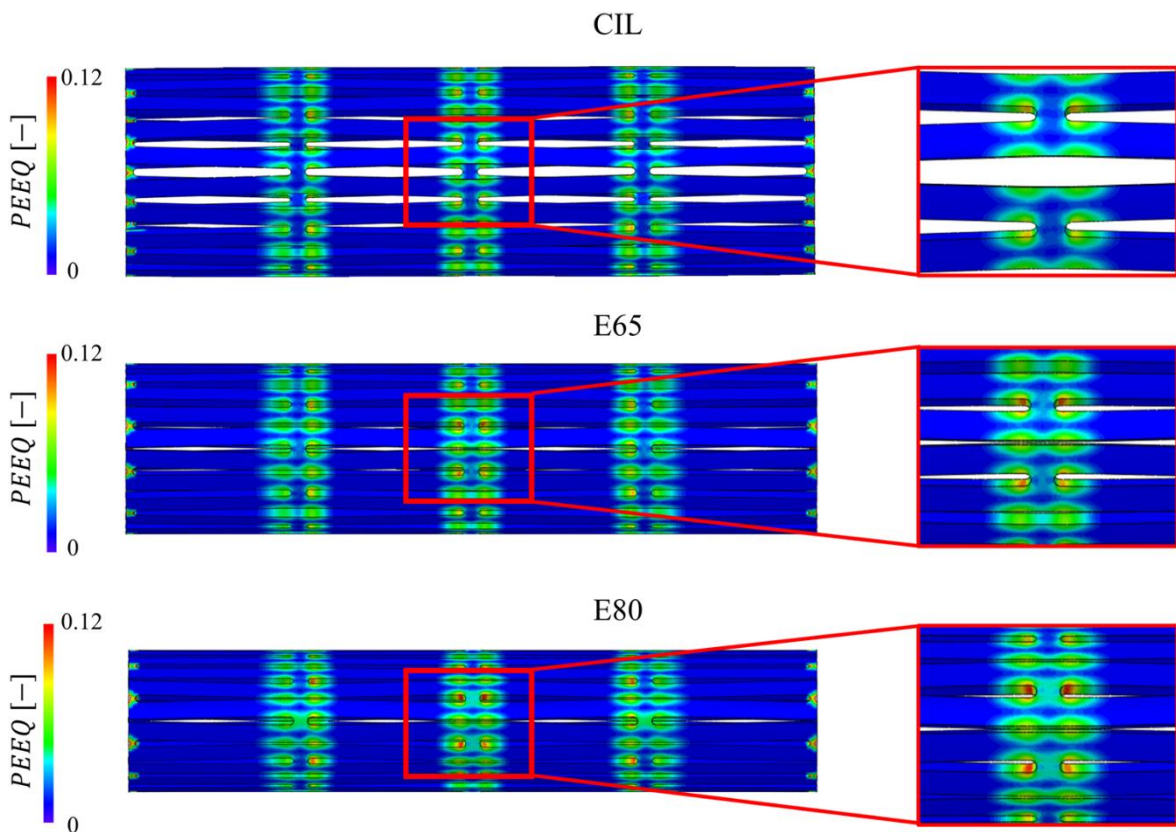


Figure 4.17: Abaqus contour plots of the equivalent plastic strain (PEEQ) of the Palmaz stent after the different crimping (*CIL*, *E65*, *E80*) and close-up views of PEEQ distribution in the region of maximal struts' compression.

In particular, in the *CIL* case a uniform distribution of the PEEQ was obtained among all the struct junctions; while in elliptical crimping a higher plasticization was obtained in the region of maximum struts “squeezing”, due to the final configuration imposed by the virtual crimper. This effect, already observable in *E65*, was even more noticeable in *E80* (**Figure 4.17.close-up views**).

Post-crimping stent stresses during the cardiac cycle - After the crimping phase and a first settling cardiac cycle, the σ_{VM} of the Palmaz stent were reevaluated: their maximum, 90th and 50th percentiles behavior over time is represented in **Figure 4.18**.

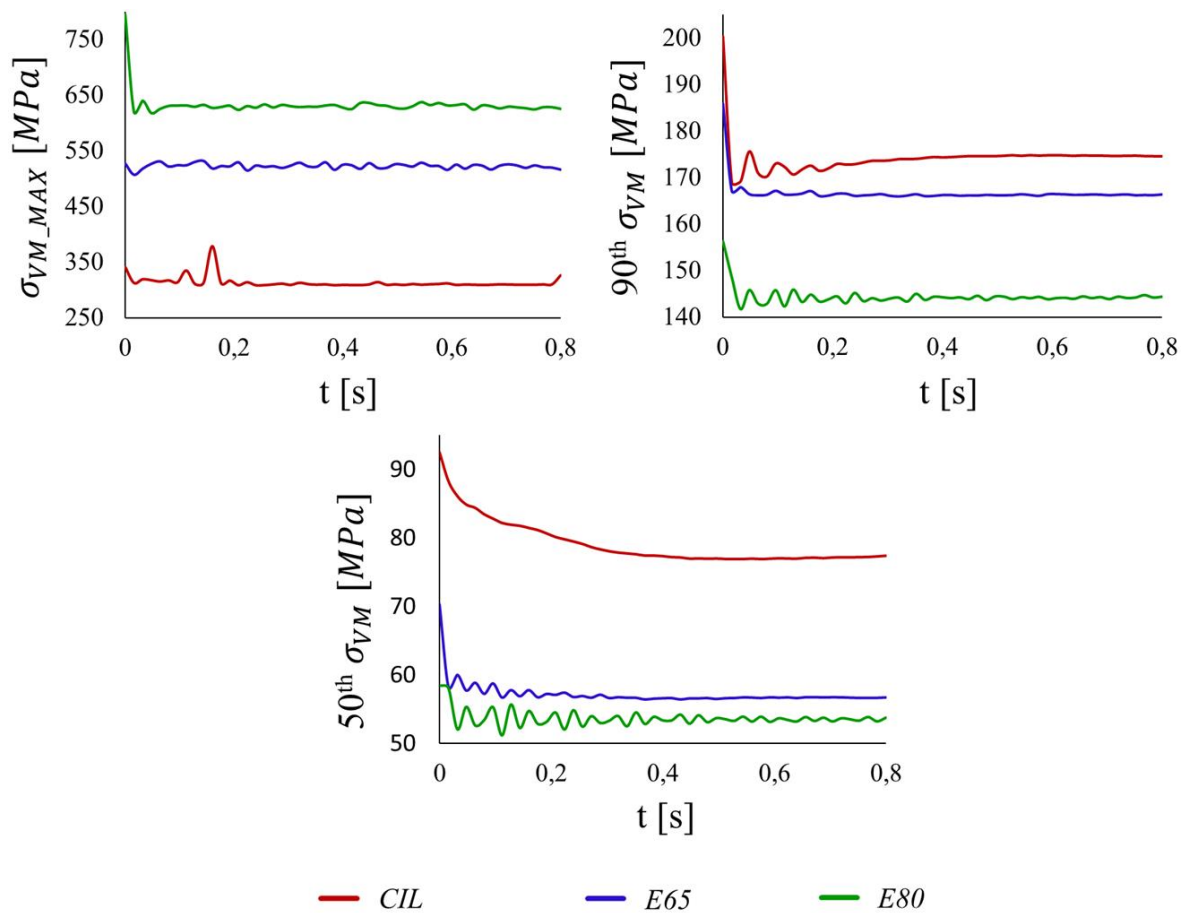


Figure 4.18: Comparison of the behaviors of maximum, 90th and 50th percentiles σ_{VM} during the second cardiac cycle, due to the different crimping modalities used.

A significant increase in the maximum stresses was detected, from CIL to E80 the σ_{VM_MAX} was almost doubled; however, the 90th and 50th percentiles exhibited an opposite trend. This behavior was the result of two different effects: on one side, in the circular crimping the stresses were almost uniformly distributed on the struts in the same axial position, while

in the elliptical crimping they were more concentrated in the region of maximum compression of the stent struts; on the other side, the elliptically crimped stents experienced a higher rearrangement of the stress distribution in the stent, particularly in the region of the maximum compression, due to the higher yielding in the more loaded regions.

Post-crimping valve leaflet strains during the cardiac cycle - During the second cardiac cycle, also the maximum principal strains developed at the commissures levels in the valve were extracted and their 90th and 50th percentile behaviors were plotted over time (**Figure 4.19**).

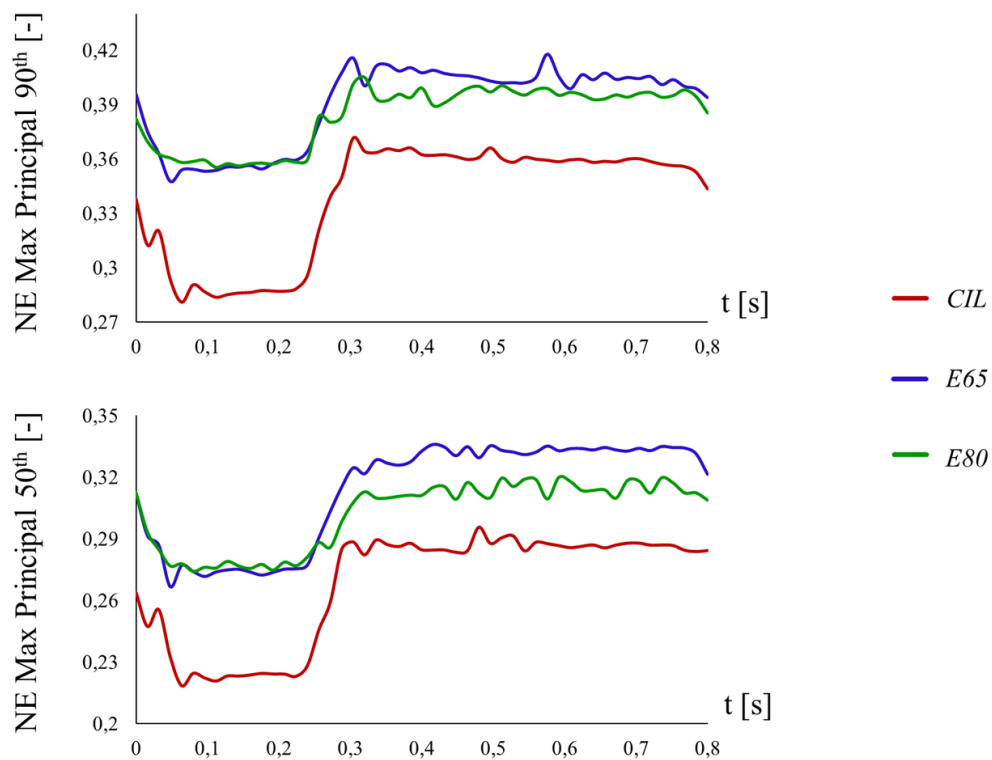


Figure 4.19: Comparison of the behaviors of maximum principal strains 90th and 50th percentiles during the second cardiac cycle, due to the different crimping modalities used.

Generally, the leaflets commissures underwent lower deformations during the opening phase and higher ones during valve closure time. When the conduit was crimped in an elliptical way the strains at the commissure increased: in particular, it was slightly higher in the *E65* case with respect to the *E80* one. The mean over the cardiac cycle of the percentage differences in the 90th and the 50th percentiles between the various crimped configurations was computed: from *CIL* to *E80* the 90th percentile increased of 14.11% on average, while

the 50th of 13.57%; an additional rise of 2.04% in the 90th and of a 13.57% in the 50th was registered from *E80* to *E65*.

The difference in the deformation level could potentially accelerate the deterioration of the valve leaflets and lower their long-term durability. However, although it was noticeable that the valve experienced a greater deformation when the crimping was not ideally circular, the extent of the computed increase remained limited: the mean percentage difference was of 15.87% between *CIL* and *E65* and 14,11% between *CIL* and *E80*. Moreover, in the context of a Sano procedure for the first stage surgery in HLHS treatment, the long-term durability of the implanted shunt is not a major issue, because the venous conduit remains implanted over months, but not over multiple years. Indeed, in the second stage of the HLHS palliation surgery, which is generally performed at 3 to 6 months of age, the RVPA shunt is removed and pulmonary blood flow is supplied by an anastomosis between the superior vena cava and the pulmonary artery.

Valve orifice area during the cardiac cycle - At first, the leaflet systolic behavior was evaluated in the case of the unreinforced saphenous valved conduit by computing the valvular geometric orifice area (GOA) (**Figure 4.20**).

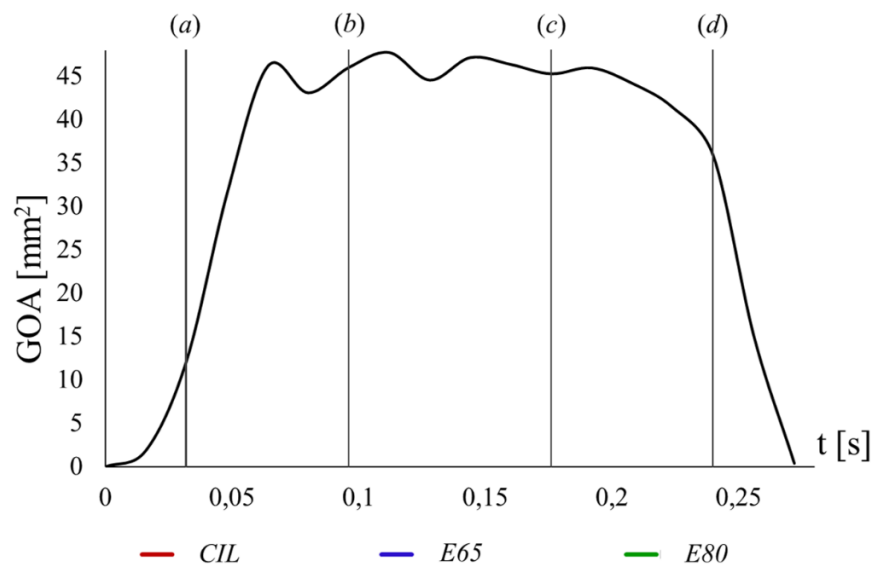


Figure 4.20: Geometric orifice area of the venous valve during systole in the unreinforced saphenous conduit, with highlighted four instants in which the view of the geometrical configurations of the valve were exported from Abaqus: (a) $t = 0.032$ s, (b) $t = 0.092$ s, (c) $t = 0.176$ s, (d) $t = 0.240$ s.

The leaflets reached their completely opened configuration after 0.064 s from the start of the second cardiac cycle; driven by the intervening pressure curve applied to the leaflets, the

whole valve systole lasted 0.288 s from the valve opening initiation to the end of the closure phase. Moreover, the valve showed a smooth opening and closure dynamics.

The leaflets in their opening configuration almost leaned on the internal surface of the vein thus allowing a nearly maximized orifice area. This can be observed from the downstream view of the valved conduit, acquired from Abaqus in four instants during the valve systole: at the leaflets aperture beginning (*a*); in two instants while the valve was completely opened (*b*), (*c*), and at valve closure initiation (*d*) (**Figure 4.21**).

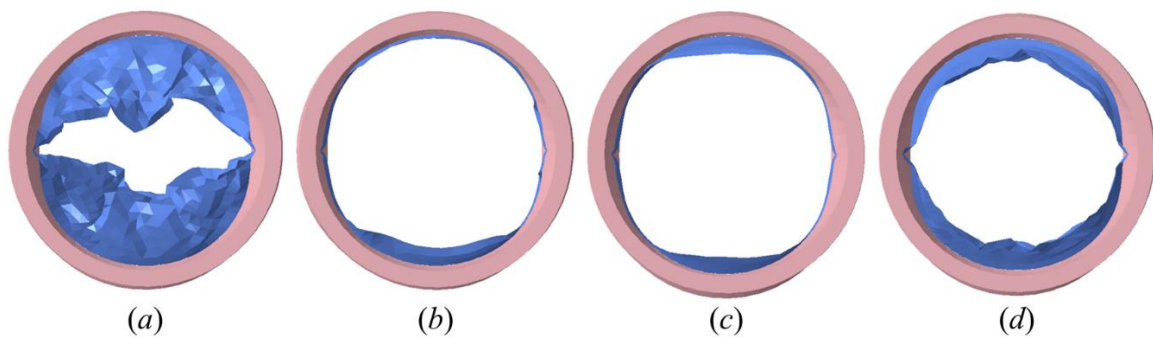


Figure 4.21: Downstream view of the valved conduit configuration in four time instants during systole: (*a*) $t = 0.032$ s, (*b*) $t = 0.092$ s, (*c*) $t = 0.176$ s, (*d*) $t = 0.240$ s.

A similar examination was conducted for the comparison of the three post-crimping configurations in the reinforced valved saphenous conduit: the valve GOA was significantly reduced with respect to the uncrimped conduit, but the GOA vs. time waveform was preserved (**Figure 4.22**).

However, with respect to the unreinforced conduit, the valve closure was slightly anticipated, due to the fact that in the crimped configuration the valvular leaflets come into contact earlier during the closing phase. The crimped valves reached their maximal opening between 0.048 s and 0.064 s after the cycle start and they accomplished a complete closure after 0.272 s. Even though the tracing was similar, the amount of GOA was highly different in the three crimped cases, as can be seen from the computation of the maximum, 90th percentile and mean GOA (**Table 4.10**).

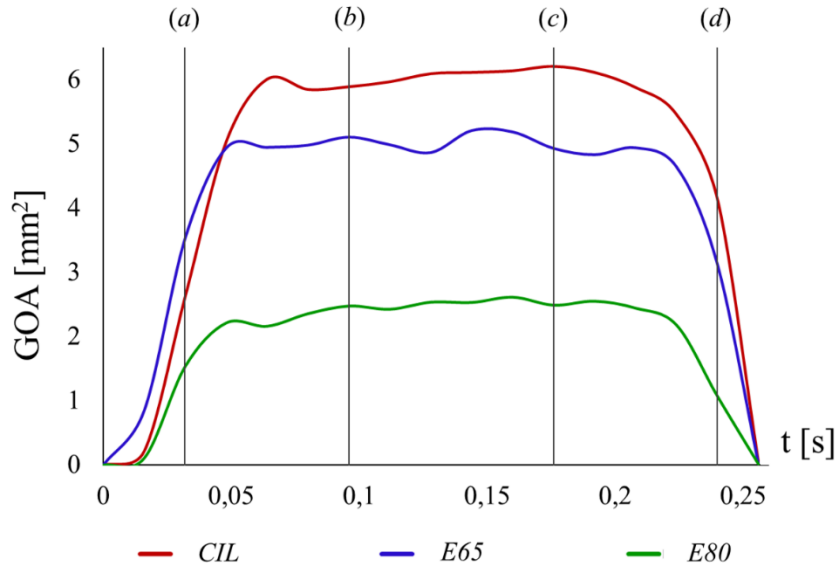


Figure 4.22: Geometric orifice area obtained for the crimped valved conduit in the different crimping modalities (*CIL*, *E65*, *E80*). the four instants in which the view of the geometrical configurations of the valves were exported from Abaqus are highlighted: (a) $t = 0.032$ s, (b) $t = 0.092$ s, (c) $t = 0.176$ s, (d) $t = 0.240$ s.

	GOA [mm ²]		
	<i>CIL</i>	<i>E65</i>	<i>E80</i>
Maximum	6.21	5.21	2.61
90 th percentile	6.13	5.15	2.54
Mean	4.86	4.18	1.98

Table 4.10: Maximum, 90th and Mean GOA obtained due to the different crimping modality applied.

In *E65* the GOA was reduced by about 15% with respect to *CIL*, while in *E80* the reduction was almost by 60% of the *CIL* GOA. This was due to the higher obstruction of the conduit by the leaflets, which was caused by the increasing eccentricity of the stent cross-section. As before, for a better understanding of the valve configuration, the downstream view of the valved conduit was acquired from Abaqus in the same four instants during the valve systole (**Figure 4.23**).

Generally, the crimped conduits exhibited a refold configuration of the leaflets, during the whole cardiac cycle simulation: however, the resulting orifice was still approximately circular in the *CIL* case (**Figure 4.23.CIL**), instead it offered a more irregular internal profile in the crimping with the elliptical final configurations.

In the *E65* case, the valve leaflets were so folded on themselves that they protruded into the lumen of the saphenous conduit for over a third of its height (**Figure 4.23.E65**); in *E80* they

even came into contact, splitting the orifice area of the valve in two separate sections (**Figure 4.23.E80**).

In light of this, besides inducing a reduction of the GOA during the valve systole, an elliptical crimping could also result in localized perturbations of the trans-valvular flow.

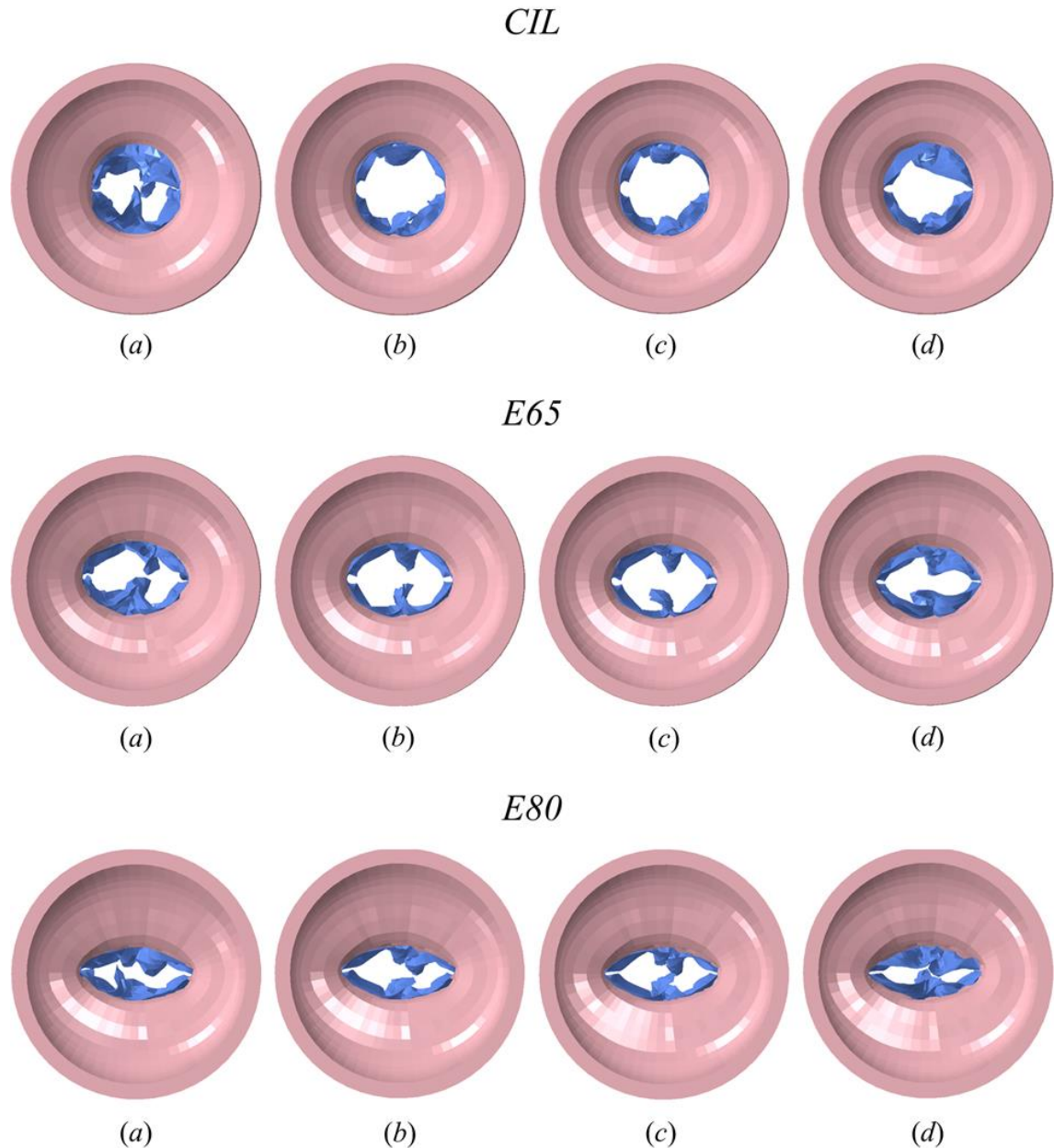


Figure 4.23: Downstream view of the three types of crimped valved conduit showing their configuration in four time instants during systole: (a) $t = 0.032$ s, (b) $t = 0.092$ s, (c) $t = 0.176$ s, (d) $t = 0.240$ s.

Chapter 5

Conclusions

5.1 Conclusions

At Boston Children's Hospital, an innovative Sano procedure for the first stage palliation in the hypoplastic left heart syndrome (HLHS) treatment was developed, consisting in the implantation of a right ventricle to pulmonary artery shunt: a valved venous conduit externally reinforced with a Palmaz stent [9]. In this procedure, if clinical monitoring suggests that the shunt allows for too much retrograde flow to the lungs, the stent might be crimped onto the vessel, to reduce this flow. However, the crimping operation is done manually and so there is a high risk of inaccurate maneuvers that can result in an irregular conformation of the shunt and thus in an increase in the hydraulic impedance of the conduit, leading to the development of pulmonary hypertension.

The aim of this thesis work was to provide a finite element simulation of this pioneering surgery and to assess the potential risks due to a defective crimping operation. In particular, three different final configurations were imposed to the crimper: the first was perfectly cylindrical, while the second and the third were elliptical, with an eccentricity of 0.65 and 0.80, respectively.

The employed methods succeeded in providing a complete simulation of this innovative surgical procedure, being able to model both the isolated components of the design (a Palmaz stent, a saphenous vein and a venous valve) and their complex interaction in the assembled model. Furthermore, the computational crimping of a stent on the outer surface of the valved venous shunt was achieved, whether a final cylindrical or elliptical configuration was imposed to the crimper. This aspect was a novelty for the numerical modelling scientific literature, in which, so far, only the stent intraluminal implantation was taken into account. Moreover, from the computational simulation of this surgery, it was possible to establish the stress patterns and the plastic strains produced on the stent and the venous conduit with the three different modalities for the crimping phase. With the aid of boxplot computation and statistical tests, it was assessed that a non-ideally cylindrical crimping modality may lead to an actual variation of the stress distributions with respect to the ideally cylindrical procedure: as for the saphenous vein, the elliptical crimping resulted in a rise both of the maximum traction sustained in the extremities of the vein inner surface and of the maximum compression experienced in the crimped portion of the conduit; while in the Palmaz stent an augmentation of the medial and maximum Von Mises stresses was found.

Furthermore, a simulation of two cardiac cycles was performed after the end of the different crimping phases and, from the analysis of the maximum principal strains in the valve commissures over the second cardiac cycle, an increase in the range of deformation was found passing from the cylindrically crimped conduit to the elliptical ones. This could be a factor in lowering the long-term durability of prosthetic valves, causing structural failure of the leaflets [21]; however, this likely may not constitute a substantial risk in the short-term application that was considered in the current thesis work [9].

In addition, during the second cardiac cycle systole, a considerable diversity in the geometric orifice area (GOA) obtained due to the diversity in the crimping modality was highlighted. The GOA was gradually reduced from the cylindrical crimping to the most elliptical ones: in *E65* the GOA was about the 85% of the *CIL* one, while in *E80* it was merely the 40% of the *CIL* GOA.

Moreover, it was also shown that an elliptical crimping could lead to an increase in the protrusion of the folded valve leaflets into the lumen, resulting in a higher hydraulic encumbrance caused by the shunt. This could induce an increase in the hydraulic resistance of the conduit, that could in effect enhance the work done by the right ventricle to overcome

it and in conclusion it could produce an associated hypertension at some level of the pulmonary circulation.

5.2 Limitations and Future developments

Although in this thesis work the effect of different crimping modalities was successfully tested, for the sake of simplicity, in this initial testing paradigmatic crimped configurations were assumed. A successive study could take into account a diverse modality for the crimping phase, for instance by imposing a more articulated application of the stent crimping, allowing a simulation of the procedure closer to reality, in which this operation is done manually by the clinicians.

Besides, a validation of the model would be required: a parallel experimental study is at the development stage at Boston Children's Hospital in order to assess the behavior of a concrete reinforced valved saphenous vein subjected to a crimping procedure, when placed in a hydraulic experimental set-up. This could provide a different view of the criticalities that could emerge from the innovative procedure considered and a support to the results obtained computationally.

Moreover, this thesis work laid the foundations for the simulation of the subsequent phase of the Roberts et al. surgery [9]: the balloon dilatation of the crimped conduit, to re-expand the shunt. This subsequent expansion phase was performed in one case, in which it resulted in trivial-to-mild regurgitation.

A forthcoming research could investigate the balloon dilatation of the valved venous shunt crimped in the various modalities to assess the potential difference both in the stresses suffered by the re-expanded shunts and in the valve conformation, depending on the crimped procedure used. Furthermore, a FE model could assist in the acquisition of a greater knowledge of what could be an adequate range of re-expansion, optimal to minimize unwanted backflows.

Besides, additional and complementary measurements could be obtained by the implementation of a computational fluid-structure interaction (FSI) model: in this case also the blood would be modelled, the cardiac cycles simulation could be accomplished imposing the flux that arrives from the right ventricle, instead of a pressure directly applied to the leaflets. With a FSI model it would be possible to extract also data regarding wall shear

stresses acting on the conduit, the flux streamlines and the velocity peaks; so, the different fluid dynamics and the recirculation cycles that could arise in the shunt due to the different crimping procedure applied could be compared. In addition, since GOA does not characterize the flow property, with FSI simulation it would be possible to compute the effective orifice area (EOA), the minimum area formed by the fluid downstream of the valve.

References

- [1] J. Betts, *Anatomy and Physiology*, Chapter 19 - The Cardiovascular System: The Heart, OpenStax College (1788), 2013.
- [2] F. Netter, *Atlas of Human Anatomy* (sixth edition), Plate 221, Saunders, imprint of Elsevier Inc., 2014.
- [3] F. Baldissera and C. Porro, *Fisiologia e Biofisica Medica* (fourth edition), Chapter 45 - Meccanica Cardiaca, vol. 2, Poletto Editore srl, 2012.
- [4] E. Braunwald, D. Zipes and P. Libby, *Heart Disease: A Textbook of Cardiovascular Medicine* (sixth edition), Chapter 43 - Congenital Heart Disease in Infancy and Childhood, W. B. Saunders Company, 2001.
- [5] S. Sano, K. Ishino, M. Kawada, S. Arai, S. Kasahara, T. Asai, Z. Masuda, M. Takeuchi and S. Ohtsuki, "Right ventricle-pulmonary artery shunt in first-stage palliation of hypoplastic left heart syndrome," *J Thorac Cardiovasc Surg*, vol. 126, no. 2, pp. 504-509, August 2003.
- [6] R. Ohye, L. Sleeper, L. Mahony, J. Newburger, G. Pearson, M. Lu, C. Goldberg, S. Tabbutt, P. Frommelt, N. Ghanayem, P. Laussen, J. Rhodes, A. Lewis, S. Mital, C. Ravishankar, I. Williams, C. Dunbar-Masterson, A. Atz, S. Colan, L. Minich, C. Pizarro, K. Kanter, J. Jagers, J. Jacobs and Kraw, "Comparison of shunt types in the Norwood procedure for single-ventricle lesions," *N Engl J Med*, vol. 362, no. 21, pp. 1980-92, May 2010.
- [7] C. Schreiber, J. Kasnar-Samprec, J. Hörer, A. Eicken, J. Cleuziou, Z. Prodan and R. Lange, "Ring-enforced right ventricle-to-pulmonary artery conduit in Norwood stage I reduces proximal conduit stenosis," *Ann Thorac Surg*, vol. 88, no. 5, pp. 1541-5, Nov 2009.
- [8] C. Baird, P. Myers, M. Borisuk, F. Pigula and S. Emani, "Ring-reinforced Sano conduit at Norwood stage I reduces proximal conduit obstruction," *Ann Thorac Surg*, vol. 99, no. 1, pp. 171-9, Jan 2015.

- [9] E. Roberts, L. Quinonez, B. Piekarski and S. E. C.W. Baird CW2, “Expandable Valve for Pediatric Application Constructed From Human Venous Valved Conduit Within a Stent,” *Ann Thorac Surg*, vol. 100, no. 6, pp. 2320-4, 2015.
- [10] B. Alsoufi, C. Manlhiot, M. Al-Ahmadi, B. McCrindle, A. Kalloghlian, G. Siblini, Z. Bulbul and Z. Al-Halees, “Outcomes and associated risk factors for mitral valve replacement in children,” *Eur J Cardiothorac Surg.*, vol. 40, no. 3, pp. 543-51, Sept 2011.
- [11] J. Feng, X. Zihui and S. Katsuhiko, “On the finite element modelling of balloon-expandable stents,” *J Mech Behav Biomed Mater*, vol. 1, no. 1, pp. 86-95, Jan 2007.
- [12] D. Lim, S. Cho, W. Park, A. Kristensson, J. Ko, S. Al-Hassani and H. Kim, “Suggestion of potential stent design parameters to reduce restenosis risk driven by foreshortening or dogboning due to non-uniform balloon-stent expansion,” *Ann Biomed Eng*, vol. 36, no. 7, pp. 1118-29, Jul 2008.
- [13] C. Canver, “Conduit options in coronary artery bypass surgery,” *Chest*, vol. 108, no. 4, pp. 1150-5, Oct 1995.
- [14] M. Hwang, S. Berceci, M. Garbey, N. Kim and R. Tran-Son-Tay, “The dynamics of vein graft remodeling induced by hemodynamic forces: a mathematical model,” *Biomech Model Mechanobiol*, vol. 11, no. 3-4, pp. 411-23, Mar 2012.
- [15] J. Veselý, L. Horný, H. Chlup, T. Adámek, M. Krajiček and R. Žitný, “Constitutive modeling of human saphenous veins at overloading pressures,” *J Mech Behav Biomed Mater.*, vol. 45, pp. 101-8, May 2015.
- [16] A. Narracott, J. Keijsers, C. Leguy, W. Huberts and a. F. v. d. Vosse, “Fluid-Structure Interaction analysis of Venous Valve Hemodynamics,” in *4th International Conference on Computational and Mathematical Biomedical Engineering*, 29 June-1 July 2015.
- [17] P. Hammer, E. Roberts, S. Emani and P. D. Nido, “Surgical reconstruction of semilunar valves in the growing child: Should we mimic the venous valve? A simulation study,” *J Thorac Cardiovasc Surg*, vol. 153, no. 2, pp. 389-396, Feb 2017.
- [18] F. Sturla, E. Votta, M. Stevanella, C. Conti and A. Redaelli, “Impact of modeling fluid-structure interaction in the computational analysis of aortic root biomechanics,” *Med Eng Phys.*, vol. 35, no. 12, pp. 1721-30, Dec 2013.

- [19] E. Votta, F. Maisano, S. Bolling, O. Alfieri, F. Montevocchi and A. Redaelli, "The Geofrom disease-specific annuloplasty system: a finite element study.," vol. 84, no. 1, pp. 92-101, Jul 2007.
- [20] SIMULIA Abaqus, "Abaqus Analysys User's Guide, Analysis Continuation Techniques: Restarting an Analysis," [Online]. Available: <https://www.sharcnet.ca/Software/Abaqus/6.14.2/v6.14/books/usb/default.htm?startat=pt04ch09s01aus53.html#usb-anl-arestart>.
- [21] P. Gunning, N. Saikrishnan, A. Yoganathan and L. McNamara, "Total ellipse of the heart valve: the impact of eccentric stent distortion on the regional dynamic deformation of pericardial tissue leaflets of a transcatheter aortic valve replacement," *J R Soc Interface.*, vol. 12, no. 113, Dec 2015.